

T-3932

FINITE ELEMENT ANALYSIS OF RESIDUAL STRESS
AND DISTORTION IN FORGED AND
CARBURIZED GEAR STEEL

by

Donald B. Larson

ARTHUR LAKES LIBRARY
COLORADO SCHOOL of MINES
GOLDEN, COLORADO 80401

ProQuest Number: 10783633

All rights reserved

INFORMATION TO ALL USERS

The quality of this reproduction is dependent upon the quality of the copy submitted.

In the unlikely event that the author did not send a complete manuscript and there are missing pages, these will be noted. Also, if material had to be removed, a note will indicate the deletion.



ProQuest 10783633

Published by ProQuest LLC (2018). Copyright of the Dissertation is held by the Author.

All rights reserved.

This work is protected against unauthorized copying under Title 17, United States Code
Microform Edition © ProQuest LLC.


ProQuest LLC.
789 East Eisenhower Parkway
P.O. Box 1346
Ann Arbor, MI 48106 – 1346

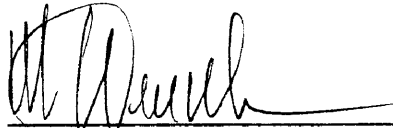
T-3932


A thesis submitted to the Faculty and the Board of Trustees of the Colorado School of Mines in partial fulfillment of the requirements for the degree of Master of Science (Applied Mechanics).

Golden, Colorado

Date 12/12/90

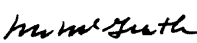
Signed: 
Donald B. Larson

Approved: 
Dr. Mogens Henriksen
Thesis Advisor


Dr. Chester J. Van Tyne
Co-Advisor

Golden, Colorado

Date 12/13/90

 12/13/90
Dr. Michael McGrath
Professor of Engineering
and Head of Department,
Department of Engineering

ABSTRACT

A two-dimensional plane strain thermomechanical finite element program was developed to calculate the residual stresses and distortion generated during quenching of carburized SAE 4023 and SAE 4620 gear steel. The incremental elastic-plastic constitutive equation incorporates the von Mises yield criterion, isotropic hardening, the Prandtl-Reuss flow rule and considers yield strength as a function of plastic strain and temperature. The elastic modulus is also a function of temperature and it is treated accordingly. The martensitic phase transformation is the only solid state reaction considered.

The numerical analysis was compared to an experimental procedure incorporating the Almen strip test. Almen strips of various thicknesses were carburized on one side only, quenched to 176°C and air cooled to 25°C. The resulting radius of curvature was compared to that predicted by the developed program.

The calculated arc deflection for the 2.03, 2.44 and 3.18 millimeter Almen strip models were of correct direction (carburized surface convex), order of magnitude and trend (the 2.03 millimeter Almen strip model deflected the most; the 3.18 millimeter model the least), but the results did not agree with the experimental results.

Discrepancies can be attributed to insufficiently refined constitutive modeling techniques and the constitutive data used for the SAE 4023 and SAE 4620 alloy steels.

An initial sensitivity study was performed on a limited number of input parameters. The variables having the greatest influence on distortion and the residual stress profile are the martensite start temperature and the elastic modulus.

TABLE OF CONTENTS

| | <u>Page</u> |
|--|-------------|
| ABSTRACT | iii |
| LIST OF FIGURES | viii |
| LIST OF TABLES | xvii |
| NOMENCLATURE | xix |
| ACKNOWLEDGMENTS | xxi |
| 1.0 INTRODUCTION | 1 |
| 1.1 Motivation | 1 |
| 1.2 Distortion | 2 |
| 1.3 Review of Residual Stress | 3 |
| 1.3.1 Residual Stress Generation due to Thermal Contraction in a Homogeneous Steel Cylinder | 4 |
| 1.3.2 Residual Stress Generation due to a Martensitic Phase Transformation in a Case Carburized Steel Cylinder | 6 |
| 1.4 Literature Review | 8 |
| 2.0 MODELING PROCEDURE USING THE FINITE ELEMENT METHOD | 13 |
| 2.1 Review of Thermomechanical Coupling | 13 |
| 2.3 Model Material Assumptions | 15 |
| 2.4 Thermomechanical Coupling Assumptions | 16 |
| 2.5 Thermal Analysis and Input Properties | 17 |
| 2.6 Thermal and Phase Transformation Strains | 18 |
| 2.7 Elastic-Plastic Stress Analysis | 19 |
| 2.7.1 Elastic-Plastic Constitutive Equation | 20 |
| 2.7.2 Mechanical Input Data | 20 |
| 2.7.3 Stiffness Matrix and Iteration Scheme | 21 |
| 2.7.4 Verification of the Elastic-Plastic Stress Analysis | 21 |

| | | |
|-------|--|-----|
| 3.0 | NUMERICAL AND EXPERIMENTAL PROCEDURE | 22 |
| 3.1 | Input Data Used in CSMCARB | 23 |
| 3.1.1 | Finite Element Mesh | 25 |
| 3.1.2 | Carbon Profile Determination | 25 |
| 3.1.3 | Spatial and Temperature Convergence Study | 28 |
| 3.2 | Verification Procedure - The Modified Almen Strip Test | 33 |
| 3.2.1 | As-Received Material | 35 |
| 3.2.2 | Almen Strip Preparation and Testing | 36 |
| 4.0 | EXPERIMENTAL AND NUMERICAL RESULTS | 39 |
| 4.1 | Microhardness, Carbon and M_s Profiles | 39 |
| 4.2 | Experimental and Numerical Deflection Results | 50 |
| 4.3 | Experimental and Numerical Residual Stress Profiles | 66 |
| 5.0 | INPUT DATA SENSITIVITY STUDY USING CSMCARB | 76 |
| 5.1 | Martensitic Start Temperature Sensitivity | 76 |
| 5.2 | Elastic Modulus Sensitivity | 80 |
| 5.3 | Yield Strength Sensitivity | 83 |
| 6.0 | DISCUSSION | 87 |
| 6.1 | Calculated Deflection History Explanation | 87 |
| 6.2 | Microhardness, Carbon, and M_s Profiles | 92 |
| 6.3 | Phase Transformation Analysis | 93 |
| 6.4 | Mechanical Property Data | 94 |
| 6.5 | Arc Deflection Results | 94 |
| 6.6 | Calculated Residual Stress Profiles | 96 |
| 7.0 | CONCLUDING REMARKS | 99 |
| 7.1 | Application of the Finite Element Method to Thermal-Elastic-Plastic Analyses | 99 |
| 7.2 | Carbon Profile Determination | 100 |
| 7.3 | Simplifying Assumptions and Input Data | 100 |
| 8.0 | SUGGESTIONS FOR FUTURE WORK | 102 |
| 8.1 | Numerical Considerations | 102 |
| 8.2 | Thermomechanical Coupling | 102 |
| 8.3 | Carbon Profile and Phase Transformation Analysis | 103 |
| 8.4 | High Temperature Mechanical Properties | 103 |
| 9.0 | REFERENCES | 104 |

| | | |
|------------|---|-----|
| APPENDIX A | Derivation of an Implicit Integration Scheme to Determine the Transient Temperature Distribution During Quenching | 108 |
| APPENDIX B | Thermal, Phase and Mechanical Properties Incorporated in CSMCARB. | 113 |
| APPENDIX C | Derivation of An Elastic-Plastic Constitutive Equation with Temperature Effect | 139 |
| APPENDIX D | Verification Problems using CSMCARB . . . | 150 |
| APPENDIX E | Calculation of the Almen Strip Radius of Curvature | 172 |

LIST OF FIGURES

| | <u>Page</u> |
|--|-------------|
| Figure 1.1 Development of residual stress in a cylindrical specimen due to cooling only with no phase transformation (longitudinal stress shown) (10). | 5 |
| Figure 1.2 Residual stress generation due to a martensitic phase transformation in a carburized steel cylinder (10). | 7 |
| Figure 2.1 Schematic illustrating the interactions for a thermomechanical analysis with phase transformation (17). | 14 |
| Figure 3.1 Schematic illustrating the time-temperature history of the experimental alloy steel samples. | 24 |
| Figure 3.2 Finite element model used in this study consisting of 10 rows by 10 columns of eight noded isoparametric elements. The lower surface is the high carbon surface. | 26 |
| Figure 3.3 Deflection history for the 2.03 millimeter Almen strip model using spatial meshes of 6x6, 8x8, 10x10 and 12x12 elements. The maximum temperature increment is -2.5°C. The analysis begins at 871°C and continues to 25°C. | 29 |
| Figure 3.4 Axial stress (τ_{xx}) distribution at 25°C for the 2.03 millimeter Almen strip model using various indicated meshes and a maximum temperature increment of -2.5°C. | 30 |

| | | |
|------------|---|----|
| Figure 3.5 | Deflection history of the 2.03 millimeter Almen strip model using a spatial mesh of 5x5 elements. Maximum temperature increments, ΔT , of -5.0°C , -2.5°C , -1.0°C and -0.5°C are shown. The analysis begins at 871°C and continues to 25°C | 31 |
| Figure 3.6 | Axial stress (τ_{xx}) distribution at 25°C for the 2.03 millimeter Almen strip model using a spatial mesh of 5x5 elements and the various indicated maximum temperature increments. | 32 |
| Figure 3.7 | Illustration of the Almen strip test commonly used in shot peening application to determine the intensity of the peening process (28). | 34 |
| Figure 4.1 | Experimental microhardness profile for the 1.30 millimeter SAE 4023 Almen strip. | 40 |
| Figure 4.2 | Experimental microhardness profile for the 1.85 millimeter SAE 4023 Almen strip. | 41 |
| Figure 4.3 | Experimental microhardness profile for the 2.03 millimeter SAE 4023 Almen strip. | 42 |
| Figure 4.4 | Experimental microhardness profile for the 2.44 millimeter SAE 4023 Almen strip. | 43 |
| Figure 4.5 | Experimental microhardness profile for the 3.18 millimeter SAE 4023 Almen strip. | 44 |
| Figure 4.6 | Carbon profile determined from microhardness data for the 1.30 millimeter Almen strip of SAE 4023 alloy steel. | 45 |

| | | |
|-------------|---|----|
| Figure 4.7 | Carbon profile determined from microhardness data for the 1.85 millimeter Almen strip of SAE 4023 alloy steel. | 46 |
| Figure 4.8 | Carbon profile determined from microhardness data for the 2.03 millimeter Almen strip of SAE 4023 alloy steel. | 47 |
| Figure 4.9 | Carbon profile determined from microhardness data for the 2.44 millimeter Almen strip of SAE 4023 alloy steel. | 48 |
| Figure 4.10 | Carbon profile determined from microhardness data for the 3.18 millimeter Almen strip of SAE 4023 alloy steel. | 49 |
| Figure 4.11 | Calculated M_s profile for the 1.30 millimeter Almen strip of SAE 4023 alloy steel. | 51 |
| Figure 4.12 | Calculated M_s profile for the 1.85 millimeter Almen strip of SAE 4023 alloy steel. | 52 |
| Figure 4.13 | Calculated M_s profile for the 2.03 millimeter Almen strip of SAE 4023 alloy steel. | 53 |
| Figure 4.14 | Calculated M_s profile for the 2.44 millimeter Almen strip of SAE 4023 alloy steel. | 54 |
| Figure 4.15 | Calculated M_s profile for the 3.18 millimeter Almen strip of SAE 4023 alloy steel. | 55 |
| Figure 4.16 | Calculated percentage of martensite as a function of thickness for the 1.30 millimeter Almen strip of SAE 4023 alloy steel at 25°C. | 56 |

| | | |
|-------------|--|----|
| Figure 4.17 | Calculated percentage of martensite as a function of thickness for the 1.85 millimeter Almen strip of SAE 4023 alloy steel at 25°C. | 57 |
| Figure 4.18 | Calculated percentage of martensite as a function of thickness for the 2.03 millimeter Almen strip of SAE 4023 alloy steel at 25°C. | 58 |
| Figure 4.19 | Calculated percentage of martensite as a function of thickness for the 2.44 millimeter Almen strip of SAE 4023 alloy steel at 25°C. | 59 |
| Figure 4.20 | Calculated percentage of martensite as a function of thickness for the 3.18 millimeter Almen strip of SAE 4023 alloy steel at 25°C. | 60 |
| Figure 4.21 | Deflected shape of the SAE 4023 Almen strips after being carburized and quenched. The various thicknesses are indicated. The carburized surface is convex. | 61 |
| Figure 4.22 | Deflected shape of the SAE 4023 Almen strips after being carburized and quenched. The carburized surface is convex. | 62 |
| Figure 4.23 | Deflection history for the various indicated thicknesses of SAE 4023 Almen strips. The analysis begins at 871°C and continues to 25°C. | 65 |
| Figure 4.24 | Average radius of curvature at 25°C for the five thicknesses of experimental Almen strips and the calculated radius of curvature using CSMCARB for the SAE 4023 alloy. | 67 |
| Figure 4.25 | Calculated residual stress profile through the model thickness for the 1.30 millimeter SAE 4023 Almen strip model at 25°C. | 68 |

| | | |
|-------------|---|----|
| Figure 4.26 | Calculated residual stress profile through the model thickness for the 1.85 millimeter SAE 4023 Almen strip model at 25°C. | 69 |
| Figure 4.27 | Calculated residual stress profile through the model thickness for the 2.03 millimeter SAE 4023 Almen strip model at 25°C. | 70 |
| Figure 4.28 | Calculated residual stress profile through the model thickness for the 2.44 millimeter SAE 4023 Almen strip model at 25°C. | 71 |
| Figure 4.29 | Calculated residual stress profile through the model thickness for the 3.18 millimeter SAE 4023 Almen strip model at 25°C. | 72 |
| Figure 4.30 | Calculated residual stress profile through the model thickness and experimental x-ray diffraction measurements for the SAE 4023 2.44 millimeter Almen strip. | 74 |
| Figure 4.31 | Calculated residual stress profile through the model thickness and experimental x-ray diffraction measurements for the SAE 4023 2.44 millimeter Almen strip. | 75 |
| Figure 5.1 | Deflection history for the 2.03 millimeter SAE 4023 Almen strip models with a 20% increase and 20% decrease of the M_s temperature. The analysis begins at 871°C and continues to 25°C. | 77 |
| Figure 5.2 | Residual stress distributions at 25°C for 2.03 millimeter SAE 4023 Almen strip models with a 20% increase and 20% decrease of the M_s temperature. | 78 |

Figure 5.3 Deflection history for the 2.03 millimeter SAE 4023 Almen strip models with a 20% increase and 20% decrease of the elastic modulus, E. The analysis begins at 871°C and continues to 25°C. 81

Figure 5.4 Residual stress distributions at 25°C for 2.03 millimeter SAE 4023 Almen strip models with a 20% increase and 20% decrease of the elastic modulus, E. 82

Figure 5.5 Deflection history for the 2.03 millimeter SAE 4023 Almen strip models with a 20% increase and 20% decrease of the yield strength, S_y . The analysis begins at 871°C and continues to 25°C. 84

Figure 5.6 Residual stress distributions at 25°C for 2.03 millimeter SAE 4023 Almen strip models with a 20% increase and 20% decrease of the yield strength, S_y 85

Figure 6.1 Finite element model used in this study consisting of 10 rows by 10 columns of eight noded isoparametric elements. 88

Figure 6.2 Deflection history for 2.03 millimeter SAE 4023 Almen strip model. The analysis begins at 871°C and continues to 25°C. 89

Figure 6.3 Schematic illustrating the relative strain distributions through the thickness of a typical Almen strip model at four temperatures indicated in Figure 6.2. The lower surface is the carburized surface. 90

| | | |
|------------|---|-----|
| Figure B.1 | Thermal conductivity, K , as a function of temperature for a 0.23 weight percent SAE 4023 alloy steel transforming from austenite to martensite ($M_s = 415^\circ\text{C}$) beginning at 871°C and continuing to 25°C | 115 |
| Figure B.2 | Specific heat, C_p , as a function of temperature for a 0.23 weight percent SAE 4023 alloy steel transforming from austenite to martensite ($M_s = 415^\circ\text{C}$) beginning at 871°C and continuing to 25°C | 117 |
| Figure B.3 | Density, ρ , as a function of temperature for a 0.23 weight percent SAE 4023 alloy steel transforming from austenite to martensite ($M_s = 415^\circ\text{C}$) beginning at 871°C and continuing to 25°C | 119 |
| Figure B.4 | The convective heat loss coefficient, h_c , as a function of temperature for steel immersed in oil (18). | 121 |
| Figure B.5 | The coefficient of thermal expansion, α , as a function of temperature and carbon content for ferrite, pearlite, bainite, martensite and cementite. | 123 |
| Figure B.6 | The martensite start temperature, M_s , as a function of carbon concentration for the SAE 4023 and SAE 4620 alloy steels using Andrew's linear equation. | 125 |
| Figure B.7 | The volume fraction of martensite formed as a function of temperature for steels of 0.20, 0.50 and 0.80 weight percent carbon. | 127 |

| | | |
|-------------|--|-----|
| Figure B.8 | Transformation strain as a function of carbon concentration for the ferritic, pearlitic, bainitic and martensitic phase transformations (2). | 129 |
| Figure B.9 | Calculated dilatometric strain as a function of temperature for 0.20 and 0.80 weight percent carbon SAE 4620 alloy steels cooled from 871°C to 25°C. | 130 |
| Figure B.10 | Elastic modulus, E , as a function of temperature for a 0.23 weight percent SAE 4023 alloy steel transforming from austenite to martensite ($M_s = 415^\circ\text{C}$) beginning at 871°C and continuing to 25°C. | 132 |
| Figure B.11 | Yield strength, S_y , as a function of temperature for a 0.23 weight percent SAE 4023 alloy steel transforming from austenite to martensite ($M_s = 415^\circ\text{C}$) beginning at 871°C and continuing to 25°C. | 135 |
| Figure B.12 | The stress strain behavior for a 0.23 weight percent SAE 4023 alloy steel transforming from austenite to martensite ($M_s = 415^\circ\text{C}$) at the various indicated temperatures. | 138 |
| Figure C.1 | The von Mises' yield criterion, assuming isotropic hardening, represented geometrically by the yield cylinder (21). | 140 |
| Figure D.1 | Schematic illustrating the axial load model used to verify the constitutive equation in CSMCARB. | 151 |
| Figure D.2 | Schematic illustrating the thick wall pressure vessel model used to verify the constitutive equation in CSMCARB (24). | 152 |

| | | |
|-------------|--|-----|
| Figure D.3 | Stress-strain diagram and the applied loads for verification problem #1. | 154 |
| Figure D.4 | Stress-strain diagram and the applied loads for verification problem #2. | 156 |
| Figure D.5 | Stress-strain diagram and the applied loads for verification problem #3. | 158 |
| Figure D.6 | Stress-strain diagram and the applied loads for verification problem #4. | 160 |
| Figure D.7 | Stress-strain diagram and the applied loads for verification problem #5. | 162 |
| Figure D.8 | Stress-strain diagram and the applied loads for verification problem #6. | 164 |
| Figure D.9 | Stress-strain diagram and the applied loads for verification problem #7. | 166 |
| Figure D.10 | Stress-strain diagram and the applied loads for verification problem #8. | 168 |
| Figure E.1 | Schematic representing the radius of curvature for the Almen strip. | 173 |

LIST OF TABLES

| | <u>Page</u> |
|---|-------------|
| Table 3.1 Alloy Steel Composition | 22 |
| Table 3.2 Two Stage Quench Process | 23 |
| Table 3.3 As-Received Hardness | 36 |
| Table 3.4 Geometry of Experimental Almen Strips . . . | 37 |
| Table 4.1 Experimental Arc Deflection Results at 25°C | 63 |
| Table 4.2 Average Experimental and Calculated Arc Deflection Results at 25°C | 64 |
| Table 5.1 M_s Sensitivity Analysis - Arc Deflection | 79 |
| Table 5.2 M_s Sensitivity Analysis - Residual Stress | 79 |
| Table 5.3 Elastic Modulus Sensitivity Analysis - Arc Deflection | 80 |
| Table 5.4 Elastic Modulus Sensitivity Analysis - Residual Stress | 83 |
| Table 5.5 Yield Strength Sensitivity Analysis - Arc Deflection | 86 |
| Table 5.6 Yield Strength Sensitivity Analysis - Residual Stress | 86 |
| Table B.1 Coefficients for Thermal Conductivity . . . | 114 |
| Table B.2 Coefficients for Specific Heat | 116 |
| Table B.3 Coefficients for Density | 118 |
| Table B.4 Convection Coefficient Data | 120 |
| Table B.5 Coefficients for the Coefficient of Thermal Expansion | 122 |

| | | |
|-----------|---|-----|
| Table B.6 | Linear Dilatometric Strain Associated with Transformation to the Indicated Phases | 128 |
| Table B.7 | Coefficients for Elastic Modulus | 131 |
| Table B.8 | Coefficients for Yield Strength | 133 |
| Table B.9 | Coefficients for Stress at Four Percent Strain | 136 |

NOMENCLATURE

| | |
|--------------------------------|--|
| A | arbitrary dependent variable (Appendix A) |
| C | carbon content in weight percent |
| [C] | "damping" matrix (Appendix A) |
| D | thermal diffusivity |
| D_c^y | diffusivity of carbon in austenite |
| [D] | elastic constitutive matrix (Appendix C) |
| E | elastic modulus |
| E^T | tangent modulus |
| F | yield function |
| H | thickness of Almen strip |
| H | strain hardening parameter (Appendix C) |
| HRC | hardness (Rockwell C scale) |
| h_c | convection coefficient |
| J_2 | second stress invariant |
| K | conductivity |
| K_{ij} | stiffness matrix |
| L_j | length of Almen strip |
| m | meter |
| mm | millimeter |
| M_s | martensite start temperature |
| R_j | flux matrix (Appendix A) |
| s | deviatoric stress |
| S_y | uniaxial yield strength |
| S_4 | stress at four percent strain |
| t | time |
| T | temperature |
| v | weighing parameter (Appendix A) |
| W | width of Almen strip |
| x | position |
| α | coefficient of thermal expansion |
| β | change in yield strength with temperature (Appen. C) |
| $\{\Delta\varepsilon^K\}$ | incremental kinematic strain * |
| $\{\Delta\varepsilon^{EL}\}$ | incremental elastic strain * |
| $\{\Delta\varepsilon^{PL}\}$ | incremental plastic strain * |
| $\{\Delta\varepsilon^\theta\}$ | incremental thermal strain * |
| $\{\Delta\varepsilon^\phi\}$ | incremental phase strain * |
| $\{\Delta\varepsilon\}$ | effective incremental plastic strain * |
| $\{\Delta\tau\}$ | incremental stress * |
| $\{\varepsilon^K\}$ | total kinematic strain * |
| $\{\varepsilon^{EL}\}$ | total elastic strain * |
| $\{\varepsilon^{ELt}\}$ | historical elastic strain * |
| $\{\varepsilon^{PL}\}$ | total plastic strain * |

| | |
|--------------------------|--|
| $\{\varepsilon^\theta\}$ | total thermal strain * |
| $\{\varepsilon^\phi\}$ | total phase strain * |
| ΔT | incremental change in temperature |
| $\{\bar{\varepsilon}\}$ | effective total plastic strain * |
| θ | integration constant (θ -method) |
| λ | constant of proportionality (flow rule) |
| ν | Poisson's ratio |
| ρ | density |
| σ_θ | hoop stress |
| τ | Cauchy stress |
| d | total derivative operator |
| ∂ | partial derivative operator |
| Δ | finite incremental change |
| $\{X\}$ | column array of components, X_i (i = row number) |
| $\langle Y \rangle$ | row vector of components, Y_j (j = column number) |
| $[Z]$ | two-dimensional array of components Z_{ij} |

* The column vectors for strain and stress contain the following components:

$$\{\varepsilon\} = \begin{Bmatrix} \varepsilon_{xx} \\ \varepsilon_{yy} \\ \varepsilon_{xy} \\ \varepsilon_{zz} \end{Bmatrix}$$

Note: ε_{xy} is defined as engineering shear strain

ACKNOWLEDGMENTS

The author would like to thank Dr. Mogens Henriksen (thesis advisor) for his technical and moral support in making this study a reality. CSM will surely miss his presence.

The author would also like to thank his thesis committee, Dr. Chester Van Tyne (co-thesis advisor), Dr. George Krauss, Dr. David Matlock and Dr. Graham Mustoe for their support which made this investigation possible.

For technical and financial assistance, the author would like to thank the professors, staff and students in the Advanced Steel Processing and Products Research Center at the Colorado School of Mines.

Thanks go to Tony Freda (Chrysler Motor Corporation) for his assistance in the experimental procedure and to Dennis Vukovich and Aquil Ahmad (Eaton Corporation) for their assistance in x-ray diffraction measurements.

For their moral support, thanks also go to John, Damon, Öl, Bob and the brothers of KE (A.E.K.Δ.B).

Last, and quite possibly most, the author would like to thank the Larson family for their patience and support.

1.0 INTRODUCTION

This study, sponsored by the Advanced Steel Processing and Products Research Center at the Colorado School of Mines, was initiated to provide a better understanding of the distortion phenomenon currently seen in the industrial manufacturing of forged, carburized and heat treated steel. To more fully quantify the sources of these distortions, a finite element program, CSMCARB, was developed to more fully characterize the distortion produced by the quench that follows carburizing.

An experimental procedure, using a simple geometry which produced measurable distortion, enabled a direct comparison with the numerical results.

This study provides an alternative approach in distortion prediction to those used by previous authors (1,2,3,4). The derivation and implementation of an incremental elastic-plastic constitutive equation used in this study is also different than that used in the past.

1.1 Motivation

The motivation for this work is the need in the heat treatment industry for an accurate numerical method to determine the residual stress distribution and geometric distortion in carburized and quenched steel gears. This numerical method could improve industrial practices by

minimizing or eliminating final grinding operations, press quench techniques or compensated gear design. The result would be a lower priced, higher quality steel gear component.

1.2 Distortion

Distortion in carburized and quenched alloy steel parts is caused by the development of residual stress and local plasticity (1,2,3,4,5,6,7). The severity of residual stresses depend on the suppressed strains associated with thermal and phase induced dilatation. Residual stresses often exceed the hot yield strength of the alloy. Local plastic flow can result in a macroscopic dimensional changes, commonly referred to as distortion.

Three specific types of distortion can occur during the manufacturing of carburized steel gears. Unwinding is observed in heat treated helical gears where the helix angle of the gear teeth decreases (i.e. the face of the gear tooth tends to become parallel with the gear's axis). Involute distortion is said to occur when the involute of the gear tooth changes shape, creating mesh misalignment which produces excess vibration and noise. "Potato-chipping" also can occur when the entire gear becomes warped in its plane of rotation (8).

1.3 Review of Residual Stress

The carburizing process used to surface harden steel requires heating the steel to a temperature above the A_3 temperature. While at this temperature, the steel is exposed to a carbon rich atmosphere, thus increasing the steel's surface carbon concentration (9). The steel is subsequently quenched to ambient temperatures. In such heat treatments, the transformation of the austenite phase into decomposition phases (ferrite, carbide, pearlite, bainite, and/or martensite) is accompanied by a volumetric swelling of the steel (10). The increased carbon in the surface layer lowers the martensite start (M_s) temperature; thus it delays the transformation of the case austenite to a lower temperature and a correspondingly later time than the transformation of the austenite in the core (11). This time lag creates varying magnitudes of restricted internal strains resulting in the generation of residual compressive stress at the surface of the component.

Other sources of residual stress exist. Any material with substantial thickness will generate residual stress due to differential temperatures. This is particularly true for steels with a relatively low thermal conductivity and temperature dependent yield strength. This thermal stress will combine with that created by phase transformations (10).

The following sections describe the residual stress formation in a cylindrical steel geometry due to thermal contraction only and a martensitic phase transformation in a case carburized steel. Additional discussion of residual stress development due to thermal and phase transformation strains can be found in a variety of texts and papers (7,10,11,12,13,14).

1.3.1 Residual Stress Generation due to Thermal Contraction in a Homogeneous Steel Cylinder

The development of residual stress due to cooling of a steel cylindrical sample with no phase transformation is illustrated in Figure 1.1 (10). The normal temperature-time cooling curves for the surface and core of the cylinder are illustrated in the upper left figure. The surface cooling rate is much greater than the core cooling rate. Initially the cylinder is at a uniform temperature (label A). Since the surface of the cylinder cools faster than the core, it will tend to undergo its normal thermal shrinkage at a faster rate than the core (label B). The hotter (and therefore relatively larger) core of the bar will not permit the outer surface to undergo the contraction which it would see as a free body. Consequently, tensile stress is generated in the axial and circumferential directions of the cooling surface. This stress is shown as curve (a). However, since this contraction is occurring at an elevated

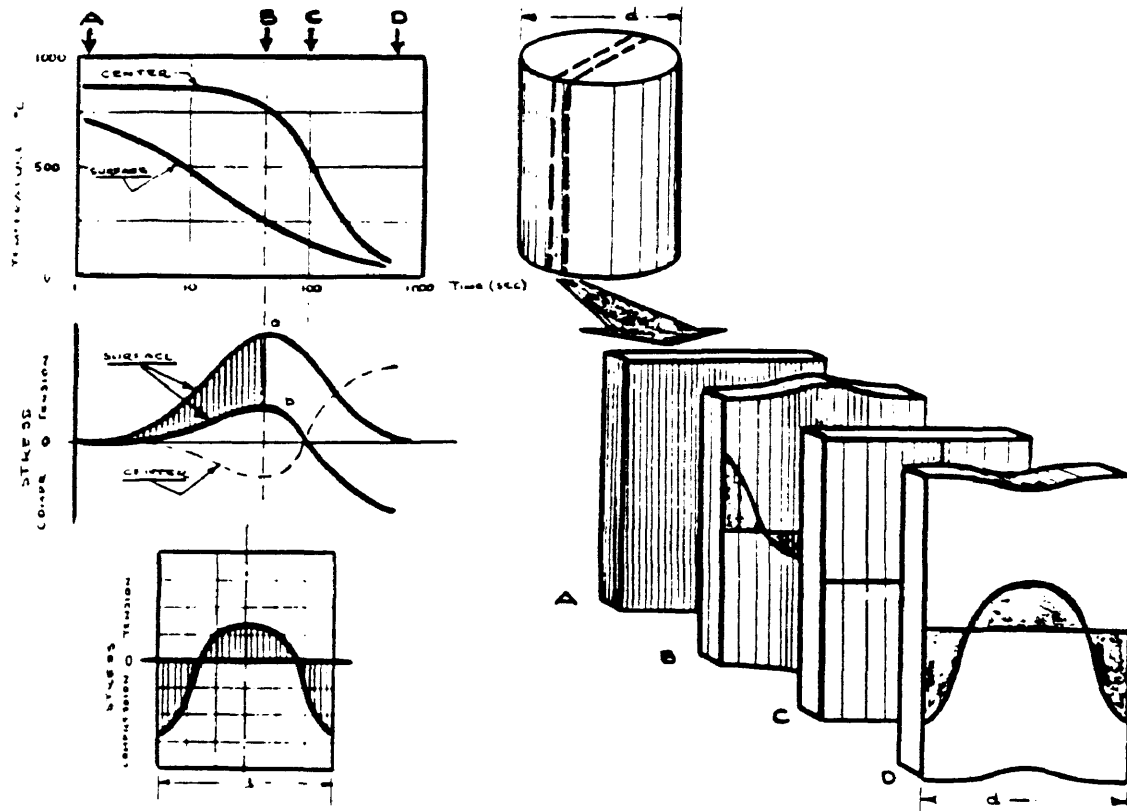


Figure 1.1 Development of residual stress in a cylindrical specimen due to cooling only with no phase transformation (longitudinal stress shown) (10).

temperature where the yield strength of the material is low, a high stress intensity will not develop. A lower level of stress, shown on curve (b), will be present.

The magnitude of the longitudinal stress can induce plastic flow of both the core and center (shortening of the core, lengthening of the center). As cooling continues, the warmer core of the cylinder cools and undergoes its normal contraction but will meet resistance to this contraction from the rigid outer shell (label C). Consequently, the core remains longer than if its contraction were uninhibited by the rigid outer surface and is therefore in a state of residual tension. The outer surface is shorter than as it would be as a free body, because of the tension that the core shrinkage induces. Hence, when the entire body has reached room temperature, the surface is in a state of residual compression and core is in a state of residual tension (label D).

1.3.2 Residual Stress Generation due to a Martensitic Phase Transformation in a Case Carburized Steel Cylinder

The development of residual stress due to a martensitic phase transformation in a carburized steel cylinder is illustrated in Figure 1.2 (10). Residual stress development in case-carburized steel differs from that in a homogeneous material because of the suppressed M_s temperature at the surface. Due to the lower carbon level, the core material

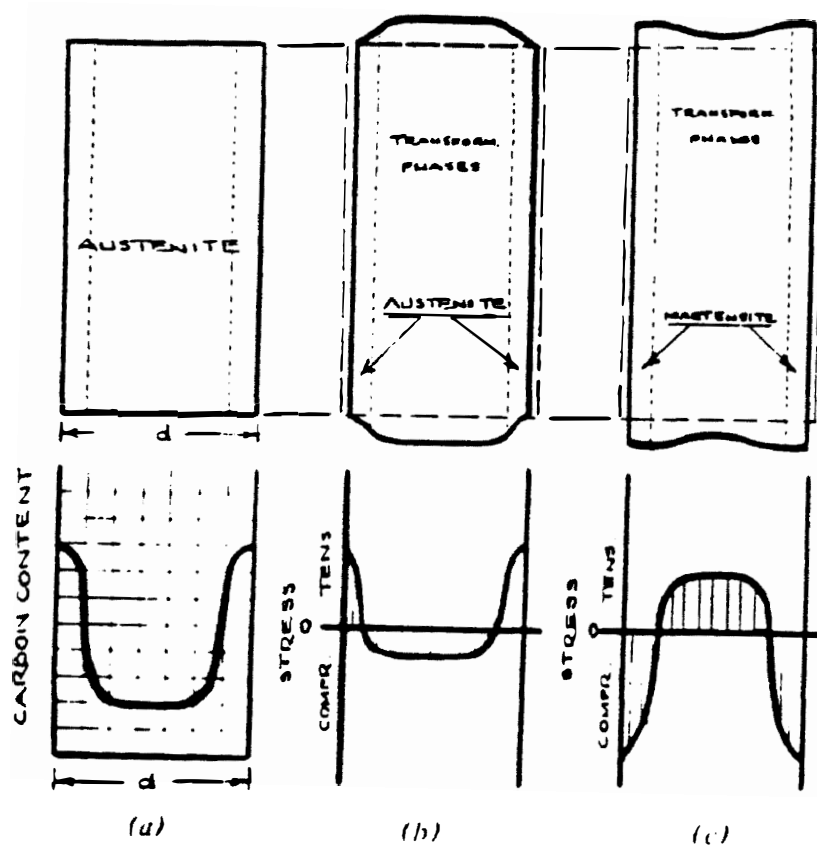


Figure 1.2 Residual stress generation due to a martensitic phase transformation in a carburized steel cylinder (10).

transforms first and the transformation region moves from the core toward the surface. In illustration (a), the steel cylinder is at a uniform high temperature and is uniformly austenite. In illustration (b), the material in the core has undergone a martensitic transformation and corresponding volume expansion producing tensile stress at the surface and compressive stress in the core. The phase transformation and corresponding expansion moves from the core toward the surface as given by the varying M_s temperature. The amount of dilatational expansion also increases with increasing carbon content. In illustration (c), the remaining austenite at the surface transforms to martensite but its corresponding volume expansion is inhibited by an already rigid martensitic core resulting in a high surface compressive stress and a tensile core stress.

1.4 Literature Review

A historical account of analytical and numerical work performed in the area of quenched carburized steel and other alloys prior to 1977 can be found in Burnett (1). Dougherty (4) and Fletcher (7) also discuss various results in the numerical modeling of quenched carburized steel. Selected descriptions of work most influential to this study are discussed below.

Burnett (1) developed a one-dimensional axisymmetric finite element model to calculate the transient generation of residual stress in 0.5 inch diameter SAE 8620 steel cylinders subject to water and oil quenching. Dilatometric data was obtained for various carbon concentrations and temperatures; these data were used in the finite element model, thus combining the thermal and phase transformation strains. The phase transformation was assumed to be martensitic only. The historical thermal behavior was determined from experimental quench tests. Mechanical testing yielded the elastic modulus, the yield strength and strain hardening behavior for the SAE 86XX alloy steel family at elevated temperatures, ranging from 25°C to 927°C. The elastic-plastic constitutive formulation used by Burnett included the von Mises' yield criterion, isotropic hardening and the Prandtl-Reuss flow rule. He also considered yield strength as a function of plastic strain and temperature. The maximum compressive stress was found at about the 0.50% carbon level. Calculated residual stress levels agreed with x-ray diffraction measurements.

Hildenwall (2) and Sjöström (3) studied the residual stress development in rectangular and cylindrical steel geometries subject to oil and water quenching. A variety of alloys were studied. All possible transformation products (i.e. ferrite, pearlite, bainite, martensite and cementite)

were considered. Jominy tests were performed and the results used to numerically model the isothermal and continuous cooling temperature behavior of various alloys. These results were then used to calculate the relative amounts of diffusion controlled transformation products (i.e. ferrite, pearlite, bainite and cementite).

Hildenwall's (2) constitutive equation incorporated the von Mises' yield criterion assuming isotropic hardening, Prandtl-Reuss flow rule and normality rule. Thermal properties were curve-fit from literature data and experimental quench testing. Mechanical property relationships for elastic modulus, the yield strength and the strain hardening behavior as a function of temperature, carbon content and phase were obtained from literature data and experimental testing. Volumetric weighing was used to determine the overall thermal and mechanical behavior of a volume of steel containing more than one phase.

Sjöström's (3) constitutive equation also incorporated the von Mises' yield criterion. Kinematic and mixed hardening behavior were also considered. A discussion of transformation plasticity and a comparison of results are also given. Numerical results by Hildenwall and Sjöström generally agreed with x-ray diffraction measurements.

Studies by Fujio and others (15,16) modeled the distortion and residual stresses in case carburized S45C and SCM21 steel cylinders and spur gears. Thermal, phase transformation, and mechanical properties were determined using experimental testing. Fujio, Aida and Akizono (15) considered a gear geometry with a sufficiently large face width that heat loss was assumed to be in the plane perpendicular to the gear axis only (the face width was greater than the tip cylinder diameter). Although this assumption reduced the thermal and stress analyses to a two-dimensional plane strain problem, the resulting geometry was unrealistic. Numerical and experimental tooth profiles and involute distortions were discussed. In the large face width gear models, the tip cylinder diameter decreased and the involute shape increased after case hardening. Some of the modeled and experimentally measured distortion, however, could be attributed to the large face width geometry. Fujio, Aida, Aratake and Hosoi (16) considered SCM21 steel gears of varying face width that were case-hardened. Three-dimensional thermal analyses were performed. Tip cylinder diameter and involute distortions were significantly influenced by the ratio of tip cylinder diameter to face width.

Dougherty (4) performed two-dimensional axisymmetric thermomechanical finite element analyses using ABAQUS on 86XX alloy steel hollow cylinder models. The mechanical property data used was similar to that used in Burnett (1). The heat treatment process selected consisted of carburizing followed by a double quench. A visco-plastic constitutive model within ABAQUS was used so high temperature creep could also be considered. Sensitivity study results were discussed. The strains associated with the martensitic transformation, creep and the mechanical property data have the most significant effect on distortion and the residual stress state.

2.0 MODELING PROCEDURE USING THE FINITE ELEMENT METHOD

The finite element method is used in this study to numerically determine the distortion and residual stresses generated in carburized SAE 4023 and SAE 4620 alloy steel subject to an oil quench. A custom thermomechanical finite element program, CSMCARB, was written in FORTRAN to perform the analyses.

CSMCARB uses an implicit integration scheme, similar to the Wilson- θ Method, to represent the thermal transients induced by quenching. CSMCARB then computes the transient mechanical response using an incremental elastic-plastic stress analysis.

2.1 Review of Thermomechanical Coupling

A breakdown of the physical interactions between phase, temperature and stress must be understood to model accurately a thermomechanical process. Figure 2.1 (17) illustrates all coupling paths that should be considered to model completely the quench process. Process 1 (phase transformation) represents the effect of temperature on the ferritic, pearlitic, bainitic and martensitic phase transformations in alloy steel. Process 2 (latent heat) represents the endothermic and exothermic effects of various phase transformations, and their contribution to the thermal behavior.

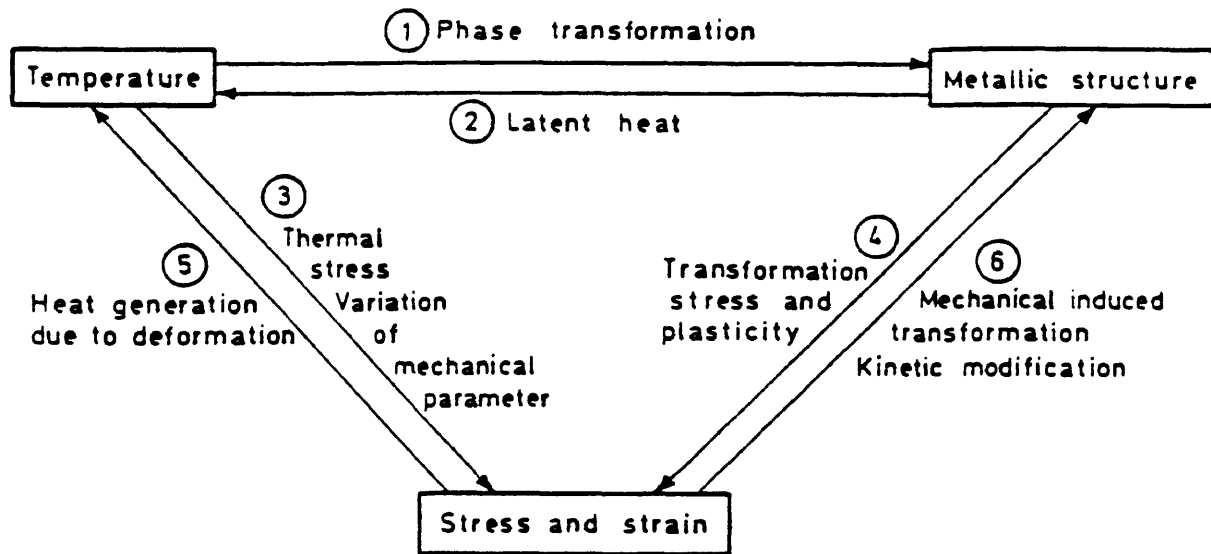


Figure 2.1 Schematic illustrating the interactions for a thermomechanical analysis with phase transformation (17).

Process 3 (thermal stress variation of mechanical parameter) represents the dilatometric thermal strain associated with change in temperature and the material's coefficient of thermal expansion. Process 4 (transformation stress and plasticity) represents the dilatometric strain associated with various phase transformations. Process 5 (heat generation due to deformation) represents heat generation due to large deformations. Process 6 (mechanical induced transformation - kinetic modification) represents variations in phase transformations due to the current stress state in the material.

2.3 Model Material Assumptions

Certain assumptions must be made to model the physical behavior of the steel used for this study. These assumptions are given as follows:

- (1) Homogeneous The model material is assumed to be homogeneous. Microscopic properties including prior austenite grain size, lath, plate and mixed martensite microstructures and inclusion effects are neglected.
- (2) Isotropic The model material is assumed to be isotropic. Anisotropy due to rolling, forging, casting or other forming operations is neglected. Strength differential effects in martensite are neglected (i.e. the initial yield strength in tension and compression are equal).
- (3) Compatible The model continuum is assumed to be compatible. Any development of cracks due to quenching is neglected.
- (4) Non-Viscous The material is assumed to behave independently of strain rate. All strain and stress variations act instantaneously.
- (5) Linear Elastic / Linear Strain Hardening The material is assumed to behave as a linear elastic continuum. The material is also assumed to be represented by a linear strain hardening model, using a constant tangent modulus, E_T .

2.4 Thermomechanical Coupling Assumptions

For this study, three of the six coupling paths discussed in section 2.1 are neglected. The latent heat due to the exothermic martensitic phase transformation is neglected (Process 2, Figure 2.1). The latent heat of transformation has the primary effect of altering the time-temperature behavior of the thermal analysis. Since this study assumes a diffusionless (time-independent) martensitic transformation only, it is reasonable to assume that altering the time-temperature history will not significantly affect the results.

The mechanical heat generation due to deformation is neglected (Process 5, Figure 2.1). This study assumes material nonlinearity only (small strains and small deformations). Therefore, the heat generated mechanically is assumed to be negligible.

Modification of the phase transformation behavior due to the present state of stress is also neglected (Process 6, Figure 2.1). While it is reasonable to assume that the state of stress will either enhance or suppress the martensitic phase transformation (and associated volume expansion), constitutive data supporting such a model are not available. Hence, interaction between phase transformations and current stress is ignored.

2.5 Thermal Analysis and Input Properties

CSMCARB performs a one-dimensional transient thermal analysis using the θ -method, derived in Appendix A. Convective heat loss surface boundary conditions are employed. The thermal analysis iterates to determine the time increment necessary for a specified maximum temperature difference, ΔT .

This analysis incorporates conductivity, specific heat and density as a function of temperature, carbon content, and phase using the cubic relationships presented in (2). A surface convection coefficient, h_c , is modeled as a function

of temperature for steel, quenched in oil. This convection term is also assumed to follow the results presented in (18). These nonlinear thermal properties are also defined in Appendix B.

2.6 Thermal and Phase Transformation Strains

The volumetric fraction of phases present are calculated using Andrew's linear equation (19) and the exponential relationship given by Koistinen and Marburger (20). Only the martensitic phase transformation is considered. Hence, the volumetric fractions thus computed are used to estimate the incremental and total thermal and phase transformation strains. The thermal and phase transformation strains are incrementally applied per load step.

The incremental thermal strains, indicated as $\{\Delta\varepsilon^\theta\}$ (where ε^θ indicates thermal strain and the column vector contains the strains in the X, Y, and Z directions), are calculated using the coefficient of thermal expansion, α , and an incremental change in temperature. This relationship is commonly used in engineering analyses and is presented in Appendix C. A coefficient of thermal expansion as a function of temperature and carbon content is also incorporated (2).

The incremental transformation strains, $\{\Delta\varepsilon^\phi\}$ (where ε^ϕ indicates phase transformation strain and the column vector contains the strains in the X, Y, and Z directions), associated with the formation of martensite, were calculated using a quadratic equation fit to experimental values presented by Hildenwall (2).

Andrew's linear equation (19), Koistinen and Marburger's relationship for the formation of martensite (20), the relationship for the nonlinear coefficient of thermal expansion, α , and the phase transformation strains associated with the ferritic, pearlitic, bainitic and martensitic transformations incorporated in CSMCARB are also given in Appendix B.

2.7 Elastic-Plastic Stress Analysis

CSMCARB performs a 2-D elastic-plastic finite element analysis using an eight-node isoparametric element. A review of continuum and finite element theory applied to elastic-plastic analyses can be found in (21,22,23,24,25). The primary nodal variables are carbon concentration, temperature and displacement. All strain and stress calculations are performed at integration points using two point Gauss-Legendre quadrature numerical integration (21,26).

2.7.1 Elastic-Plastic Constitutive Equation

An incremental elastic-plastic constitutive equation was derived for this analysis. Yield strength, S_y , is assumed to be a function of plastic strain, $\bar{\epsilon}$, and temperature, T . The elastic modulus is also considered to be dependent on temperature. Derivation of the constitutive relationship is given in Appendix C.

2.7.2 Mechanical Input Data

CSMCARB uses the data for elastic modulus as a function of temperature and phase determined by Burnett (1). CSMCARB uses the data for yield strength and strain hardening behavior as a function of temperature, carbon content, and phase given in Hildenwall (2). Poisson's ratio, ν , is assumed to be a constant value of 0.30. The mechanical property data incorporated in CSMCARB are also given in Appendix B.

2.7.3 Stiffness Matrix and Iteration Scheme

CSMCARB uses an elastic stiffness matrix to achieve traction equilibrium (21). The elastic stiffness matrix assured numerical stability and proper plastic-to-elastic transitional behavior. The stiffness matrix was reformed at the beginning of each load step to model increased stiffness with reduced temperature, hence allowing monotonic convergence to equilibrium conditions.

2.7.4 Verification of the Elastic-Plastic Stress Analysis

A rigorous verification procedure was performed using CSMCARB. Selected verification problems used to determine the viability of the constitutive equation and the implementation are presented in Appendix D.

3.0 NUMERICAL AND EXPERIMENTAL PROCEDURE

For this study, a simple plane strain geometry represented a modified version of the Almen strip. Input data used in CSMCARB depict the same physical response as the experimental samples discussed in section 3.2.

This study considers SAE 4023 and SAE 4620 alloy steels, commonly used in carburized gear applications (8). The nominal compositions of these alloys are listed in Table 3.1.

Table 3.1
Alloy Steel Composition

| Average of Ladle Values (wt. %) | | | | | | | |
|---------------------------------|------|------|------|------|-------|-------|------|
| Alloy | C | Mn | P | S | Si | Ni | Mo |
| SAE 4023 | 0.23 | 0.80 | 0.04 | 0.04 | 0.275 | | 0.25 |
| SAE 4620 | 0.20 | 0.55 | 0.04 | 0.04 | 0.275 | 1.825 | 0.25 |

Numerically, the only effect the alloying additions have on this analysis is to modify the martensite start temperature, M_s , and, therefore, alter the phase transformation analysis, discussed in section 2.4.2.

3.1 Input Data Used in CSMCARB

Figure 3.1 illustrates schematically the time-temperature history of the carburizing and quench process. CSMCARB initially determines the carbon profile through the Almen strip thickness, depicted in Figure 3.1 as path A-B, by converting experimentally measured microhardness profiles to nodal carbon values. CSMCARB then performs a one-dimensional transient thermal analysis followed by an incremental elastic-plastic stress analysis for a two stage quench process (oil quench and air cool), depicted as path B-C-D'. This numerically represents the same quench process as that seen by the experimental samples at Chrysler Motor Corporation's Kokomo transmission plant. (The experimental samples were also subjected to a 1.0 hour, 204°C temper, depicted by path C-D, which is beyond the scope of this study.) These input data are also presented in Table 3.2.

Table 3.2
Two Stage Quench Process

| Temperature Range | Quenchant | Quenchant Temperature |
|-------------------|-----------|-----------------------|
| 177°C < T < 871°C | oil | 177°C |
| 25°C < T < 177°C | air | 25°C |

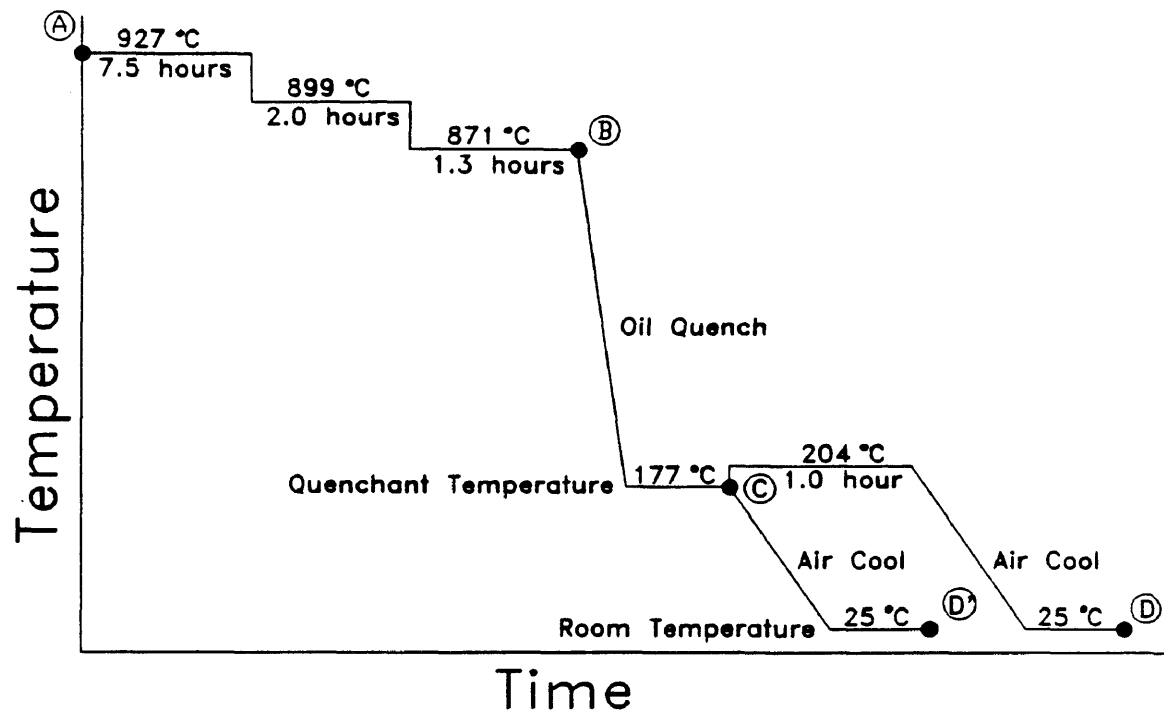


Figure 3.1 Schematic illustrating the time-temperature history of the experimental alloy steel samples.

3.1.1 Finite Element Mesh

The Almen strip is modeled using eight-noded isoparametric elements, each containing four Gauss integration points. Eight-noded isoparametric elements were chosen to improve accuracy while keeping the mesh relatively coarse. This led to improved accuracy (21,26). Figure 3.2 illustrates the finite element mesh used in this study. The model consists of 10 rows by 10 columns of length $0.5 L$ and thickness H (where L and H are the dimensions of the experimental Almen strips given in Table 3.4). The direction of carburizing is also indicated. It is only necessary to model one-half the length of the Almen strip due to symmetry. The element mesh and maximum temperature increment necessary for this analysis is discussed further in sections 3.1.3 and 4.0.

3.1.2 Carbon Profile Determination

Carbon profiles were calculated from experimental measurements. Microhardness traverses across the thickness of each of the five Almen geometries of SAE 4023 and SAE 4620 were performed. The results were then curve-fit using data regression to fourth order polynomial equations. Hardness (in HRC) as a function of depth was then converted to carbon concentration (in weight percent carbon) as a function of depth using the relationship presented in (27)

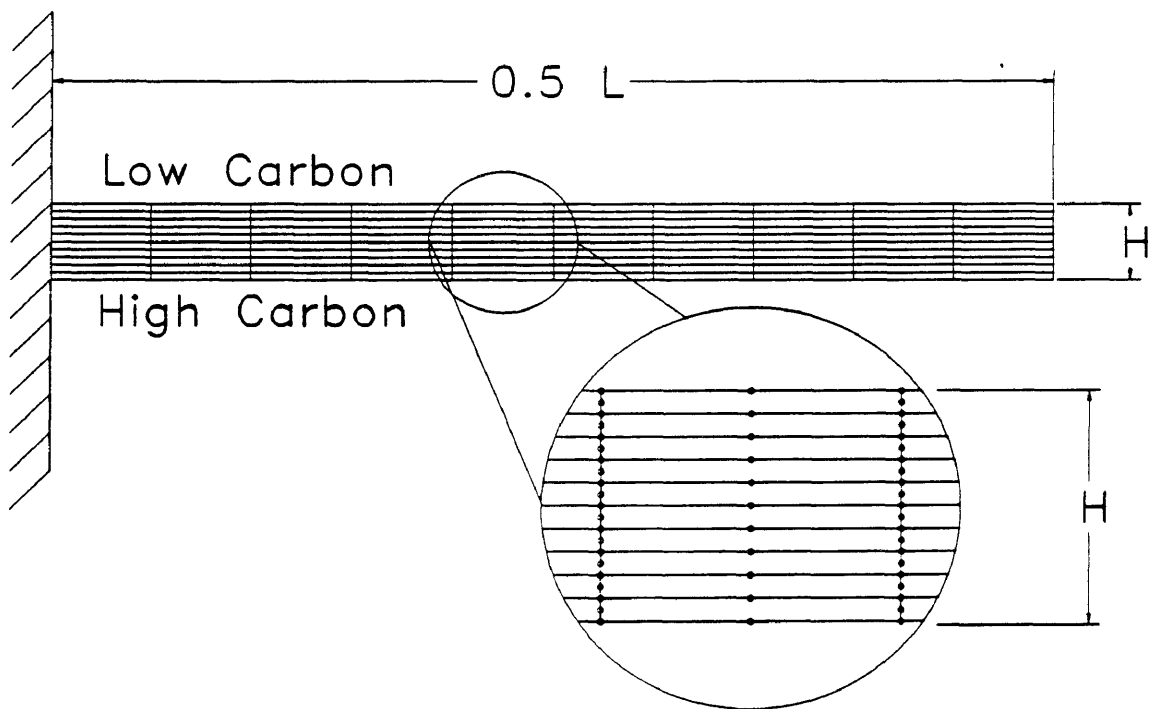


Figure 3.2 Finite element model used in this study consisting of 10 rows by 10 columns of eight noded isoparametric elements. The lower surface is the high carbon surface.

for hardness as a function of carbon concentration for 400°F tempered martensite. Results of this method are presented in section 4.1.

It should be noted that several attempts were made to simulate the carburizing process numerically. The methods used included a one-dimensional forward explicit finite difference scheme, a one-dimensional Crank-Nicholson finite element scheme and a one-dimensional finite element scheme incorporating the θ -method. The Crank-Nicholson and θ -method finite element schemes oscillated numerically unless a sufficiently refined mesh is employed (100 or more node points). This is primarily due to the magnitude of carbon diffusivity in the stiffness matrix (on the order of 10^{-9} m²/sec) and the assumption that the surface carbon concentration instantaneously is that of saturated carbon in austenite. The carbon profile results using the forward explicit finite difference scheme did not agree with the experimental microhardness profiles (using the conversion method described above). This was primarily due to a lack of input information, specifically, the surface carbon concentration at the various carburizing temperatures. The surface carbon concentration cannot be assumed constant for the carburizing stage. Furnace geometry, gas atmosphere, the amount of steel in the furnace, and carbon accumulation on the component surface must be considered to calculate

properly the transient surface carbon concentration during the carburizing stage.

3.1.3 Spatial and Temperature Convergence Study

A study was performed to determine the necessary refinement of spatial mesh necessary for numerical convergence of the elastic-plastic stress analysis. Figure 3.3 illustrates the deflection history of the 2.03 millimeter Almen strip model using spatial meshes of 6x6, 8x8, 10x10 and 12x12 elements with a maximum temperature increment of -2.5°C . Positive deflection is defined as a convex curvature of the high carbon side of the Almen strip model. Figure 3.4 illustrates the resulting axial stress (τ_{xx}) distribution for the 2.03 millimeter Almen strip model for the various indicated meshes at 25°C . Stress in tension is depicted as positive.

A study was performed to determine the maximum temperature difference, ΔT , necessary for numerical convergence of the elastic-plastic stress analysis. Figure 3.5 illustrates the deflection history of the 2.03 millimeter Almen strip model using a spatial mesh of 5x5 elements and maximum temperature increments, ΔT , of -5.0°C , -2.5°C , -1.0°C and -0.5°C . Figure 3.6 illustrates the resulting axial stress (τ_{xx}) distribution for the 2.03 millimeter Almen strip model using a spatial mesh of 5x5

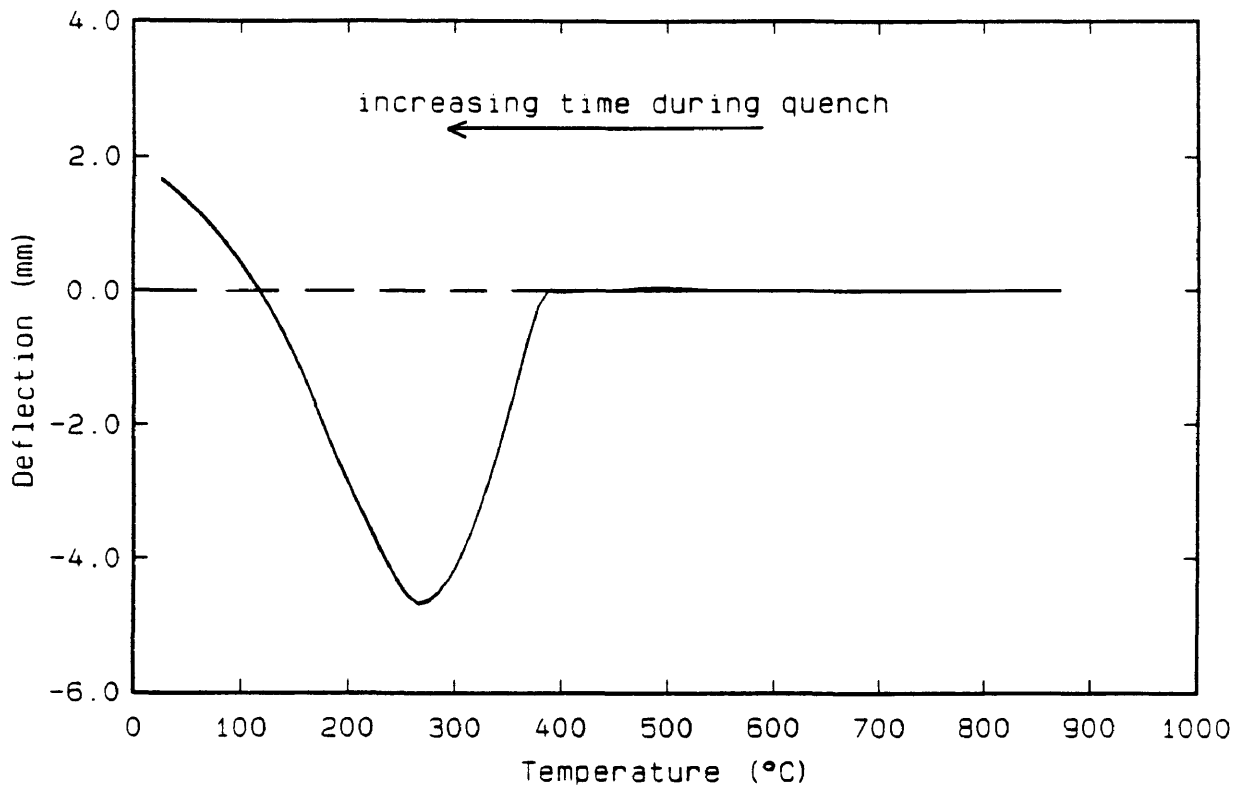


Figure 3.3 Deflection history for the 2.03 millimeter Almen strip model using spatial meshes of 6x6, 8x8, 10x10 and 12x12 elements. The maximum temperature increment is -2.5°C . The analysis begins at 871°C and continues to 25°C .

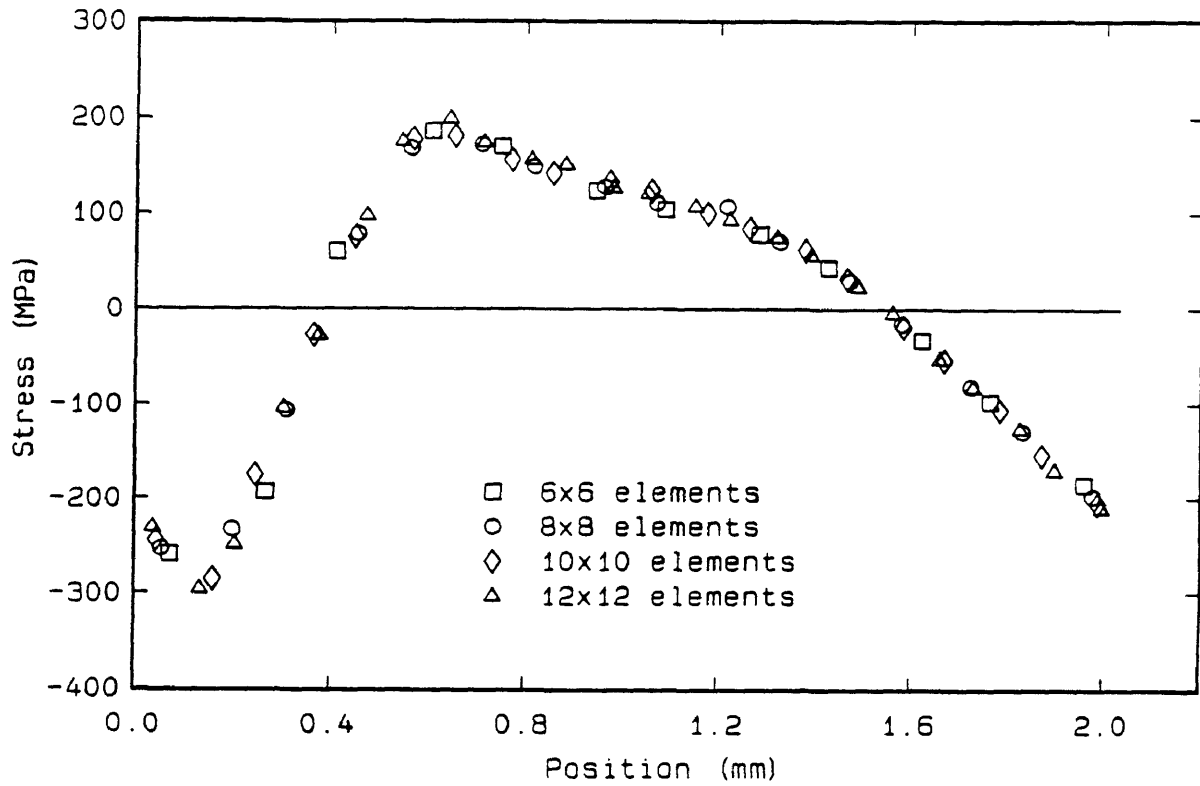


Figure 3.4 Axial stress (τ_{xx}) distribution at 25°C for the 2.03 millimeter Almen strip model using various indicated meshes and a maximum temperature increment of -2.5°C.

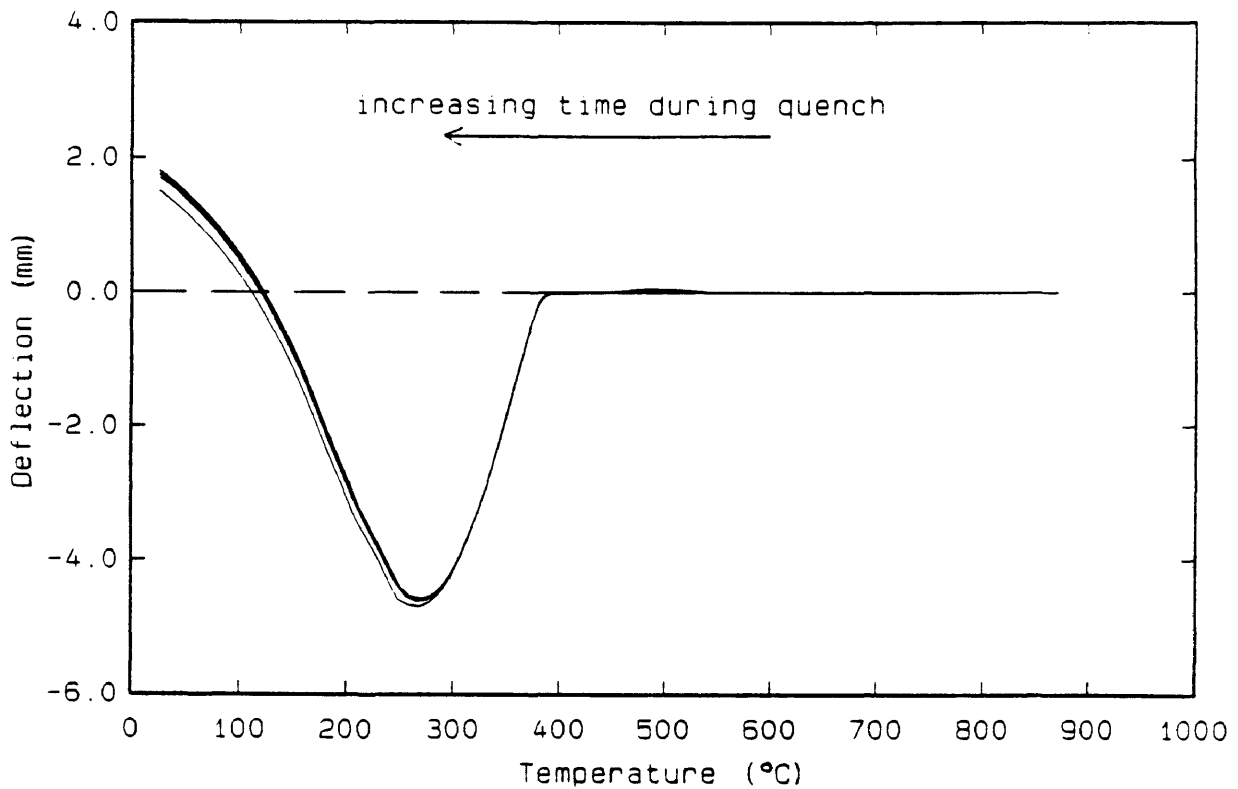


Figure 3.5 Deflection history of the 2.03 millimeter Almen strip model using a spatial mesh of 5x5 elements. Maximum temperature increments, ΔT , of -5.0°C , -2.5°C , -1.0°C and -0.5°C are shown. The analysis begins at 871°C and continues to 25°C .

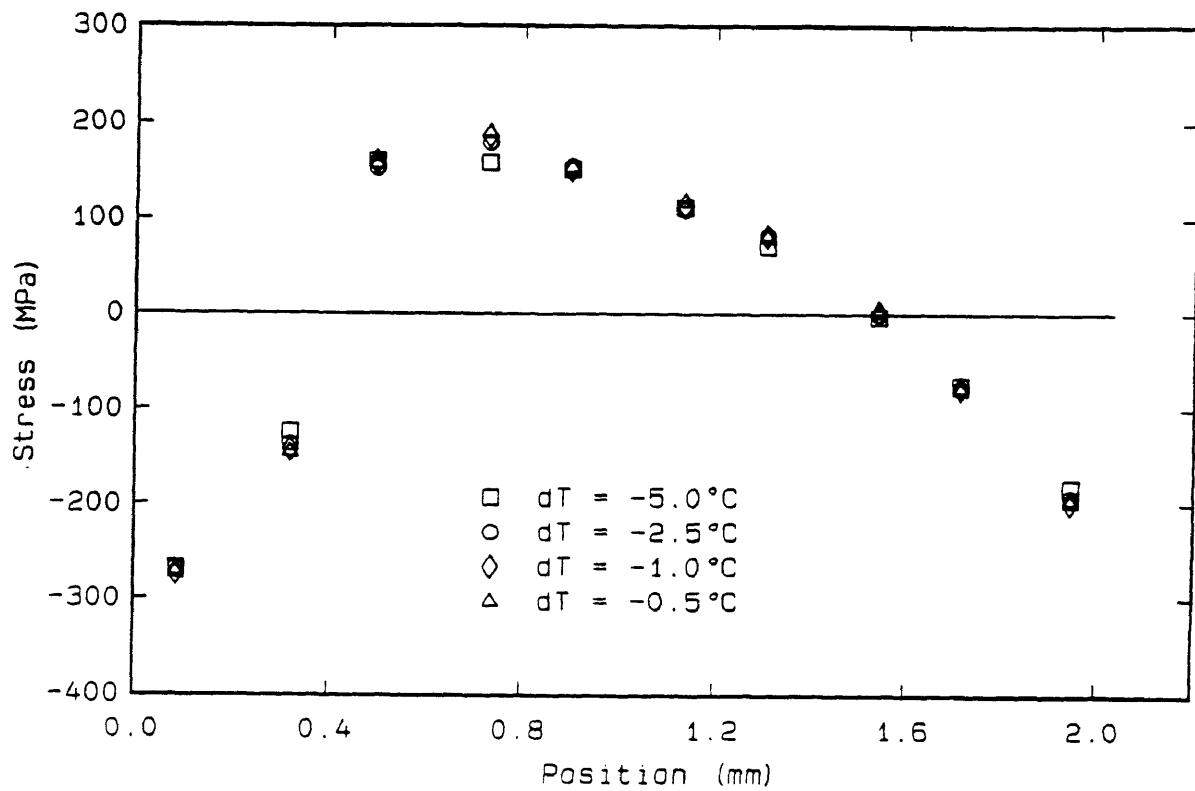


Figure 3.6 Axial stress (τ_{xx}) distribution at 25°C for the 2.03 millimeter Almen strip model using a spatial mesh of 5x5 elements and the various indicated maximum temperature increments.

elements at 25°C for the various temperature differences, ΔT . Based on the results of the spatial and maximum temperature convergence studies, a spatial mesh of 10x10 elements and maximum temperature difference, ΔT , of -1.0°C is sufficient for proper numerical convergence of the elastic-plastic stress analysis.

3.2 Verification Procedure - The Modified Almen Strip Test

The Almen strip test is commonly used as a calibration test in the shot peening industry to determine the impact energy (peening intensity) of the shot stream. The Almen strip test, developed by J.O. Almen of General Motors Research Laboratories, incorporates SAE 1070 spring steel specimens of varied thickness, as illustrated in Figure 3.7 (28). The Almen strip, while held to a fixture, is subjected to a shot stream on one side only (a). Relieving the resulting compressive residual stress on the shot peened surface (caused by the applied cold work during the process) results in a measurable arc deflection with the shot peened surface convex when viewed from above (b). This deflection can then be related to residual stress depth and magnitude (c).

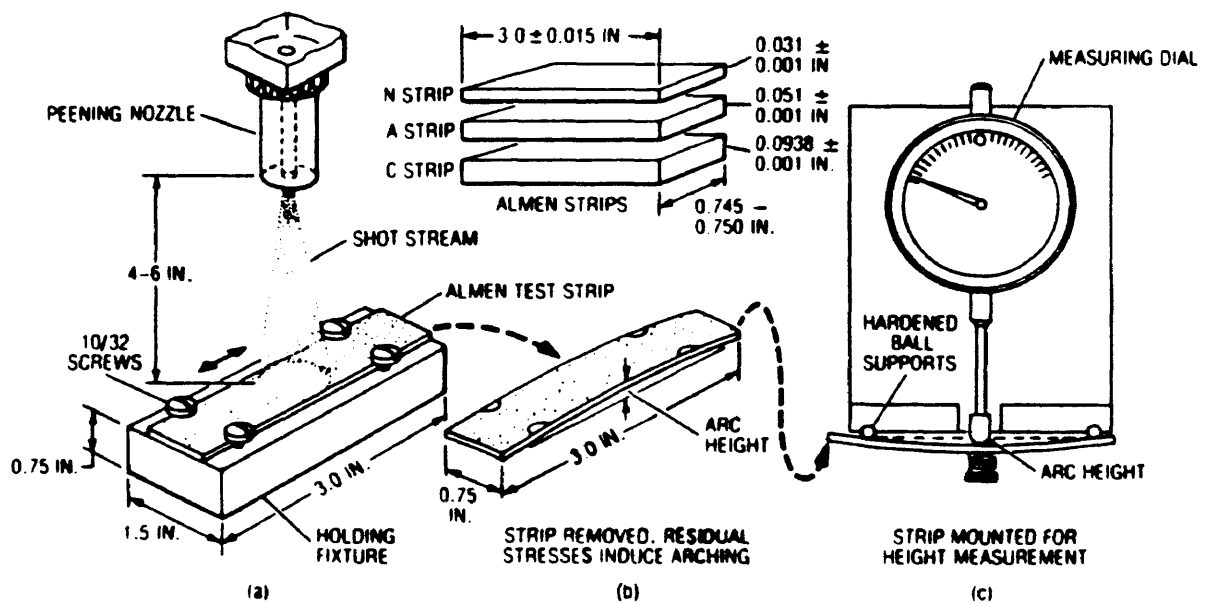


Figure 3.7 Illustration of the Almen strip test commonly used in shot peening application to determine the intensity of the peening process (28).

In this study, a modified Almen strip test was performed where thin strips of SAE 4023 and SAE 4620 alloy steel were carburized on one side only and quenched. Variations in thermal and mechanical properties over the thickness due to a carbon gradient produced an arc deflection similar to the shot peen test with the high carbon surface convex. This was primarily due to a higher volume expansion for the high carbon martensite.

3.2.1 As-Received Material

As received material consisted of SAE 4023 and SAE 4620 50.8 millimeter nominal diameter bar stock sent from Chrysler Motors Corporation's Kokomo transmission plant. Microscopy indicated a ferritic-pearlitic microstructure with average as-received hardness indicated in Table 3.3. Hardness traverses across the bar diameter did not significantly vary indicating that the bar stock reduction was sufficient to eliminate any material anisotropy.

Table 3.3
As-Received Hardness

| Alloy | HRB |
|-------------------------------|--------|
| SAE 4023 | 81.8 |
| SAE 4023 | 84.1 * |
| SAE 4620 | 85.4 |
| SAE 4620 | 88.5 * |
| * Diamond Pyramid → VHN → HRB | |

3.2.2 Almen Strip Preparation and Testing

Almen strips of SAE 4023 and SAE 4620 alloy steel were milled and precision ground to five thicknesses, as indicated in Table 3.4.

Table 3.4
Geometry of Experimental Almen Strips

| Alloy | Length, L * | Width, W * | Thickness, H ** |
|--------------------------------|-------------|------------|-----------------|
| SAE 4023 | 100 mm | 20 mm | 1.30 mm |
| SAE 4620 | 100 mm | 20 mm | 1.30 mm |
| SAE 4023 | 100 mm | 20 mm | 1.85 mm |
| SAE 4620 | 100 mm | 20 mm | 1.85 mm |
| SAE 4023 | 100 mm | 20 mm | 2.03 mm |
| SAE 4620 | 100 mm | 20 mm | 2.03 mm |
| SAE 4023 | 100 mm | 20 mm | 2.44 mm |
| SAE 4620 | 100 mm | 20 mm | 2.44 mm |
| SAE 4023 | 100 mm | 20 mm | 3.18 mm |
| SAE 4620 | 100 mm | 20 mm | 3.18 mm |
| * Nominal ** ± 0.025 mm | | | |

Two samples of each alloy and thickness were prepared for a total of 20 Almen strips. To minimize any residual stresses due to machining, the Almen strips were stress relieved for one hour at 500°C (9).

Carbon diffusion into the steel sample from one side only was achieved by taping one side of the Almen strips with standard black electrical tape, then plating the samples with 0.050 millimeters \pm 0.025 millimeters of copper. Ajax Custom Plating, Englewood, CO, performed the plating using an acid copper plating procedure. The diffusivity of carbon in copper at the carburizing

temperatures of interest is negligible compared to the diffusivity of carbon in austenitic steel, therefore, the copper plating is essentially a diffusion barrier. The samples were then sent to Tony Freda, Product Engineer at Chrysler Motors Corporation's Kokomo Transmission Plant, where they underwent a 3 stage, 10.8 hour carburizing process followed by an oil quench, temper and air cool, as described in section 3.1.

4.0 EXPERIMENTAL AND NUMERICAL RESULTS

A comparison of experimental to numerical results is presented in the following sections. Numerical results were obtained using an element mesh consisting of 10 rows by 10 columns using a maximum temperature increment of -1.0°C .

4.1 Microhardness, Carbon and M_s Profiles

Microhardness measurements across the thickness of each Almen strip was obtained using the diamond pyramid indentation method. These data were then curve-fit to fourth order polynomial equations using data regression. Figures 4.1-4.5 illustrate the measured and curve-fit microhardness traverses for the various thicknesses of SAE 4023 Almen strips. Similar microhardness profiles were obtained for the SAE 4620 Almen strips.

Carbon profiles for the five thicknesses of each alloy were calculated using the method described in section 3.1.2. Figures 4.6-4.10 illustrate the calculated carbon profiles for the various thicknesses of SAE 4023 Almen strips. Similar carbon profiles were obtained for the SAE 4620 Almen strips.

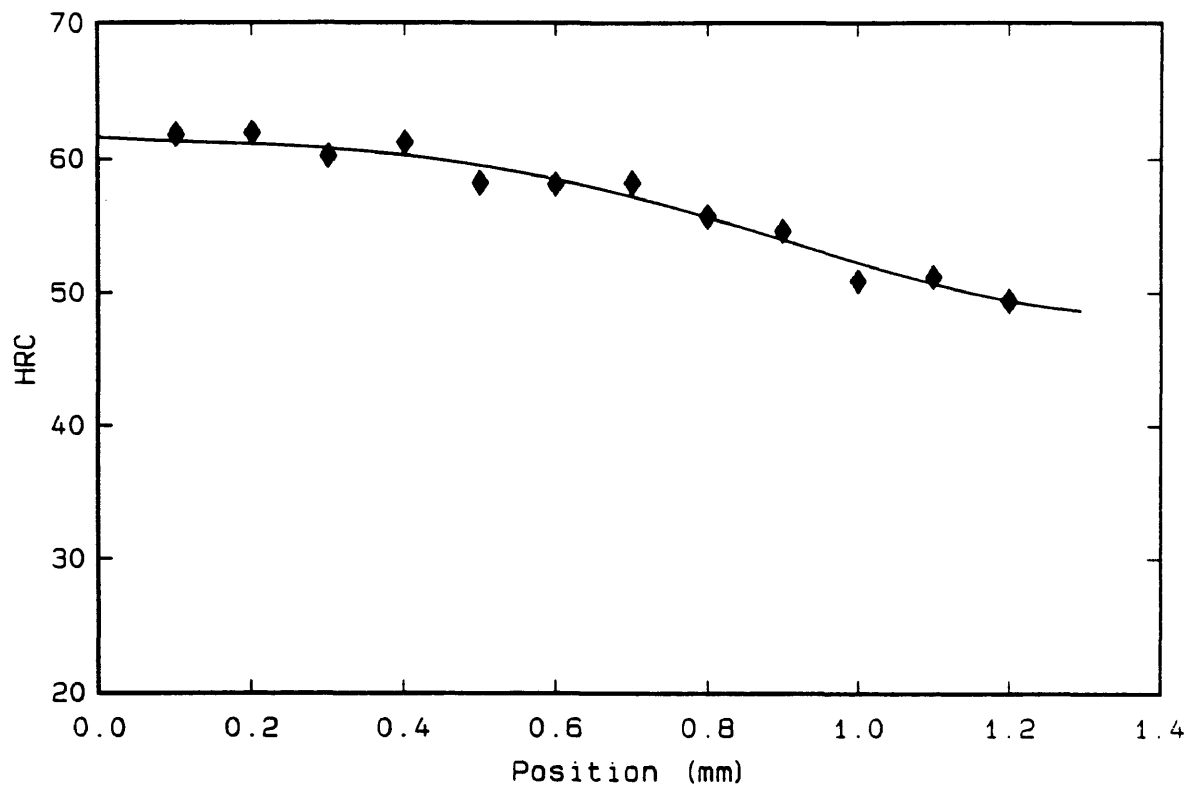


Figure 4.1 Experimental microhardness profile for the 1.30 millimeter SAE 4023 Almen strip.

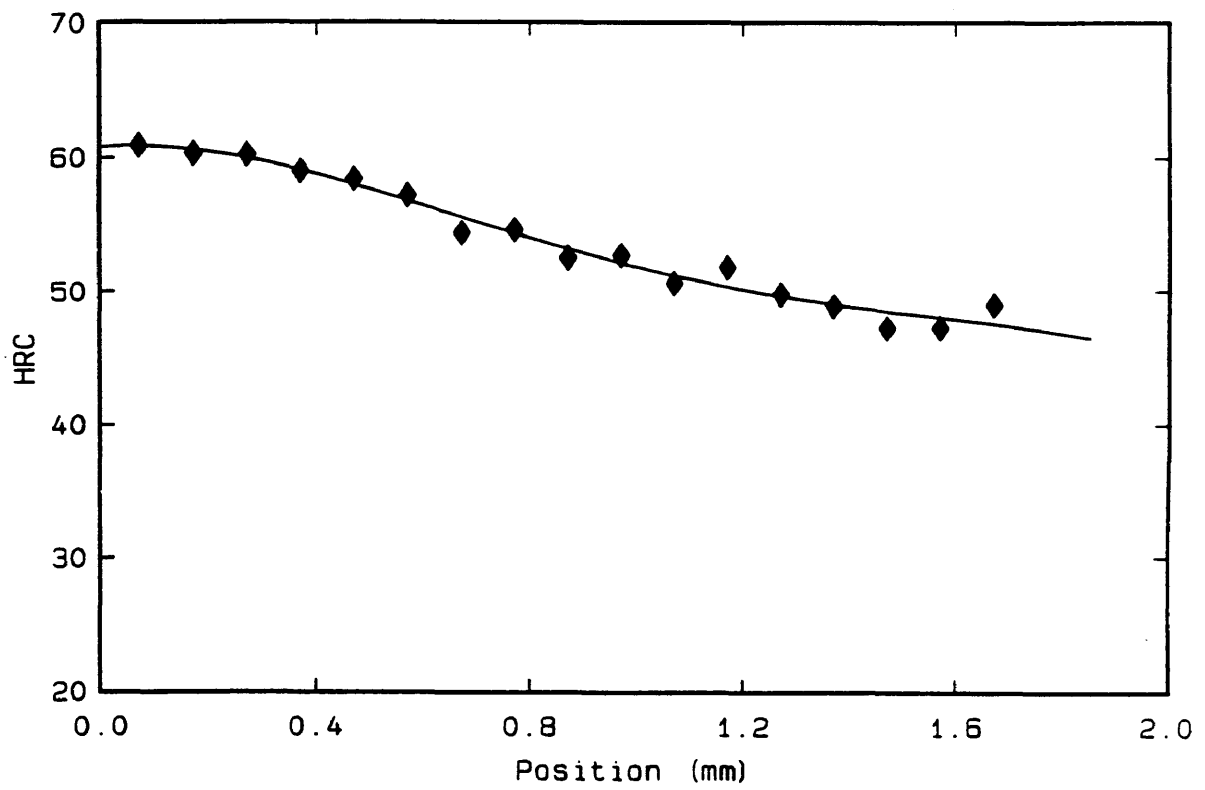


Figure 4.2 Experimental microhardness profile for the 1.85 millimeter SAE 4023 Almen strip.

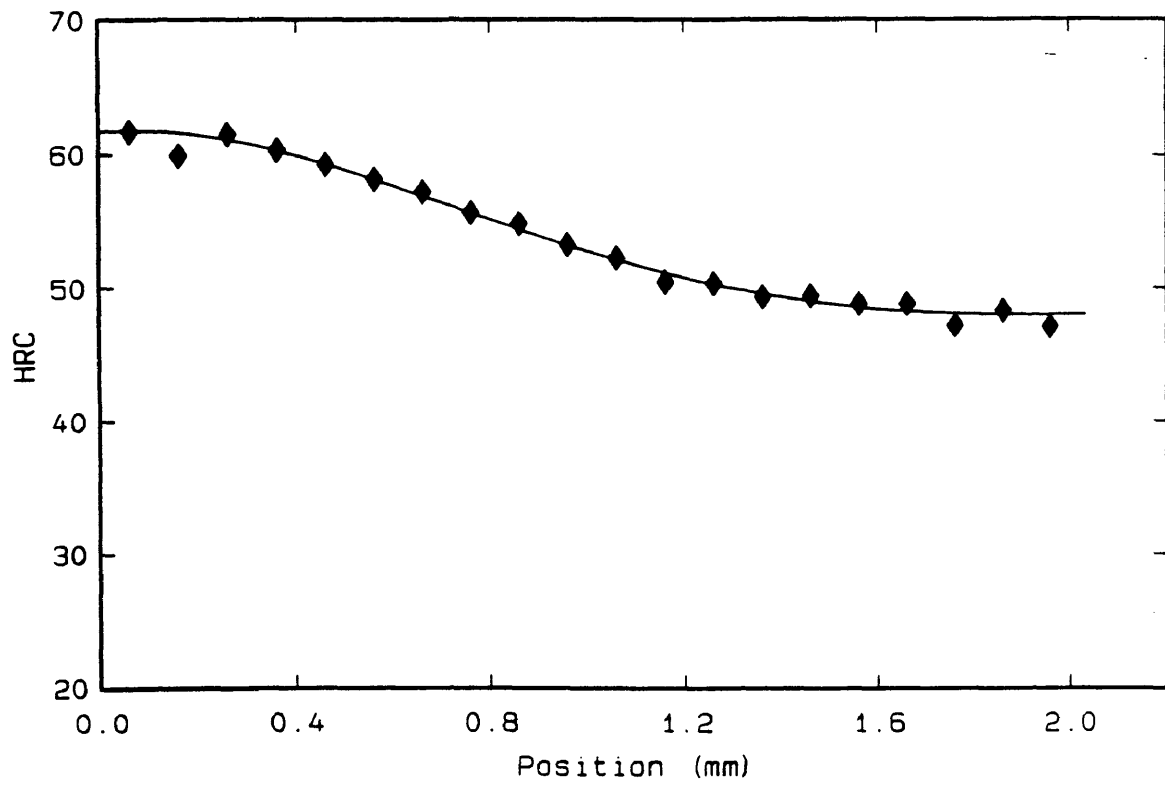


Figure 4.3 Experimental microhardness profile for the 2.03 millimeter SAE 4023 Almen strip.

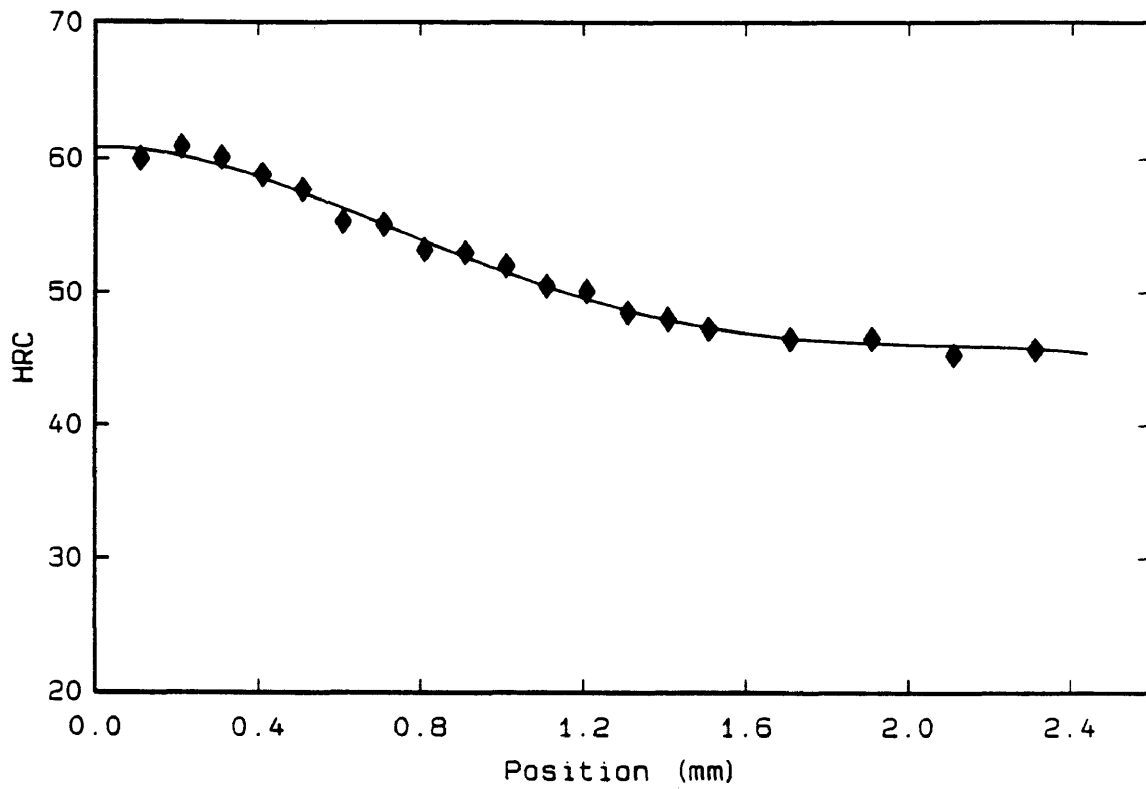


Figure 4.4 Experimental microhardness profile for the 2.44 millimeter SAE 4023 Almen strip.

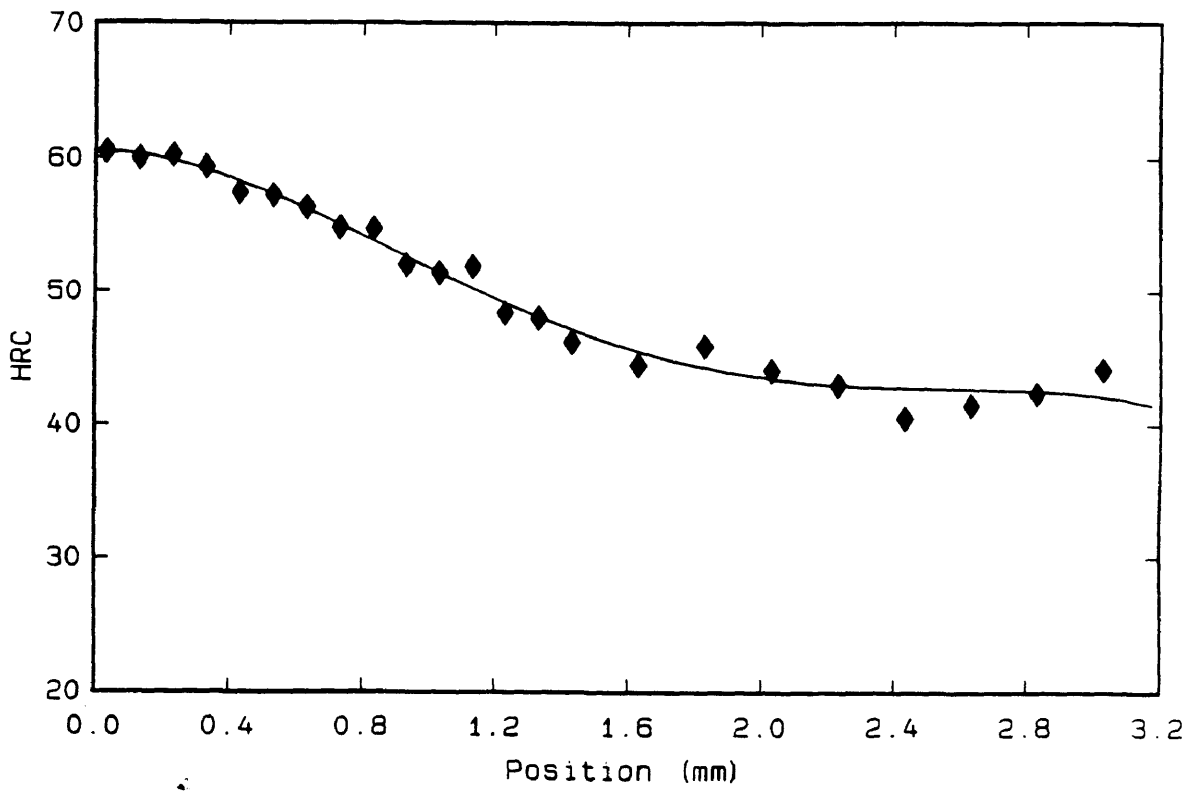


Figure 4.5 Experimental microhardness profile for the 3.18 millimeter SAE 4023 Almen strip.

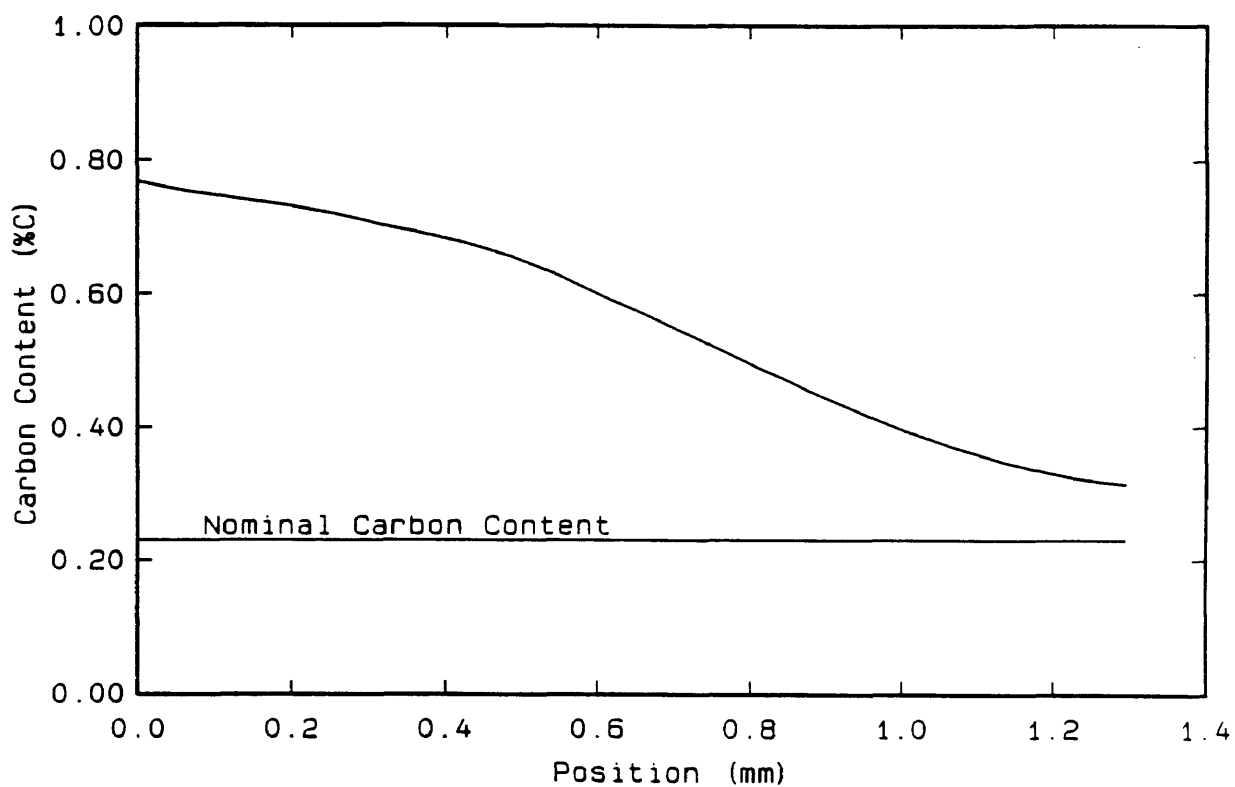


Figure 4.6 Carbon profile determined from microhardness data for the 1.30 millimeter Almen strip of SAE 4023 alloy steel.

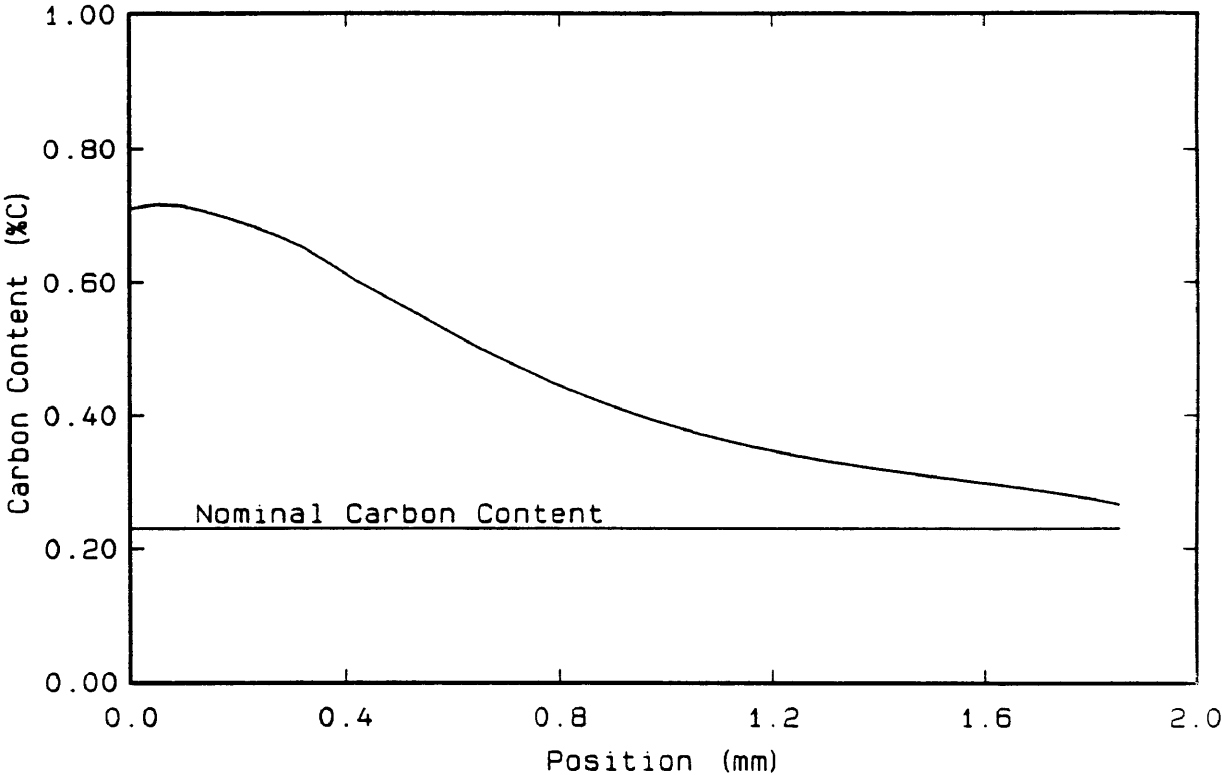


Figure 4.7 Carbon profile determined from microhardness data for the 1.85 millimeter Almen strip of SAE 4023 alloy steel.

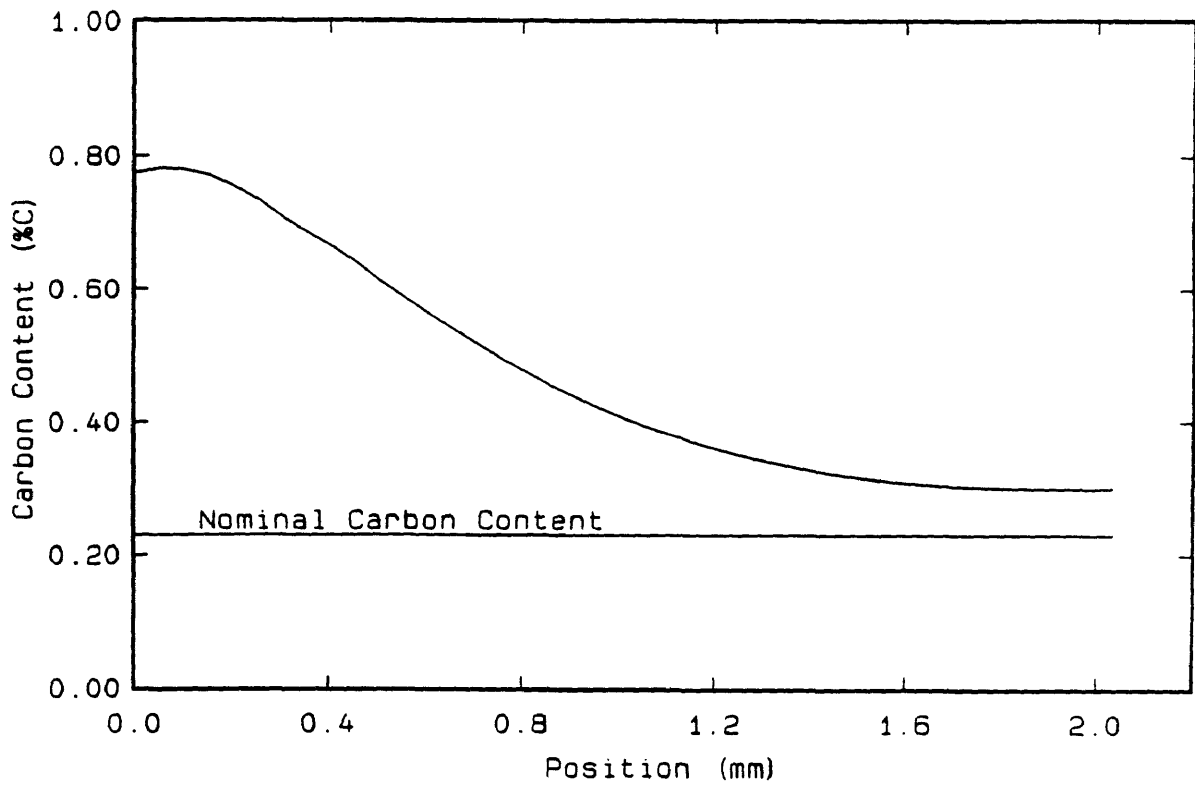


Figure 4.8 Carbon profile determined from microhardness data for the 2.03 millimeter Almen strip of SAE 4023 alloy steel.

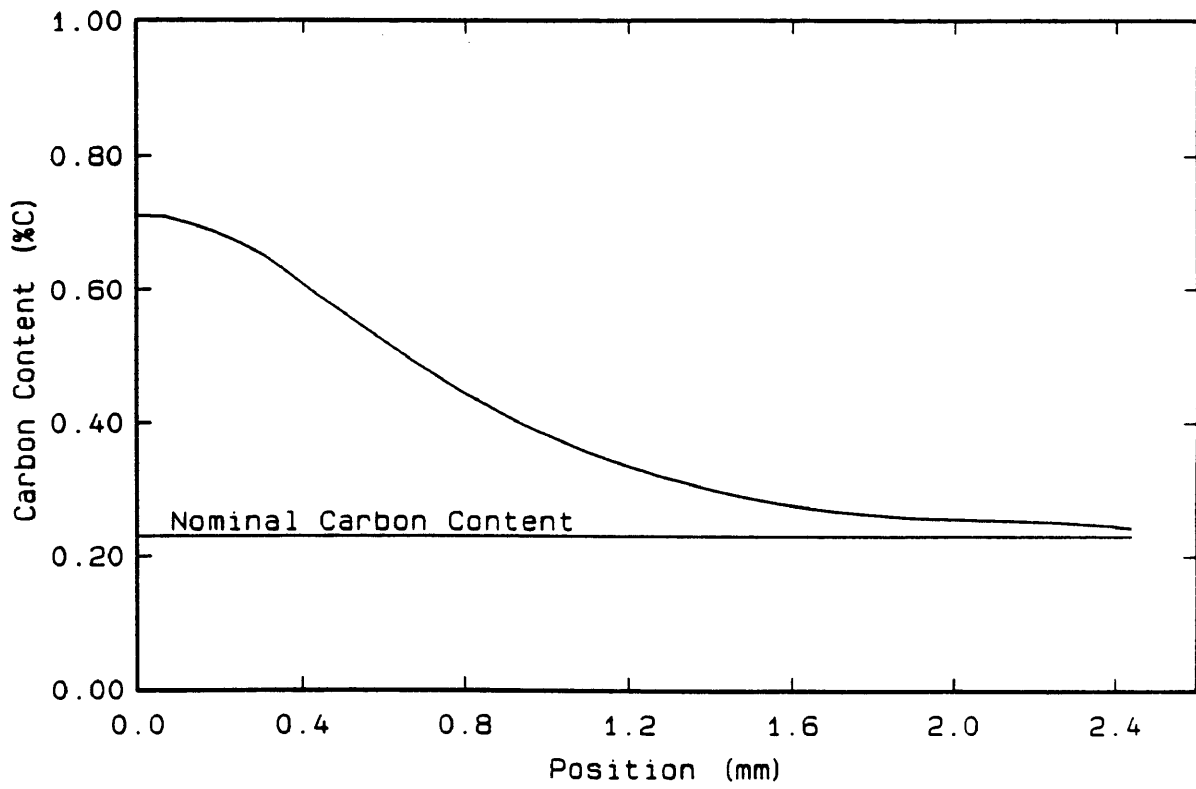


Figure 4.9 Carbon profile determined from microhardness data for the 2.44 millimeter Almen strip of SAE 4023 alloy steel.

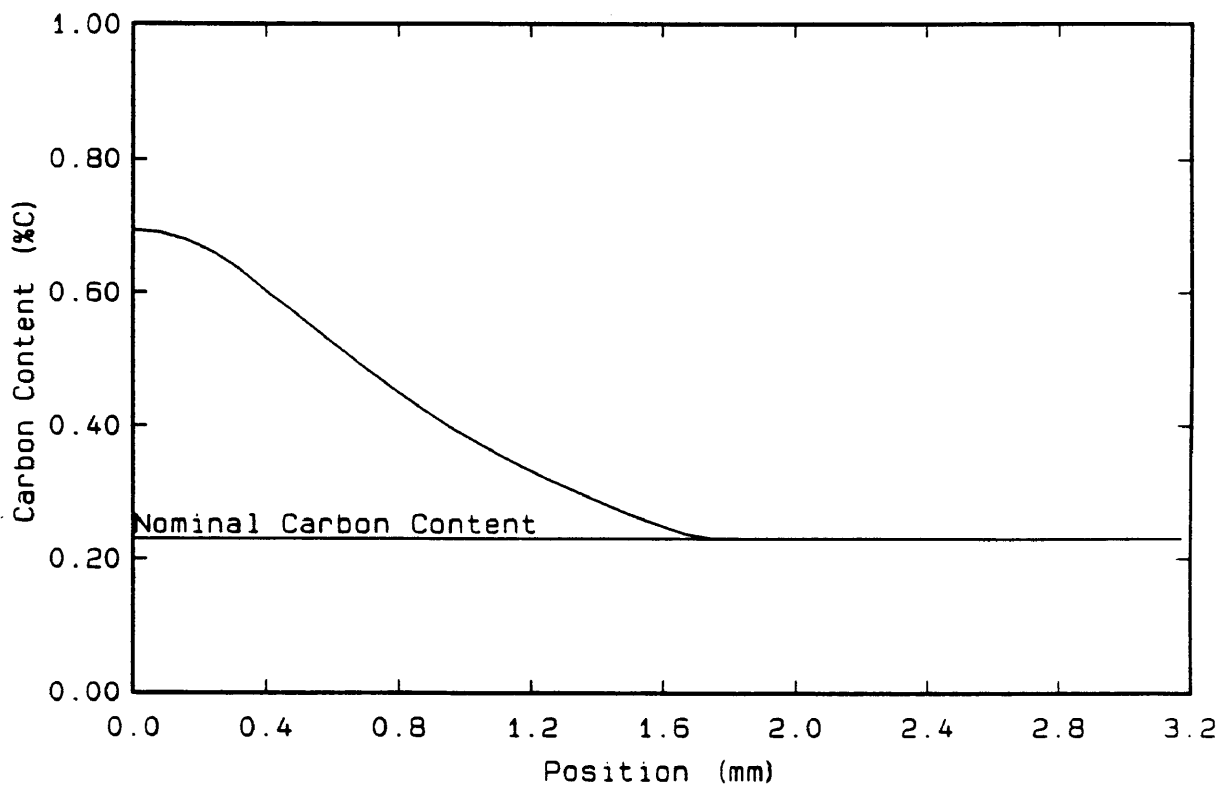


Figure 4.10 Carbon profile determined from microhardness data for the 3.18 millimeter Almen strip of SAE 4023 alloy steel.

The corresponding profiles for martensite start temperature, M_s , were determined using Andrew's linear equation (19). Figures 4.11-4.15 illustrate the calculated M_s profiles for the various thicknesses of SAE 4023 Almen strips. Similar M_s profiles were obtained for the SAE 4620 Almen strips.

The calculated M_s profiles determine the transient formation of martensite, as explained in section 2.4.2. Figures 4.16-4.20 illustrate the calculated percentage of martensite through the various thicknesses of SAE 4023 Almen strips at 25°C.

4.2 Experimental and Numerical Deflection Results

The experimental Almen strips were measured to determine the maximum arc deflection resulting from the carburizing and quench processes. Figures 4.21 and 4.22 illustrate the deflected shape of the SAE 4023 Almen strips. Table 4.1 indicates the final measured arc deflection for the twenty Almen strips tested.

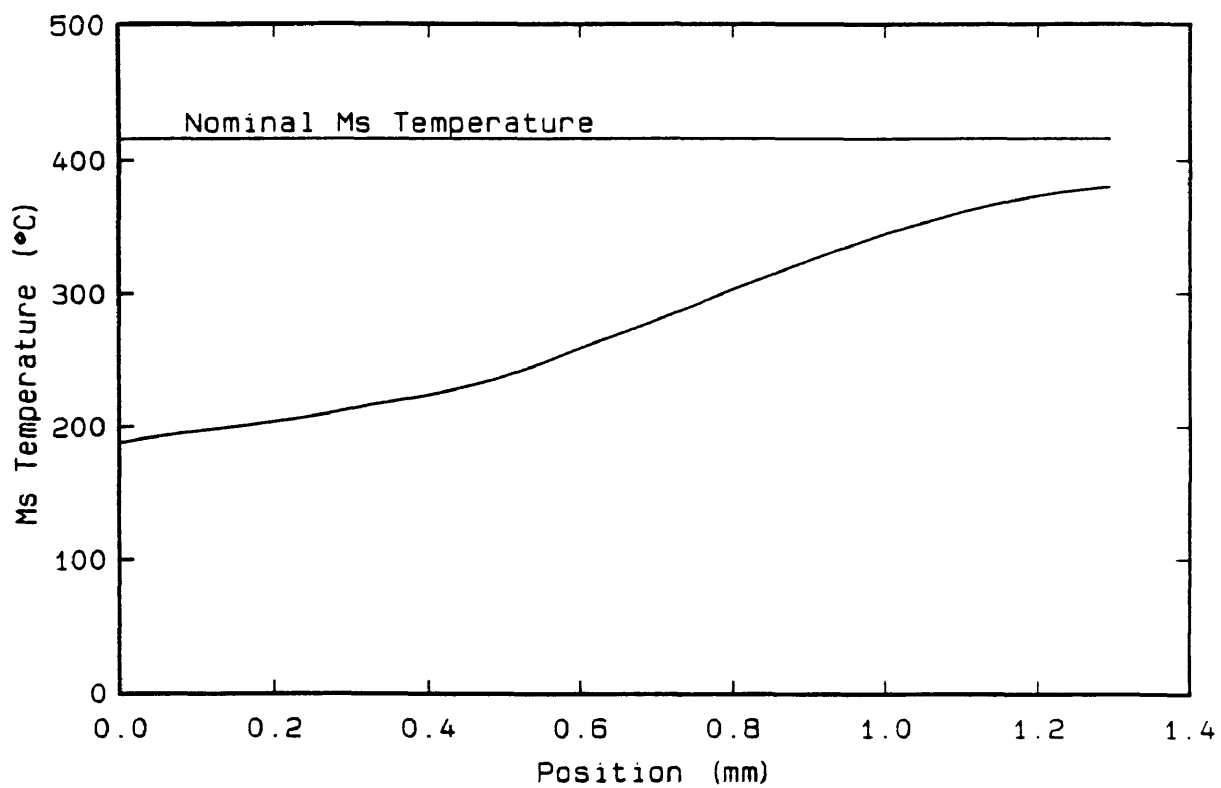


Figure 4.11 Calculated M_s profile for the 1.30 millimeter Almen strip of SAE 4023 alloy steel.

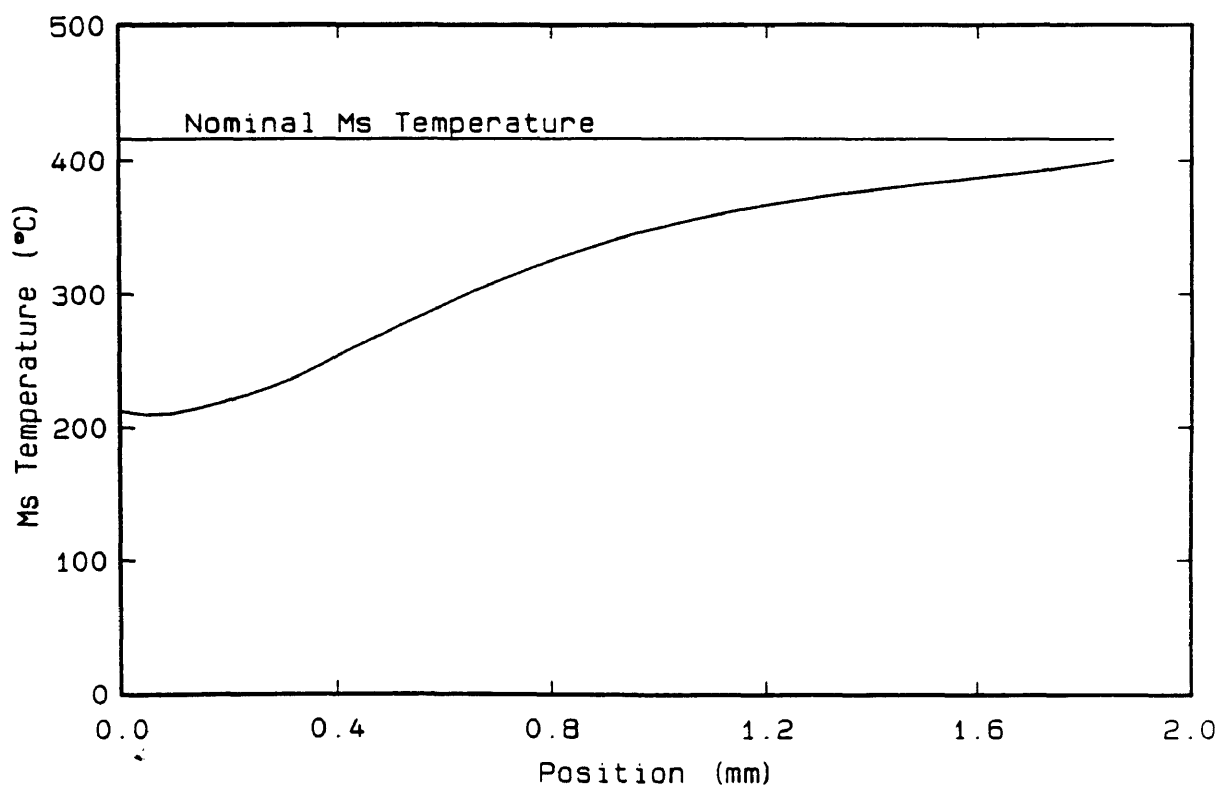


Figure 4.12 Calculated M_s profile for the 1.85 millimeter Almen strip of SAE 4023 alloy steel.

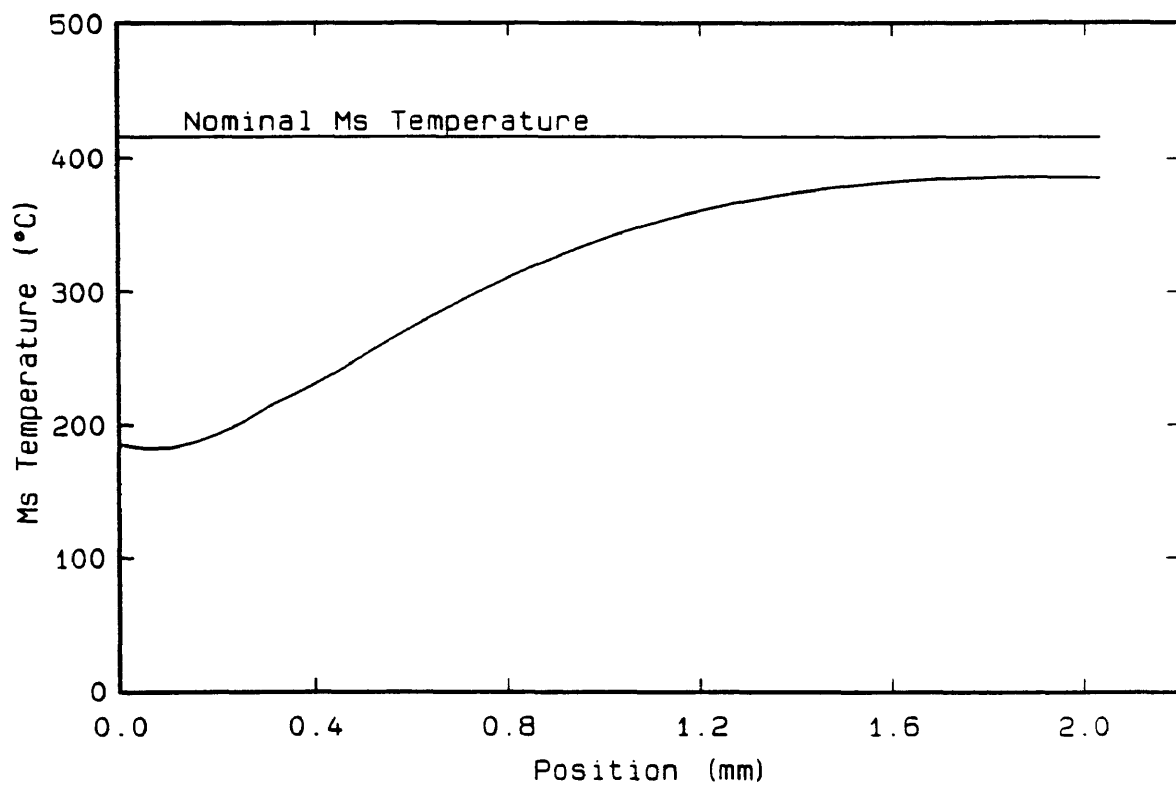


Figure 4.13 Calculated M_s profile for the 2.03 millimeter Almen strip of SAE 4023 alloy steel.

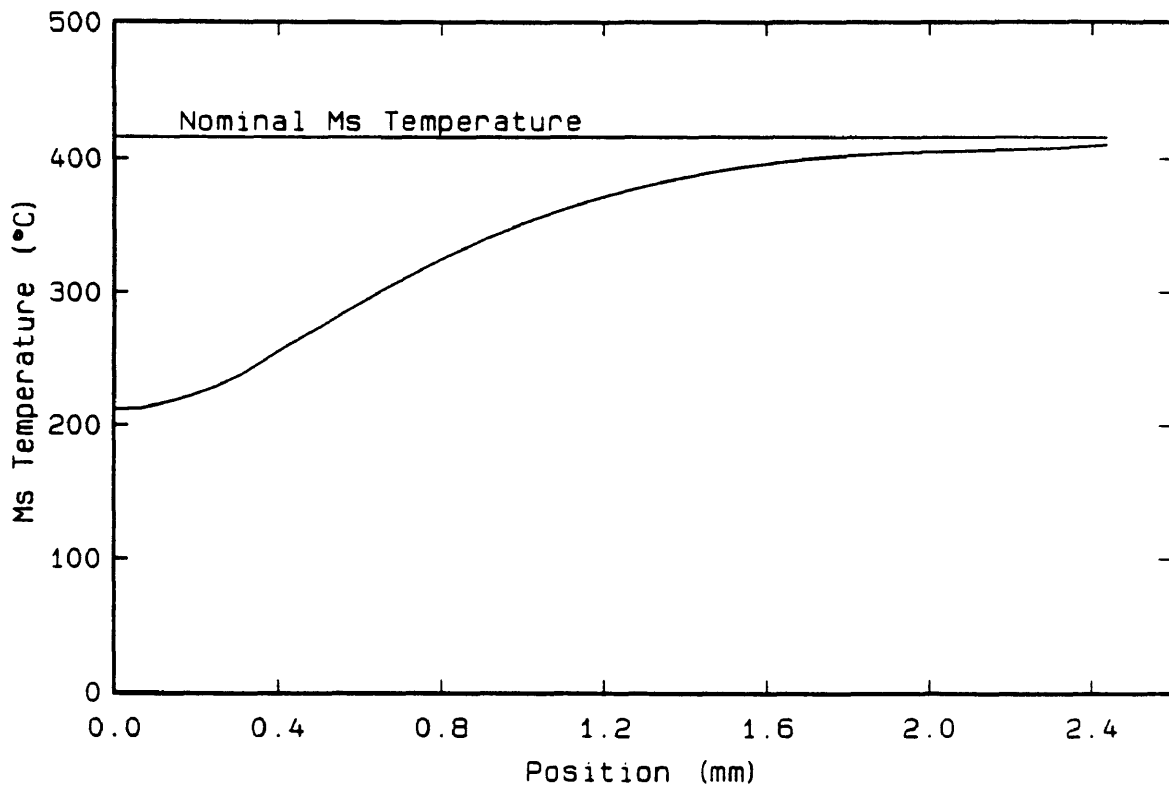


Figure 4.14 Calculated M_s profile for the 2.44 millimeter Almen strip of SAE 4023 alloy steel.

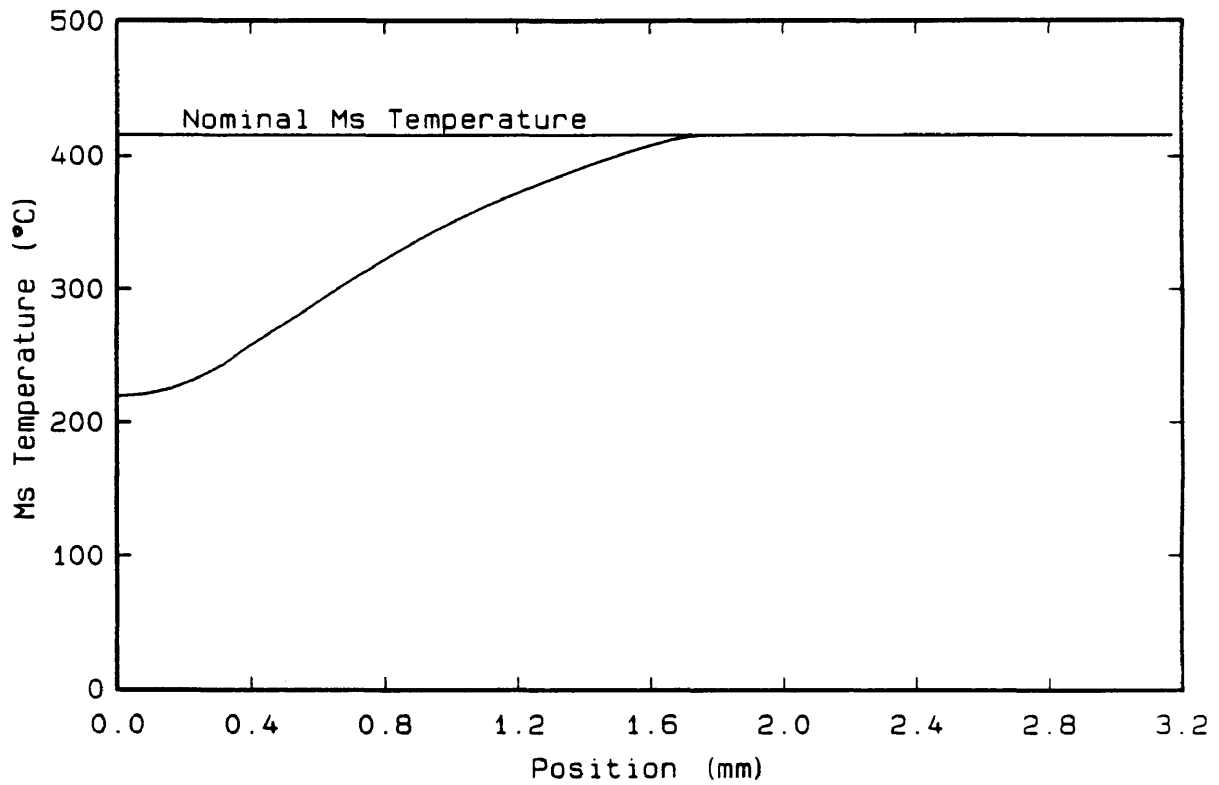


Figure 4.15. Calculated M_s profile for the 3.18 millimeter Almen strip of SAE 4023 alloy steel.

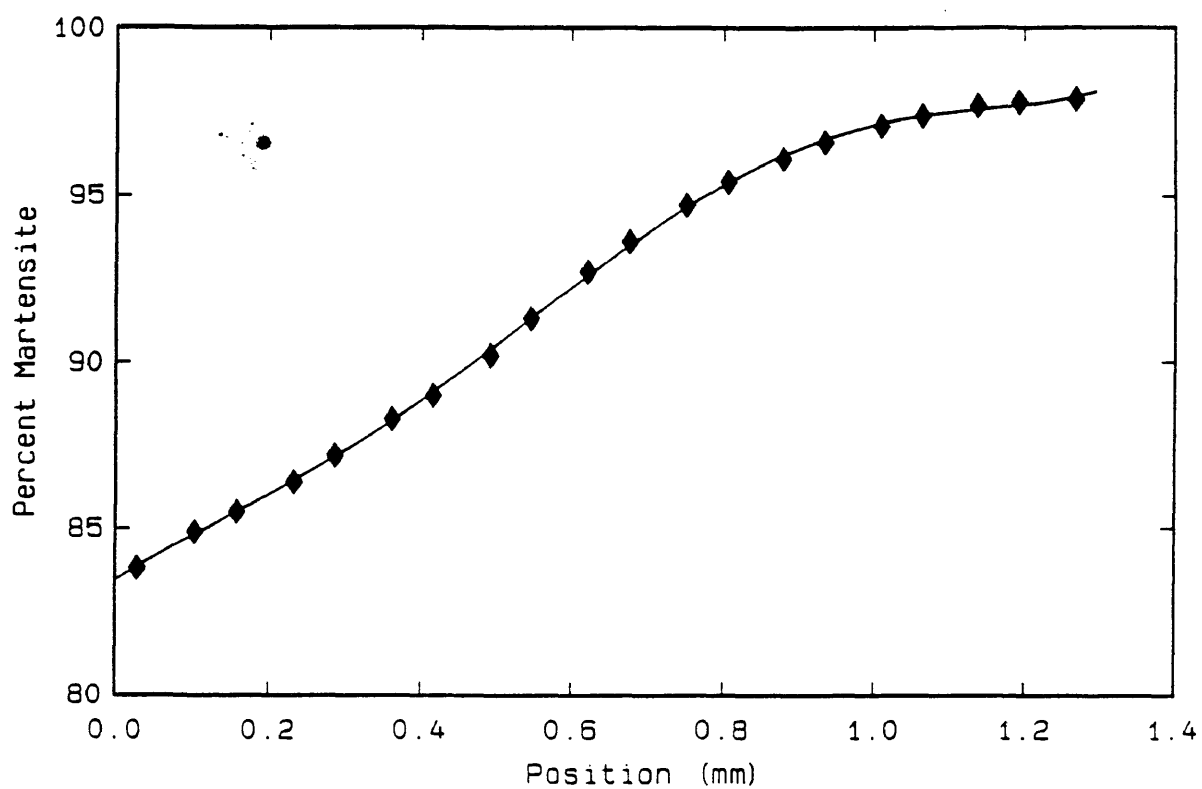


Figure 4.16 Calculated percentage of martensite as a function of thickness for the 1.30 millimeter Almen strip of SAE 4023 alloy steel at 25°C.

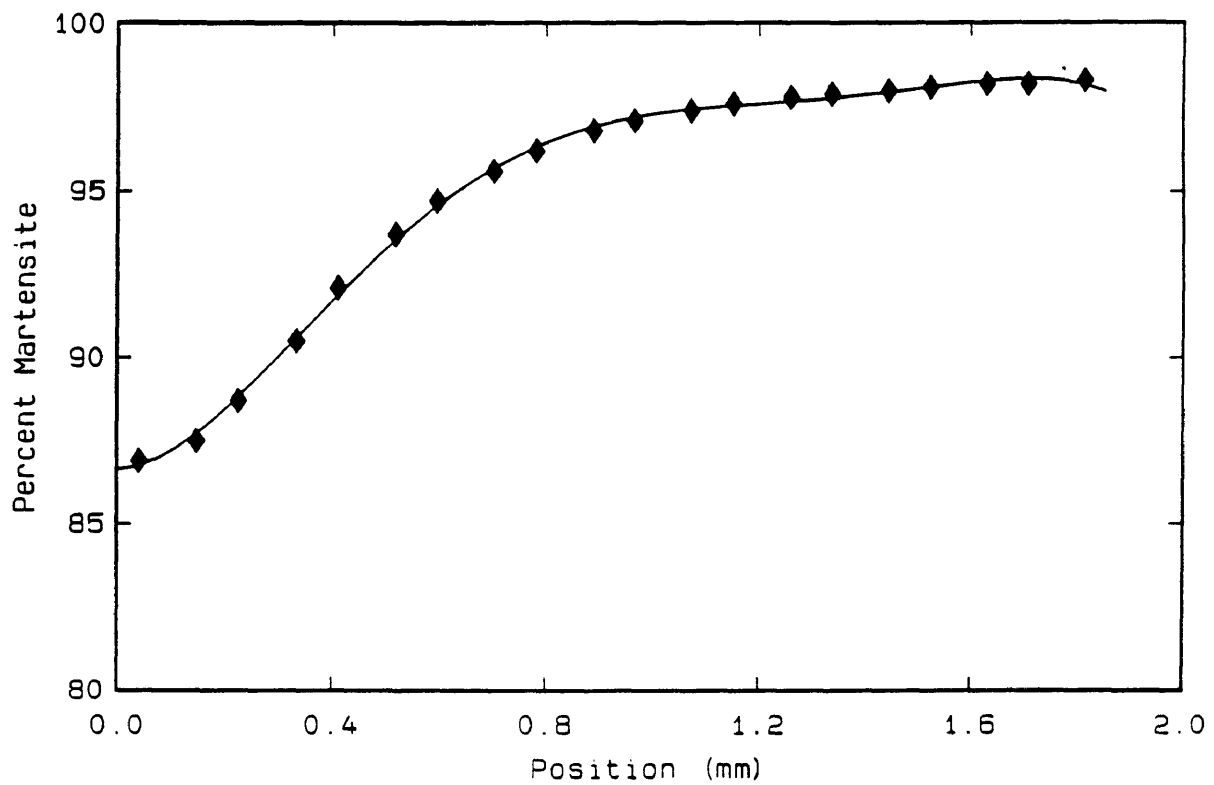


Figure 4.17 Calculated percentage of martensite as a function of thickness for the 1.85 millimeter Almen strip of SAE 4023 alloy steel at 25°C.

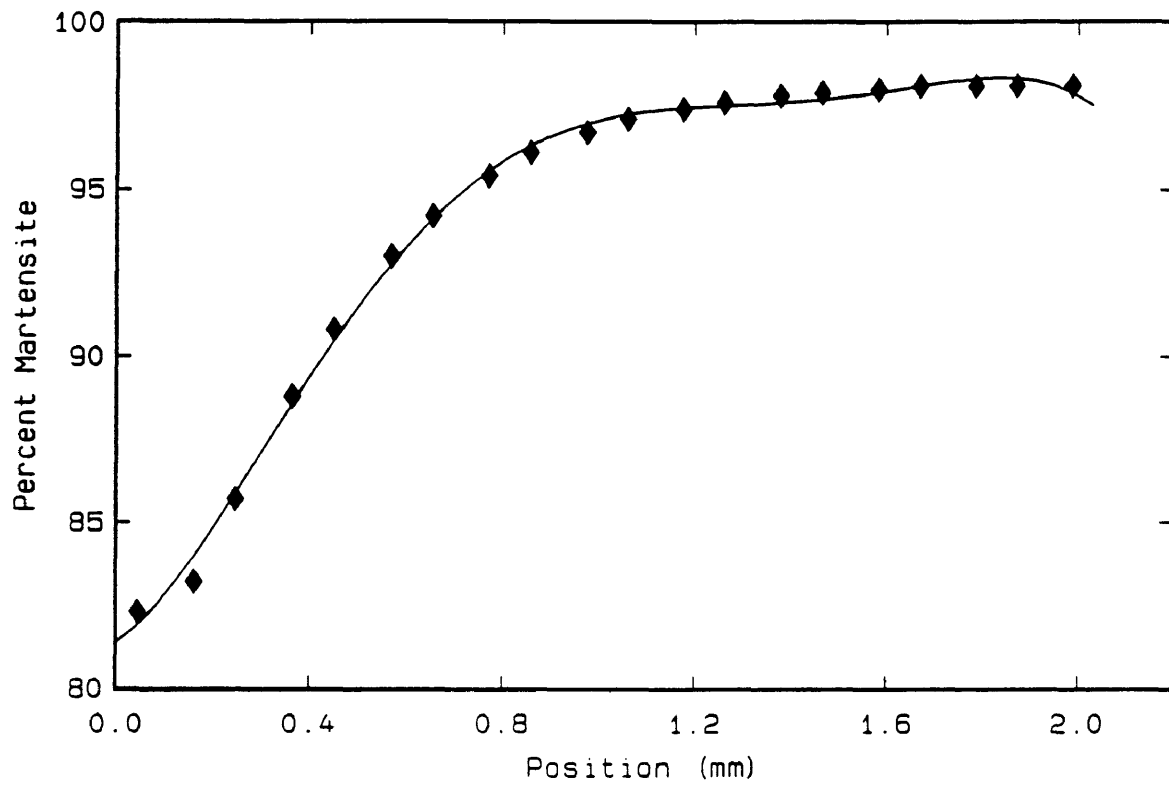


Figure 4.18 Calculated percentage of martensite as a function of thickness for the 2.03 millimeter Almen strip of SAE 4023 alloy steel at 25°C.

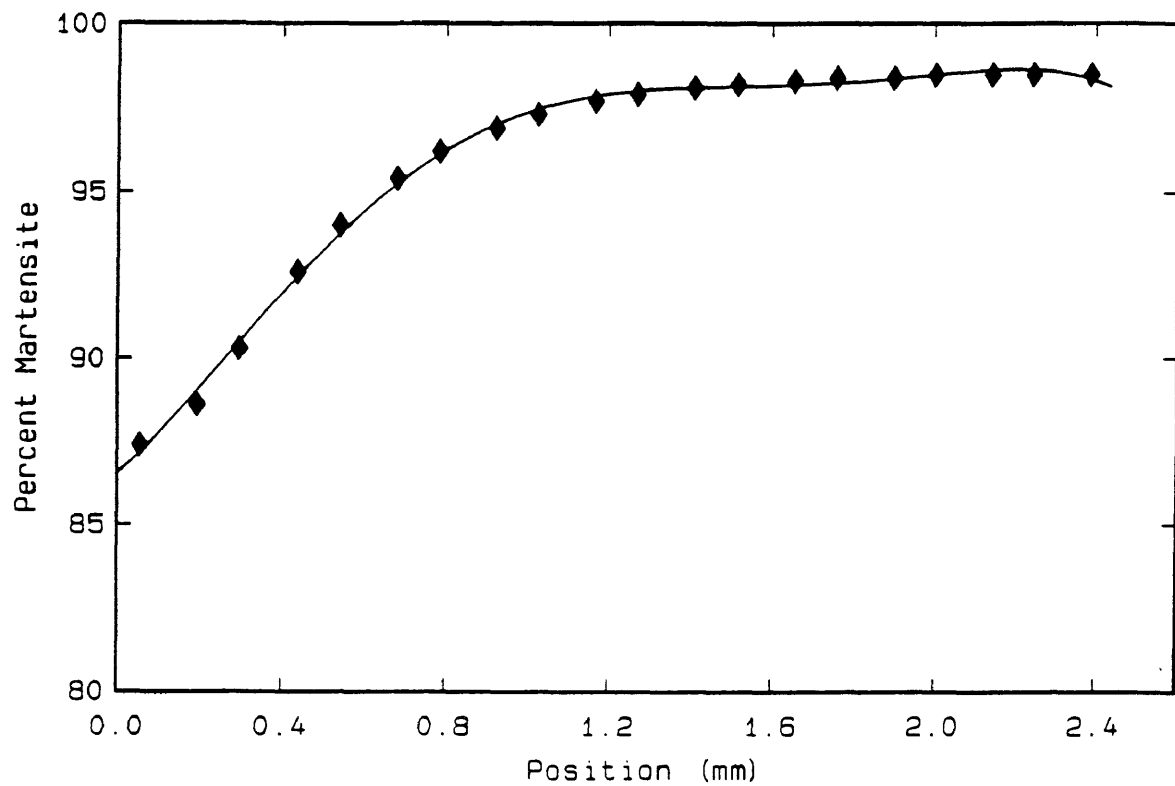


Figure 4.19 Calculated percentage of martensite as a function of thickness for the 2.44 millimeter Almen strip of SAE 4023 alloy steel at 25°C.

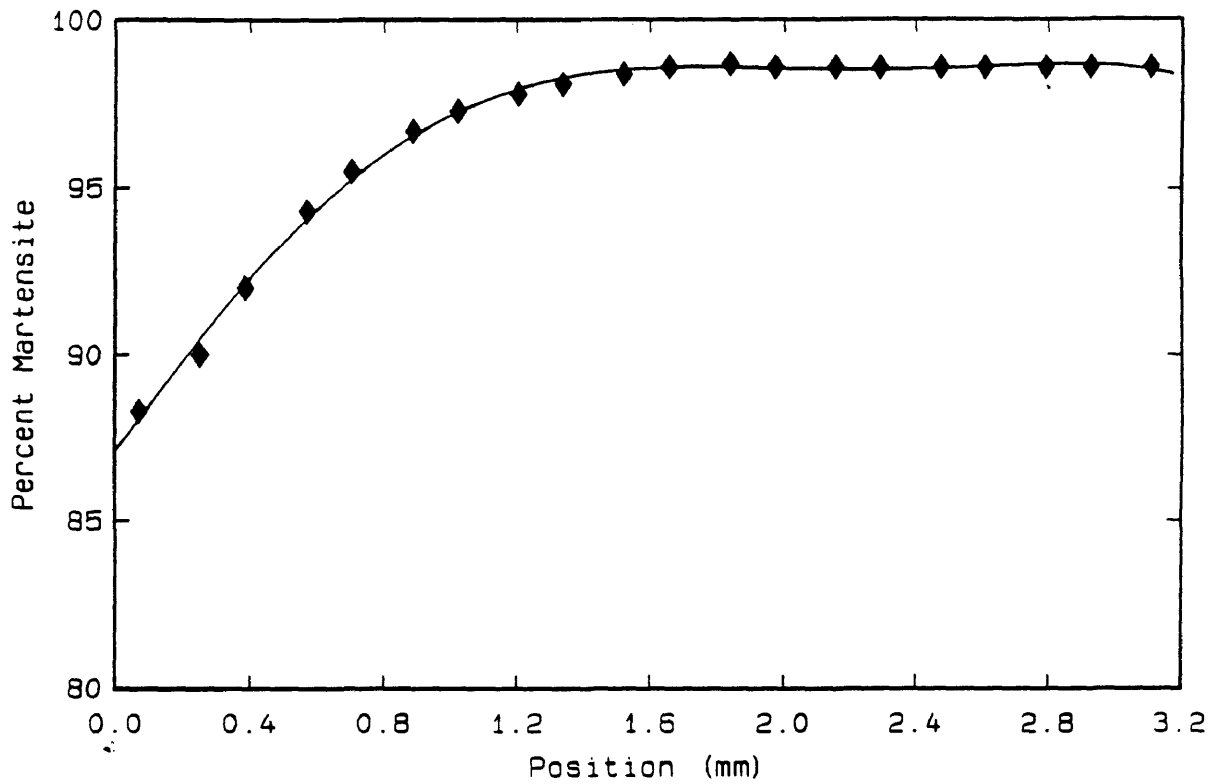


Figure 4.20 Calculated percentage of martensite as a function of thickness for the 3.18 millimeter Almen strip of SAE 4023 alloy steel at 25°C.

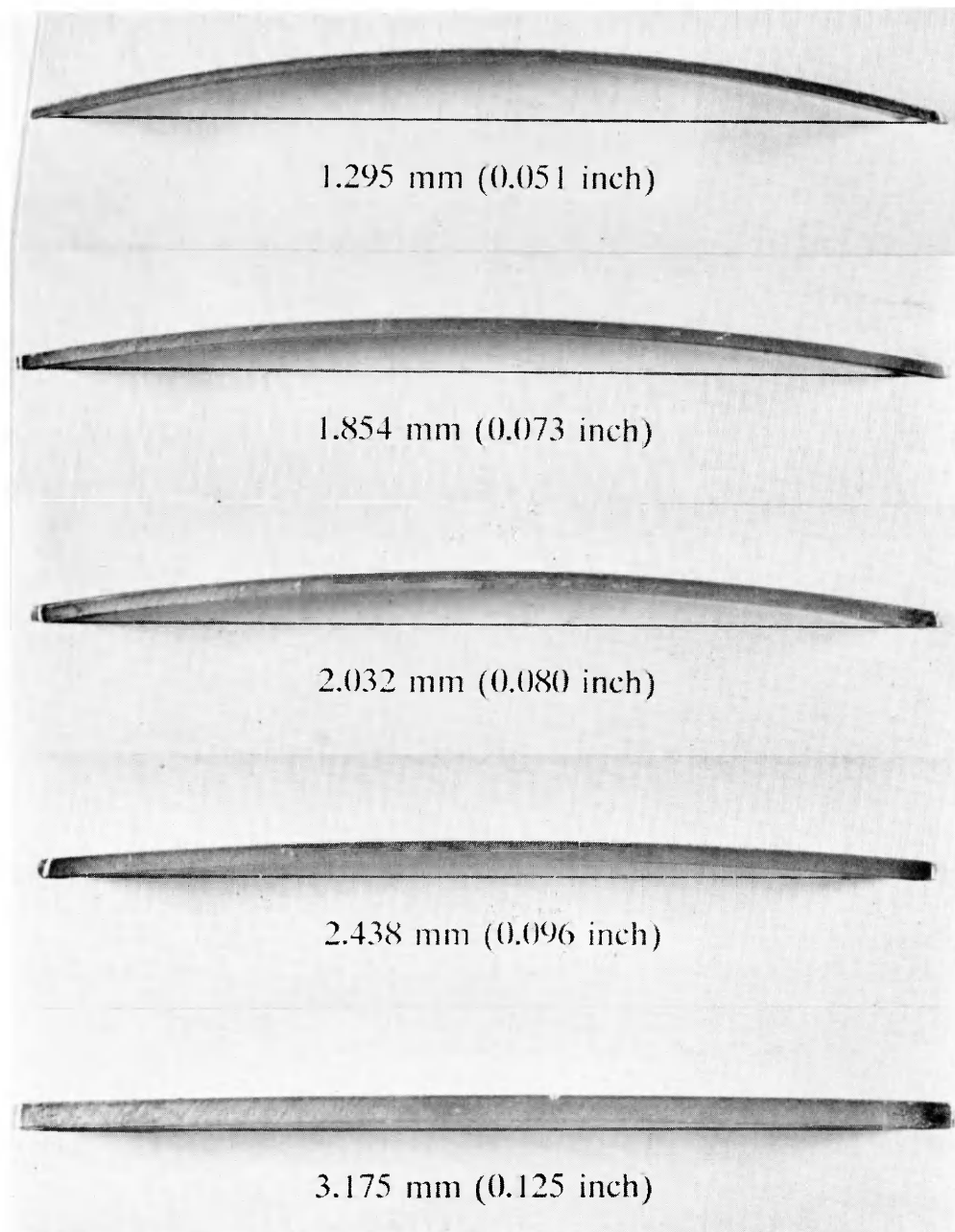


Figure 4.21 Deflected shape of the SAE 4023 Almen strips after being carburized and quenched. The various thicknesses are indicated. The carburized surface is convex.

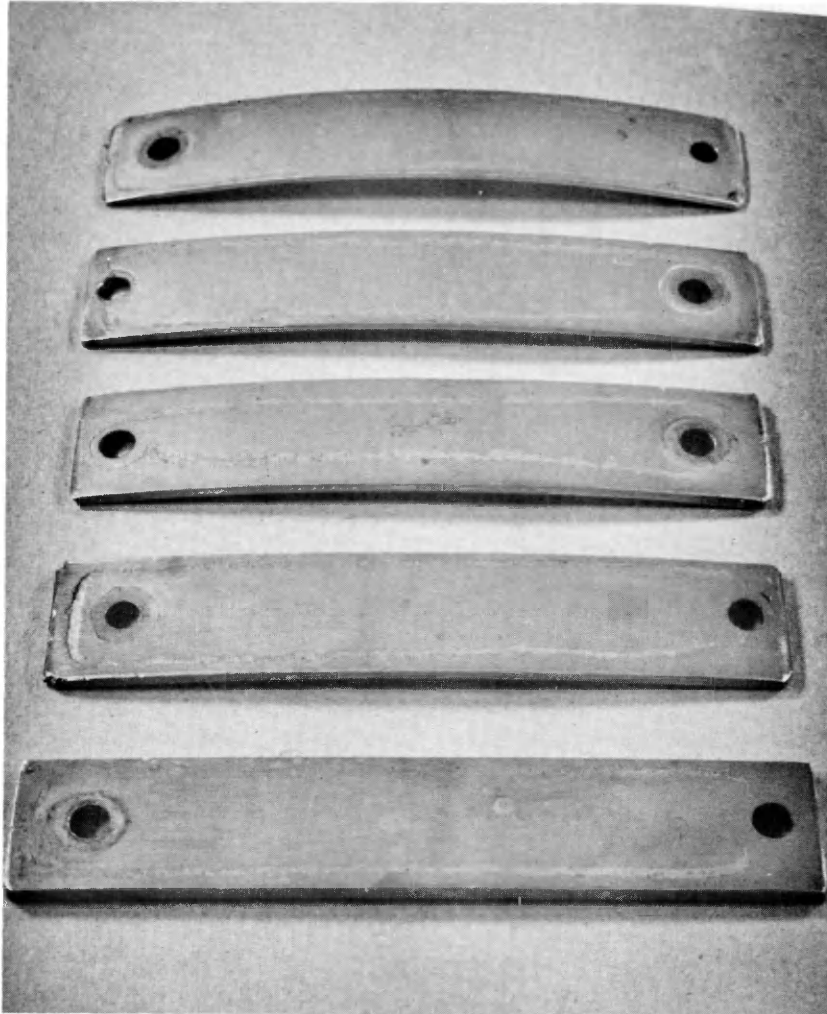


Figure 4.22 Deflected shape of the SAE 4023 Almen strips after being carburized and quenched. The carburized surface is convex.

Table 4.1
Experimental Arc Deflection Results at 25°C

| Sample | Alloy | Thickness, H * | Arc Deflection |
|--------------------------------------|----------|----------------|----------------|
| #1 | SAE 4023 | 1.30 mm | 7.54 mm |
| #2 | SAE 4023 | 1.30 mm | 7.52 mm |
| #3 | SAE 4620 | 1.30 mm | 7.19 mm |
| #4 | SAE 4620 | 1.30 mm | 0 mm ** |
| #5 | SAE 4023 | 1.85 mm | 5.03 mm |
| #6 | SAE 4023 | 1.85 mm | 5.36 mm |
| #7 | SAE 4620 | 1.85 mm | 5.18 mm |
| #8 | SAE 4620 | 1.85 mm | 0 mm ** |
| #9 | SAE 4023 | 2.03 mm | 0 mm ** |
| #10 | SAE 4023 | 2.03 mm | 4.24 mm |
| #11 | SAE 4620 | 2.03 mm | 4.25 mm |
| #12 | SAE 4620 | 2.03 mm | 4.50 mm |
| #13 | SAE 4023 | 2.44 mm | 2.39 mm |
| #14 | SAE 4023 | 2.44 mm | 2.39 mm |
| #15 | SAE 4620 | 2.44 mm | 2.99 mm |
| #16 | SAE 4620 | 2.44 mm | 2.92 mm |
| #17 | SAE 4023 | 3.18 mm | 1.02 mm |
| #18 | SAE 4023 | 3.18 mm | 1.02 mm |
| #19 | SAE 4620 | 3.18 mm | 1.12 mm |
| #20 | SAE 4620 | 3.18 mm | 1.14 mm |
| * ± 0.025 mm before plating | | | |
| ** control strip - plated both sides | | | |

From the results given in Table 4.1, the difference in deflection response due to alloying additions is negligible. Therefore, additional discussion will concentrate on the SAE 4023 alloy steel results only.

Figure 4.23 illustrates the calculated deflection history of the various thicknesses of SAE 4023 Almen strips. Table 4.2 indicates the final average arc deflections of the experimental Almen strips and the calculated arc deflection using CSMCARB.

Table 4.2
Average Experimental and Calculated Arc Deflection
Results at 25°C

| Thickness, H * | Average Arc Deflection (experimental) | Arc Deflection (CSMCARB) |
|---------------------------------|---------------------------------------|--------------------------|
| 1.30 mm | 7.42 mm | -1.22 mm |
| 1.85 mm | 5.19 mm | 1.09 mm |
| 2.03 mm | 4.39 mm | 1.77 mm |
| 2.44 mm | 2.67 mm | 1.24 mm |
| 3.18 mm | 1.07 mm | 1.15 mm |
| * \pm 0.025 mm before plating | | |

The maximum arc deflection for each alloy and thickness of Almen strips were measured using cord lengths of 31.75, 50.8, 76.2, and 101.6 millimeters. The corresponding radius of curvature for each of the samples was then calculated, assuming a circumferential deflected shape. This method is presented in Appendix E. The calculated quenched shape using CSMCARB yielded a radius of curvature in a similar manner.

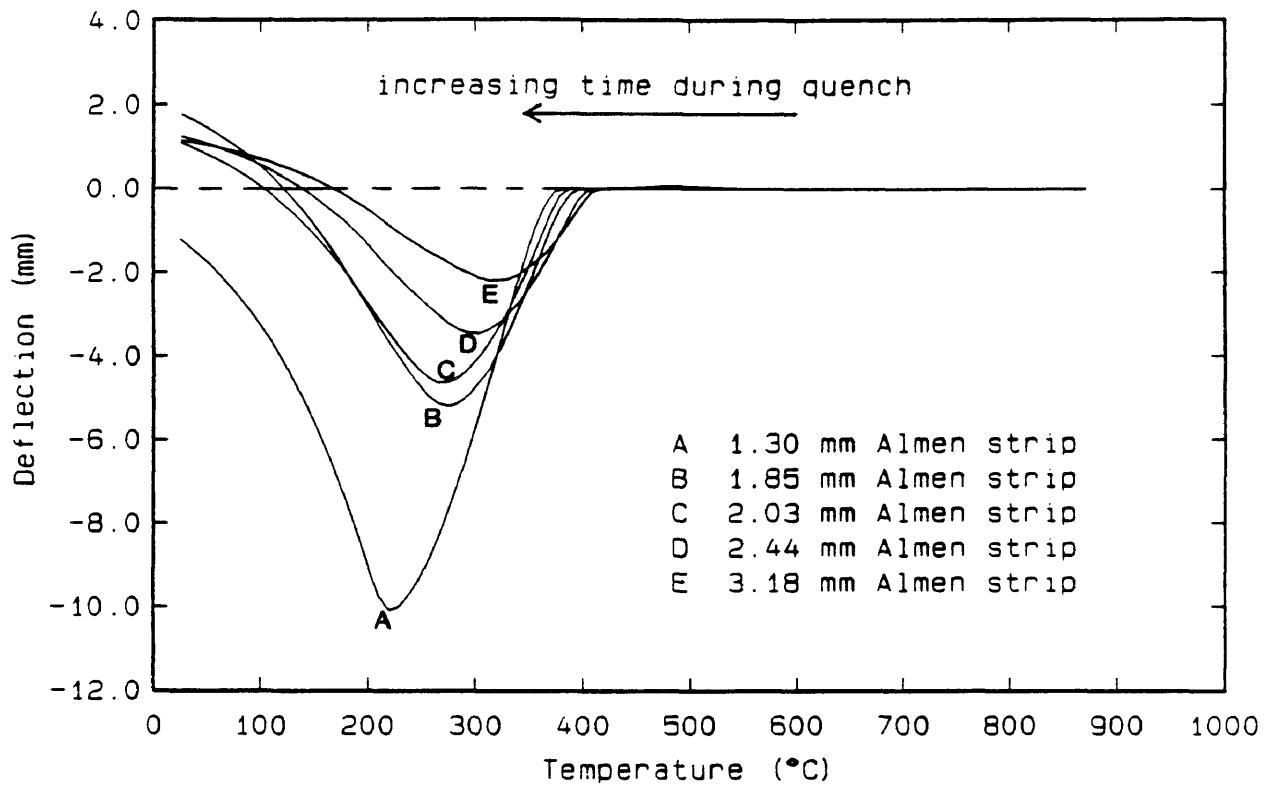


Figure 4.23 Deflection history for the various indicated thicknesses of SAE 4023 Almen strips. The analysis begins at 871°C and continues to 25°C.

Figure 4.24 illustrates the average radius of curvature for the five thicknesses of experimental Almen strips and the calculated radius of curvature using CSMCARB for the SAE 4023 alloy. No substantial differences in deflection were observed between the SAE 4023 and SAE 4620 alloy steel samples.

4.3 Experimental and Numerical Residual Stress Profiles

CSMCARB was used to calculate the residual stress profiles through the various thicknesses of Almen strips. All stress distributions presented are for the calculated stress with a resultant acting in the X-coordinate direction, τ_{xx} (parallel to the model length). Note that the axial stress, τ_{xx} , is not necessarily zero at the material surface. The stress distribution in the Y-coordinate direction (the Almen thickness direction), τ_{yy} , and the shear stress, τ_{xy} , were negligible compared to the axial stress, τ_{xx} . Figures 4.25-4.29 illustrate the residual stress profiles through the model thickness for the five thicknesses of SAE 4023 Almen strip models at 25°C.

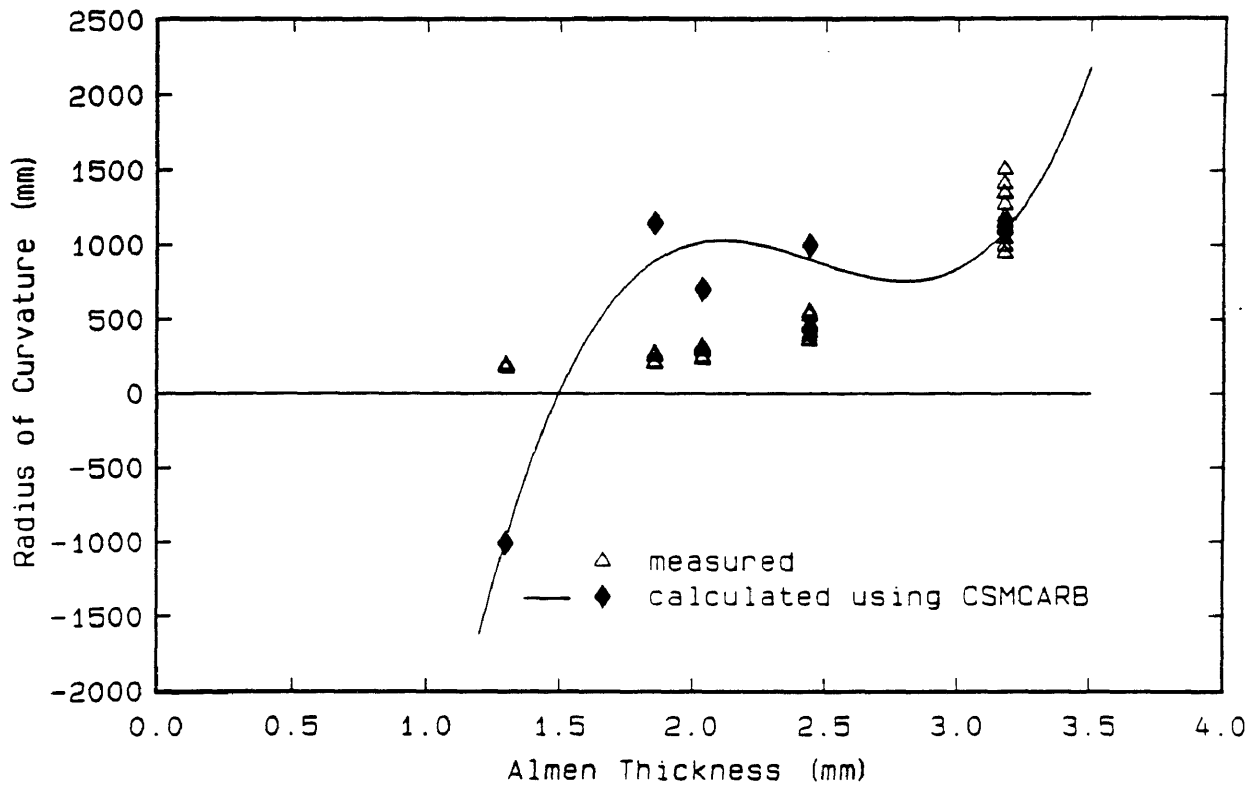


Figure 4.24 Average radius of curvature at 25°C for the five thicknesses of experimental Almen strips and the calculated radius of curvature using CSMCARB for the SAE 4023 alloy.

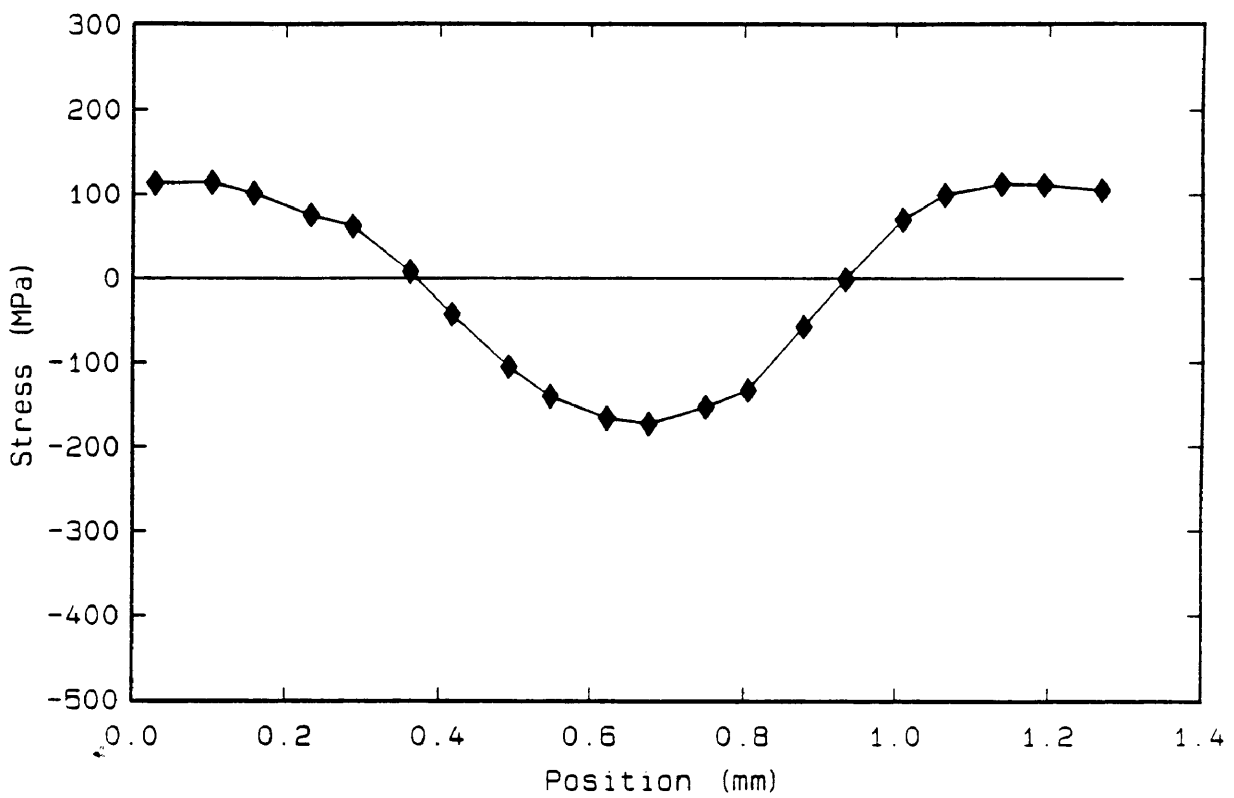


Figure 4.25 Calculated residual stress profile through the model thickness for the 1.30 millimeter SAE 4023 Almen strip model at 25°C.

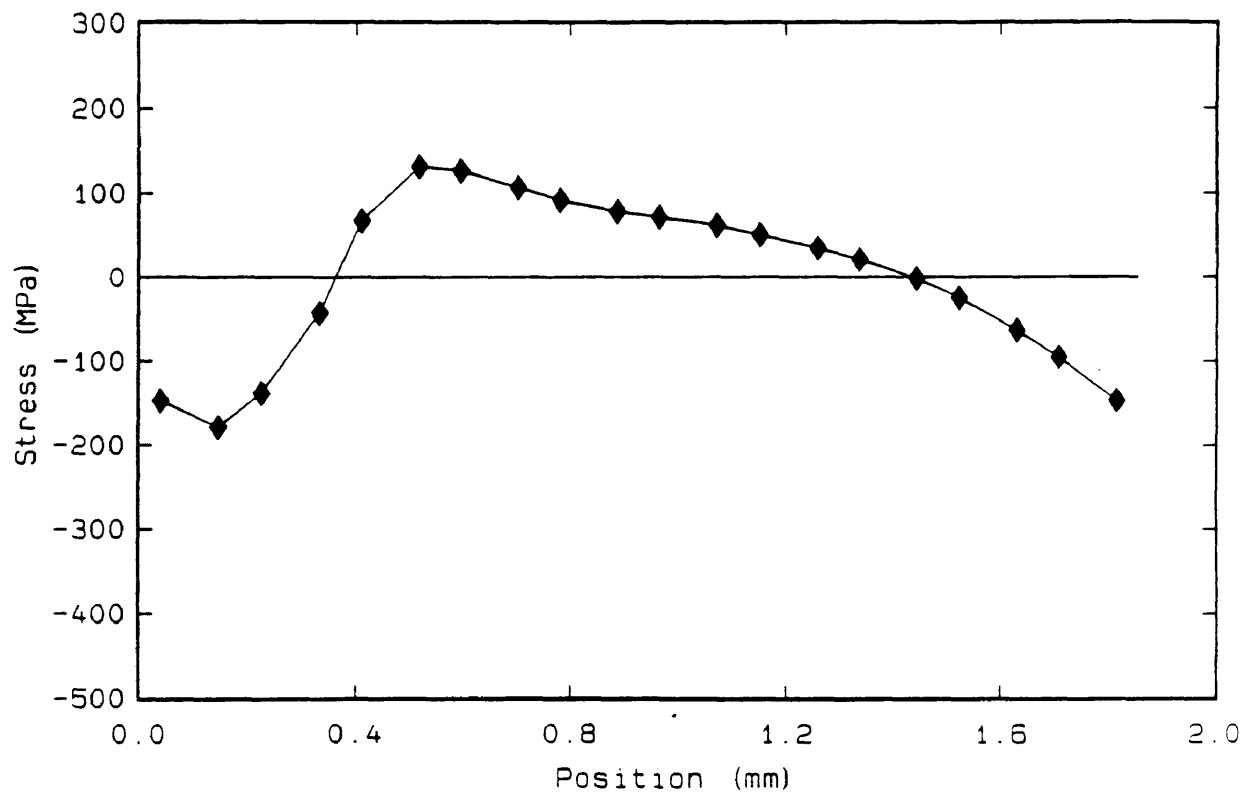


Figure 4.26 Calculated residual stress profile through the model thickness for the 1.85 millimeter SAE 4023 Almen strip model at 25°C.

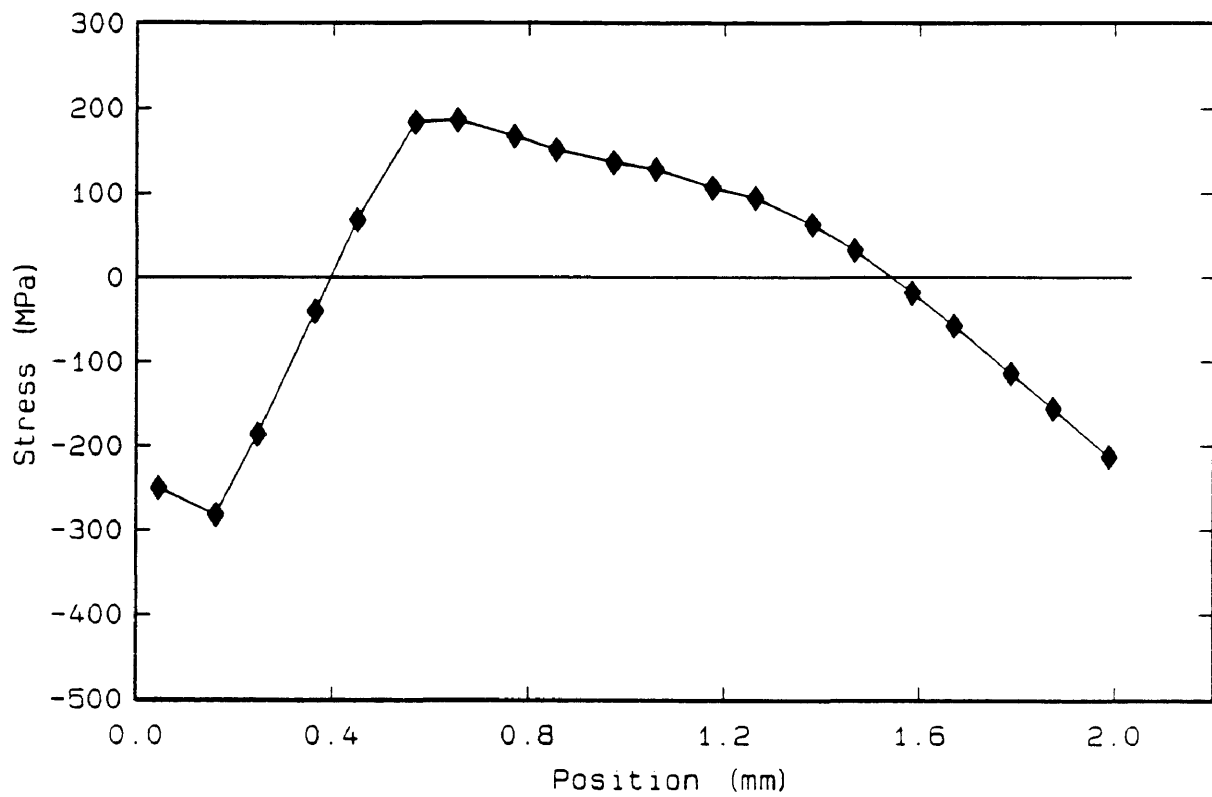


Figure 4.27 Calculated residual stress profile through the model thickness for the 2.03 millimeter SAE 4023 Almen strip model at 25°C.

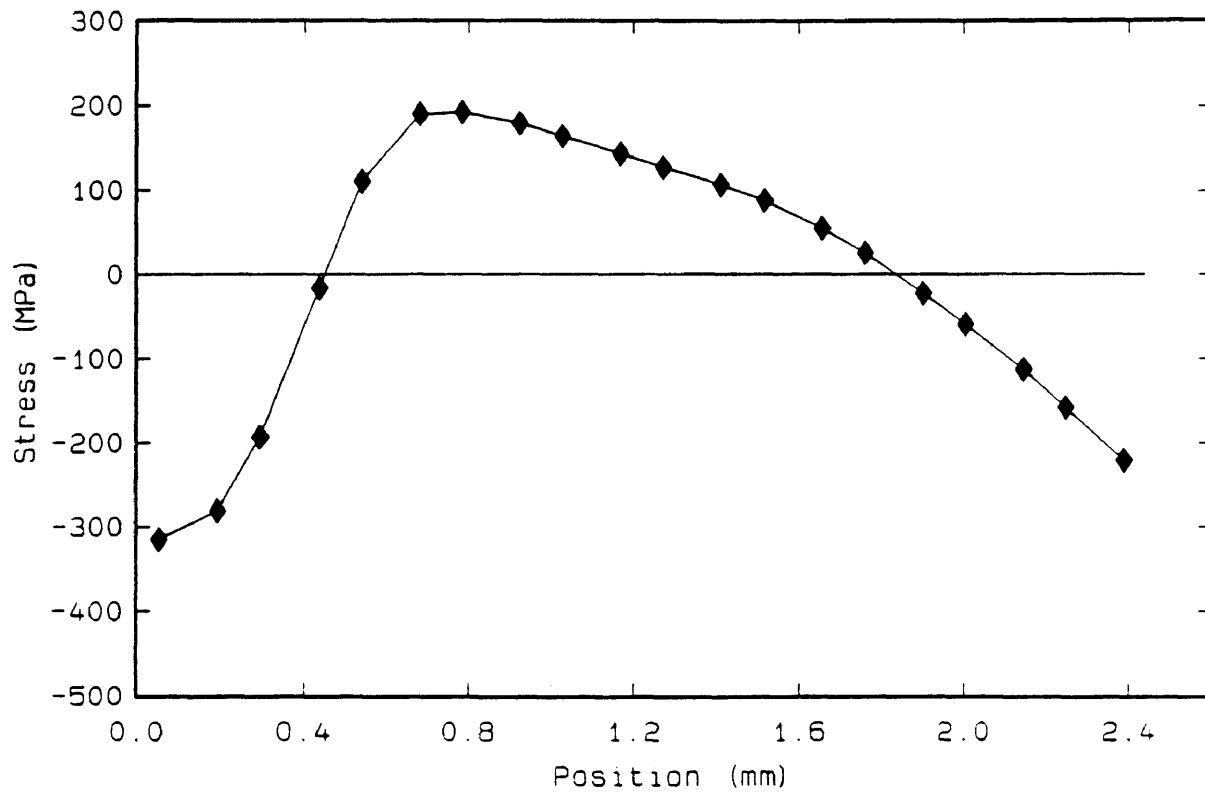


Figure 4.28 Calculated residual stress profile through the model thickness for the 2.44 millimeter SAE 4023 Almen strip model at 25°C.

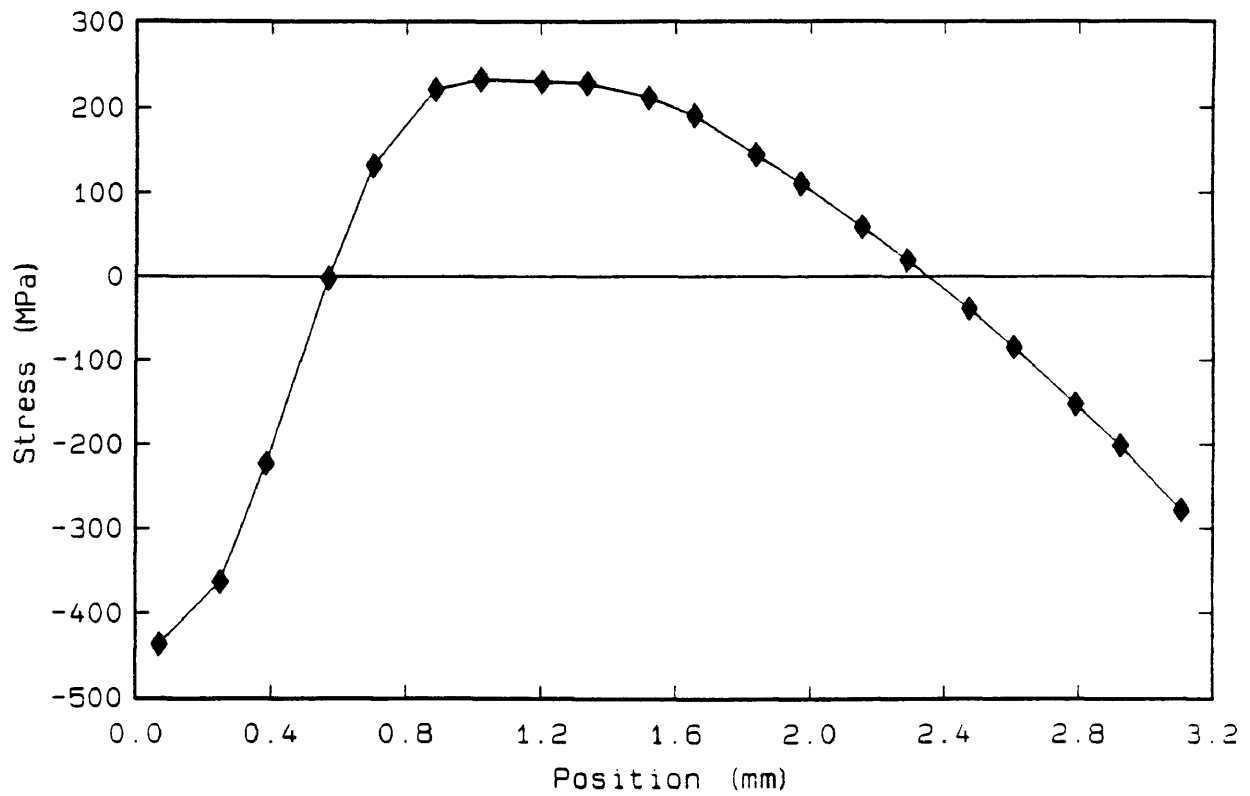


Figure 4.29 Calculated residual stress profile through the model thickness for the 3.18 millimeter SAE 4023 Almen strip model at 25°C.

Residual stress measurements were performed by the Eaton Corporation using SAE 4023 2.44 millimeter and SAE 4620 3.18 millimeter Almen strips. These data were then compared to the calculated stress profile using CSMCARB. Figures 4.30 and 4.31 illustrate the calculated residual stress profiles and experimental x-ray diffraction measurements for the SAE 4023 2.44 millimeter and SAE 4620 3.18 millimeter Almen strips, respectively. Agreement between the calculated residual stress profiles and experimentally measured results was not achieved. Further discussion is given in section 6.0.

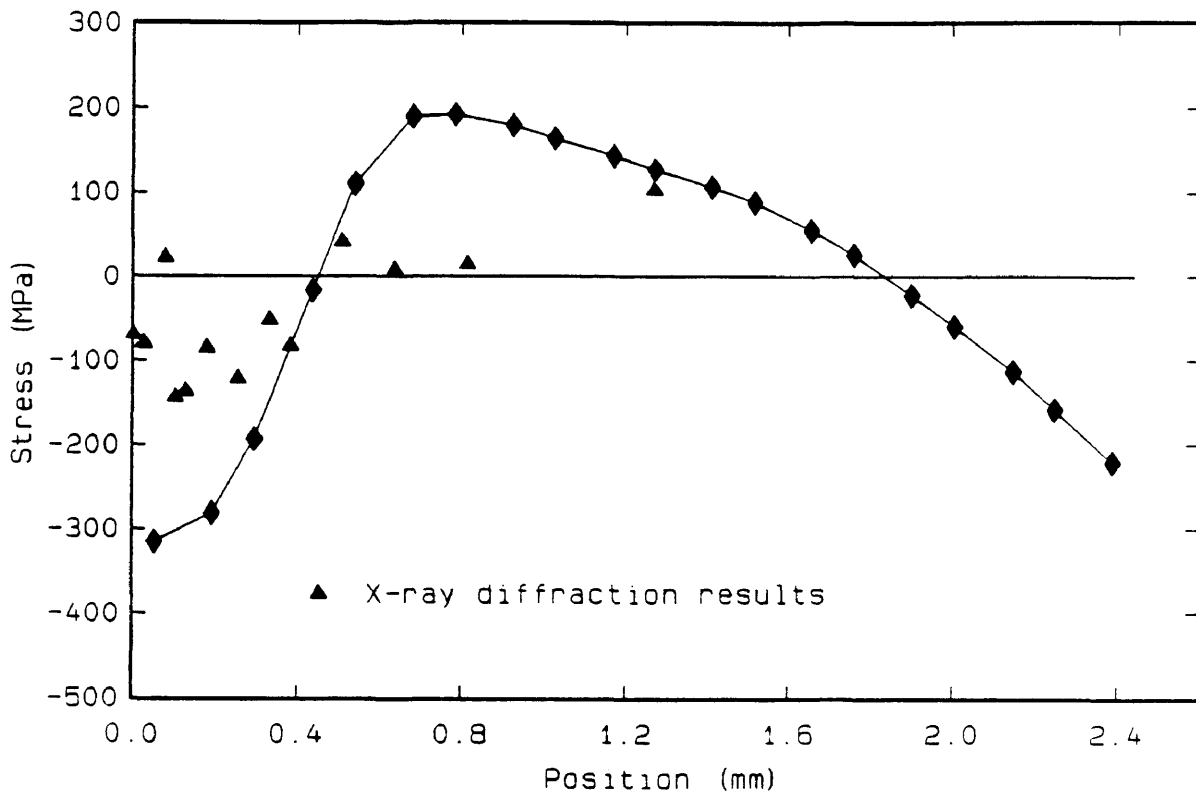


Figure 4.30 Calculated residual stress profile through the model thickness and experimental x-ray diffraction measurements for the SAE 4023 2.44 millimeter Almen strip.

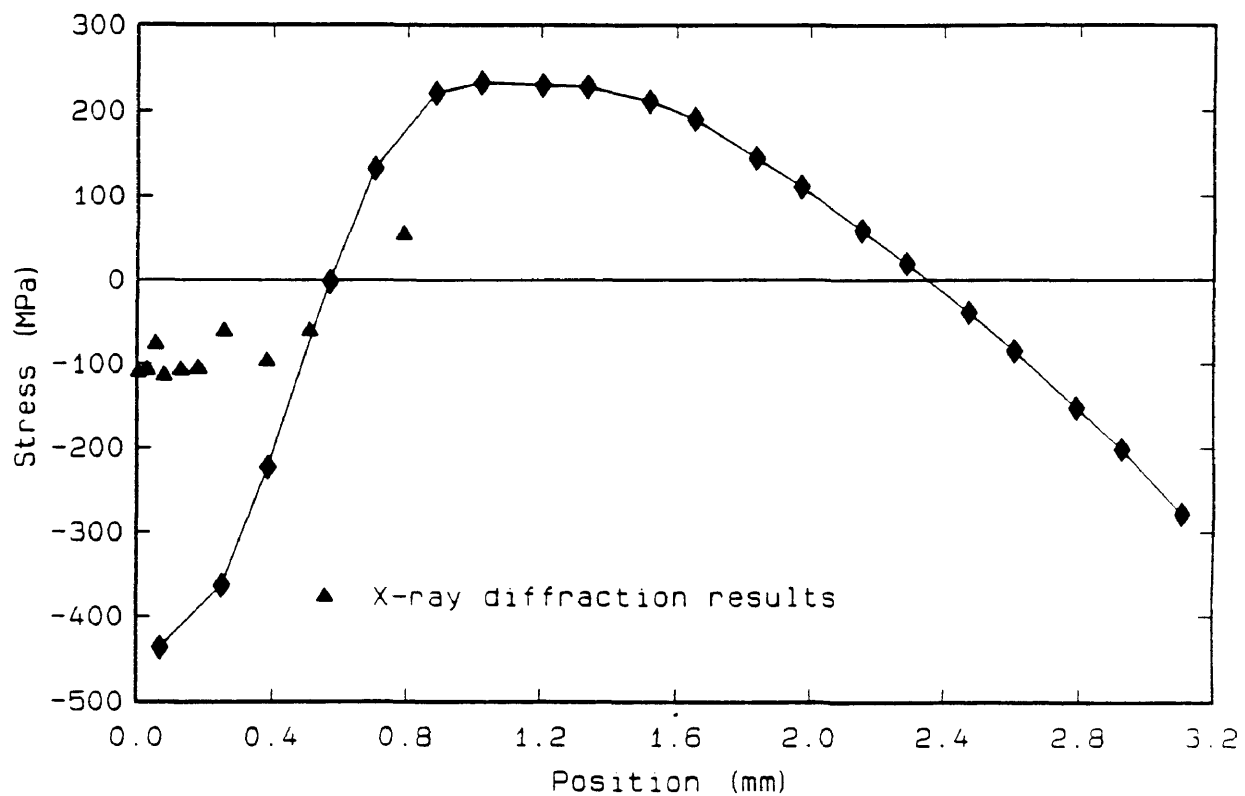


Figure 4.31 Calculated residual stress profile through the model thickness and experimental x-ray diffraction measurements for the SAE 4023 2.44 millimeter Almen strip.

5.0 INPUT DATA SENSITIVITY STUDY USING CSMCARB

A sensitivity study was performed using CSMCARB to determine which input data most influence the resulting deflection and residual stress profile in the Almen strip model. The martensite start temperature, elastic modulus and yield strength were varied for the quench analysis of the 2.03 millimeter SAE 4023 Almen strip model. Each variable was independently increased by 20% and decreased by 20% to determine the sensitivity of the particular variable to deflection and residual stress results.

5.1 Martensitic Start Temperature Sensitivity

The martensite start temperature was varied independently of all other input data by multiplying the calculated M_s temperature by 0.8 and 1.2. Hildenwall observed that the calculated M_s temperature varied by as much as 20% from the experimentally determined M_s temperature in carburized steel (2). Figures 5.1 and 5.2 illustrate the deflection histories and residual stress distributions at 25°C, respectively, for the 2.03 millimeter Almen strip model with a 20% increase and 20% decrease of the M_s temperature. Table 5.1 lists the calculated arc deflections at 25°C and percent change in arc deflection.

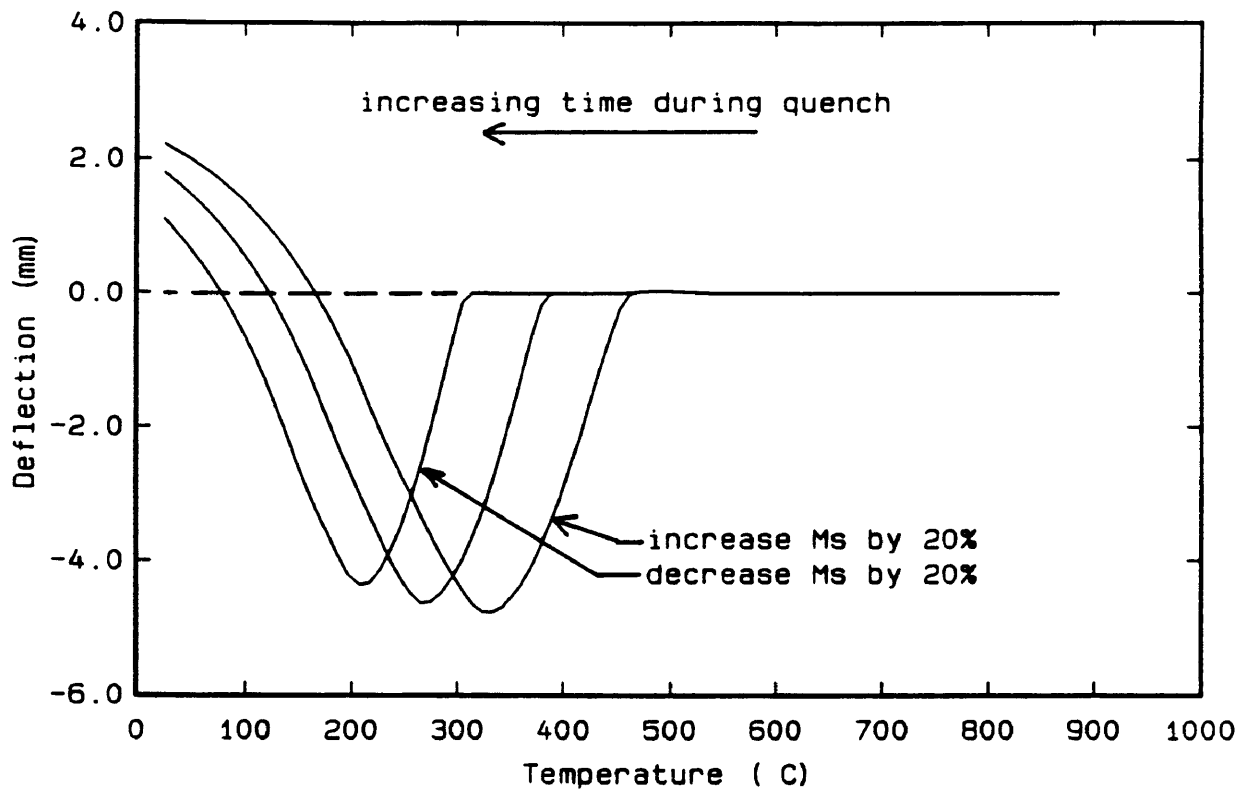


Figure 5.1 Deflection history for the 2.03 millimeter SAE 4023 Almen strip models with a 20% increase and 20% decrease of the M_s temperature. The analysis begins at 871°C and continues to 25°C .

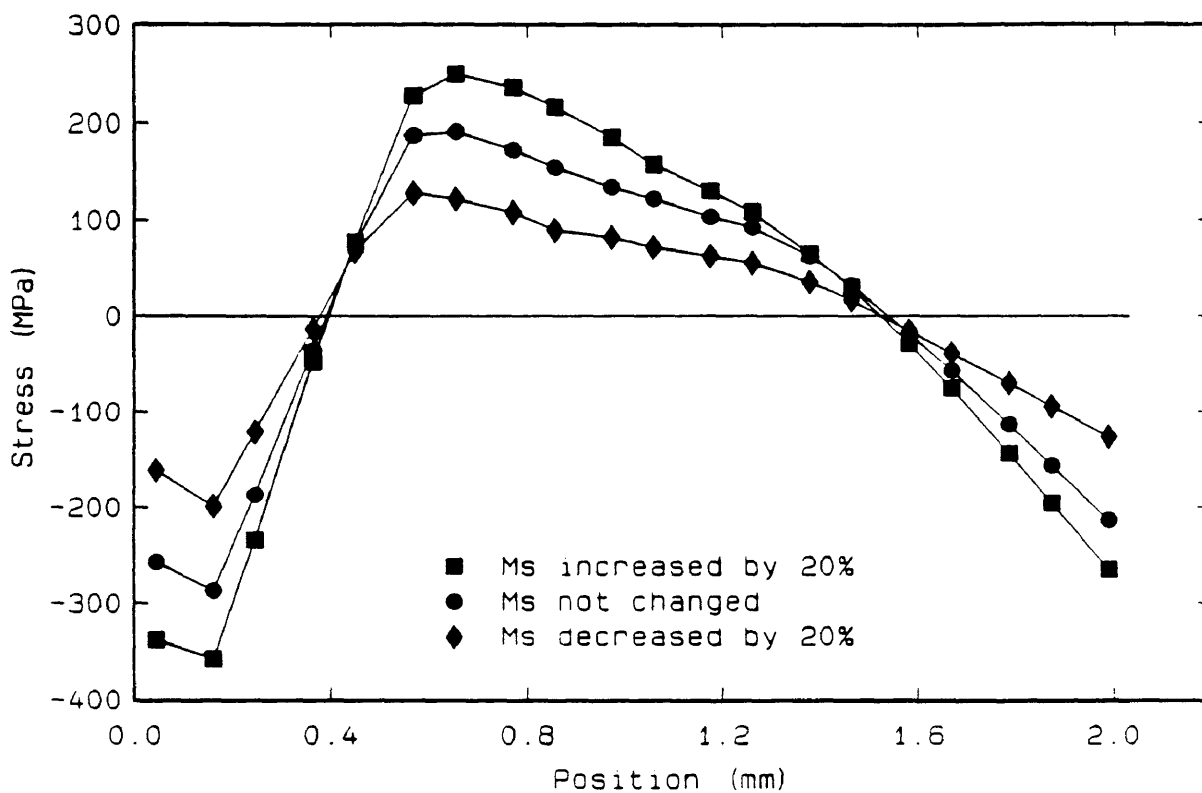


Figure 5.2 Residual stress distributions at 25°C for 2.03 millimeter SAE 4023 Almen strip models with a 20% increase and 20% decrease of the M_s temperature.

Table 5.1
 M_s Sensitivity Analysis - Arc Deflection

| Sensitivity Analysis | Arc Deflection | Percent Change in Deflection |
|--|----------------|------------------------------|
| Increase the M_s temperature by 20% | 2.22 mm | +24.0% |
| no adjustment of the M_s temperature | 1.79 mm | - |
| Decrease the M_s temperature by 20% | 1.10 mm | -38.5% |

Table 5.2 lists the maximum calculated compressive residual stress at 25°C and percent change in maximum compressive residual stress.

Table 5.2
 M_s Sensitivity Analysis - Residual Stress

| Sensitivity Analysis | Maximum Calculated Compressive Residual Stress | Percent Change in Residual Stress |
|--|--|-----------------------------------|
| Increase the M_s temperature by 20% | -358 MPa | +24.7% |
| no adjustment of the M_s temperature | -287 MPa | - |
| Decrease the M_s temperature by 20% | -199 MPa | -30.7% |

From these results it is concluded that the M_s temperature has a significant effect on both the deflection and residual stress results for the 2.03 millimeter SAE 4023 Almen strip model.

5.2 Elastic Modulus Sensitivity

The elastic modulus, E , was varied independently of all other input data. It was reported by Larson (29) that the elastic modulus data experimentally measured by Burnett (1) and subsequently used by Hildenwall, Sjöström and Dougherty (2,3,4) could be substantially in error. Figures 5.3 and 5.4 illustrate the deflection histories and residual stress distributions at 25°C, respectively, for the 2.03 millimeter Almen strip model with a 20% increase and 20% decrease of the elastic modulus, E . Table 5.3 lists the calculated arc deflections at 25°C and percent change in arc deflection.

Table 5.3
Elastic Modulus Sensitivity Analysis - Arc Deflection

| Sensitivity Analysis | Arc Deflection | Percent Change in Deflection |
|--|----------------|------------------------------|
| Increase the elastic modulus, E , by 20% | 2.21 mm | +23.4% |
| no adjustment of the elastic modulus, E | 1.79 mm | - |
| Decrease the elastic modulus, E , by 20% | 1.26 mm | -29.6% |

Table 5.4 lists the maximum calculated compressive residual stress at 25°C and percent change in maximum compressive residual stress.

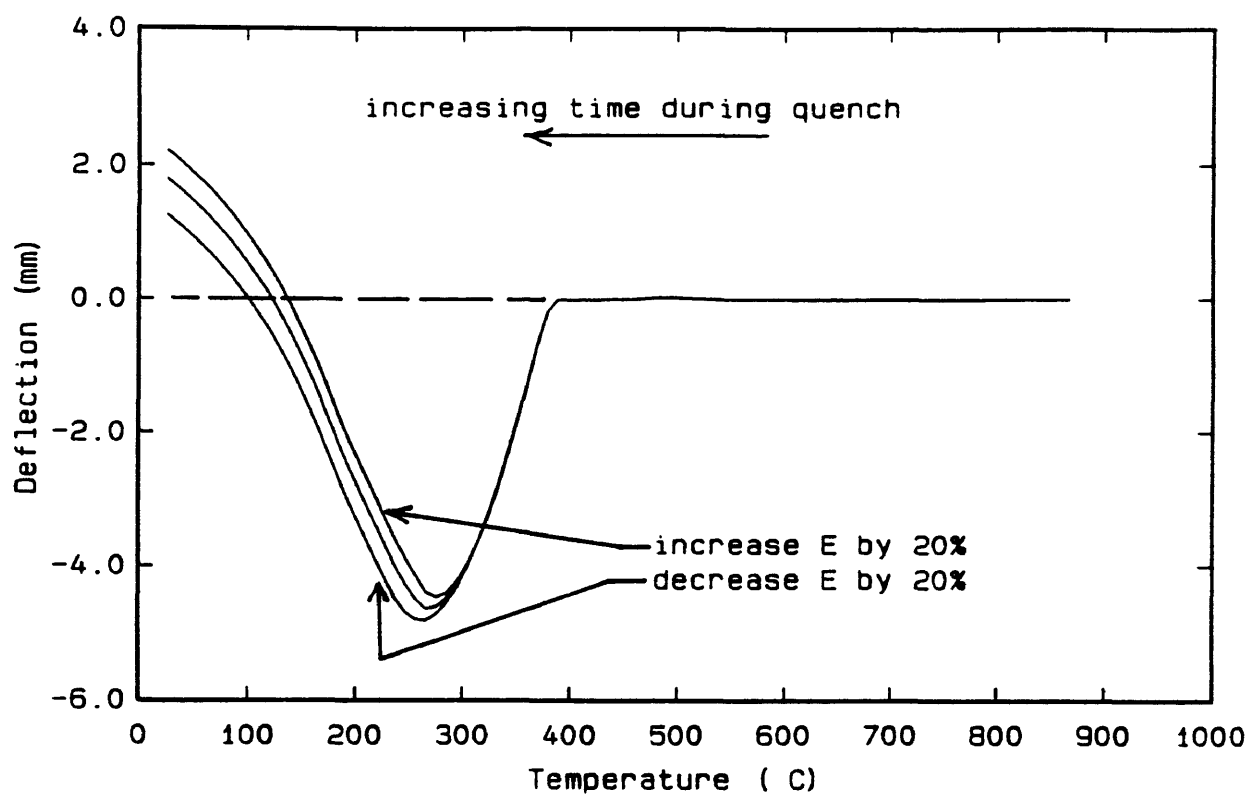


Figure 5.3 Deflection history for the 2.03 millimeter SAE 4023 Almen strip models with a 20% increase and 20% decrease of the elastic modulus, E. The analysis begins at 871°C and continues to 25°C.

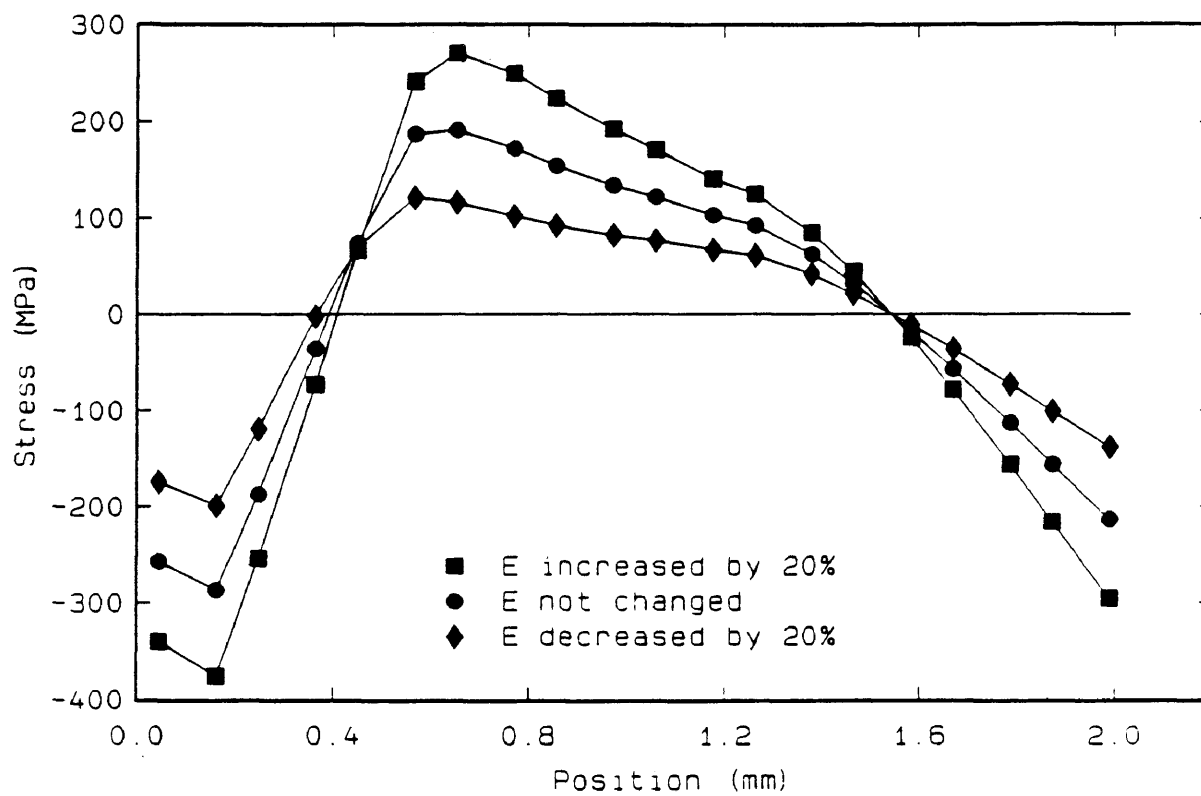


Figure 5.4 Residual stress distributions at 25°C for 2.03 millimeter SAE 4023 Almen strip models with a 20% increase and 20% decrease of the elastic modulus, E.

Table 5.4
Elastic Modulus Sensitivity Analysis - Residual Stress

| Sensitivity Analysis | Maximum Calculated Compressive Residual Stress | Percent Change in Residual Stress |
|--|--|-----------------------------------|
| Increase the elastic modulus, E , by 20% | -376 MPa | +31.0% |
| no adjustment of the elastic modulus | -287 MPa | - |
| Decrease the elastic modulus, E , by 20% | -199 MPa | -30.7% |

From these results it is concluded that the elastic modulus, E , has a significant effect on the deflection and residual stress results for the 2.03 millimeter SAE 4023 Almen strip model.

5.3 Yield Strength Sensitivity

The yield strength, S_y , was varied independently of all other input data. Figures 5.5 and 5.6 illustrate the deflection histories and residual stress distributions at 25°C, respectively, for the 2.03 millimeter Almen strip model with a 20% increase and 20% decrease of the yield strength, S_y . Table 5.5 lists the calculated arc deflections at 25°C and percent change in arc deflection.

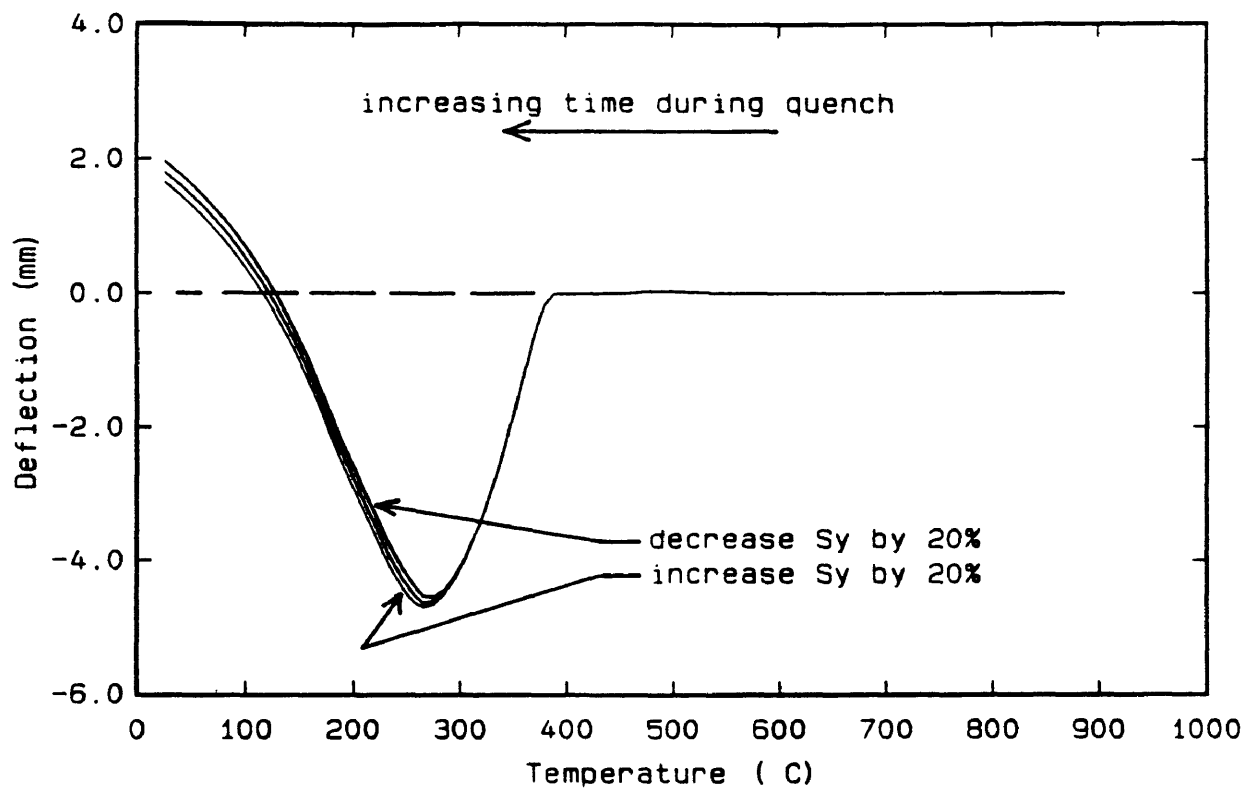


Figure 5.5 Deflection history for the 2.03 millimeter SAE 4023 Almen strip models with a 20% increase and 20% decrease of the yield strength, S_y . The analysis begins at 871°C and continues to 25°C.

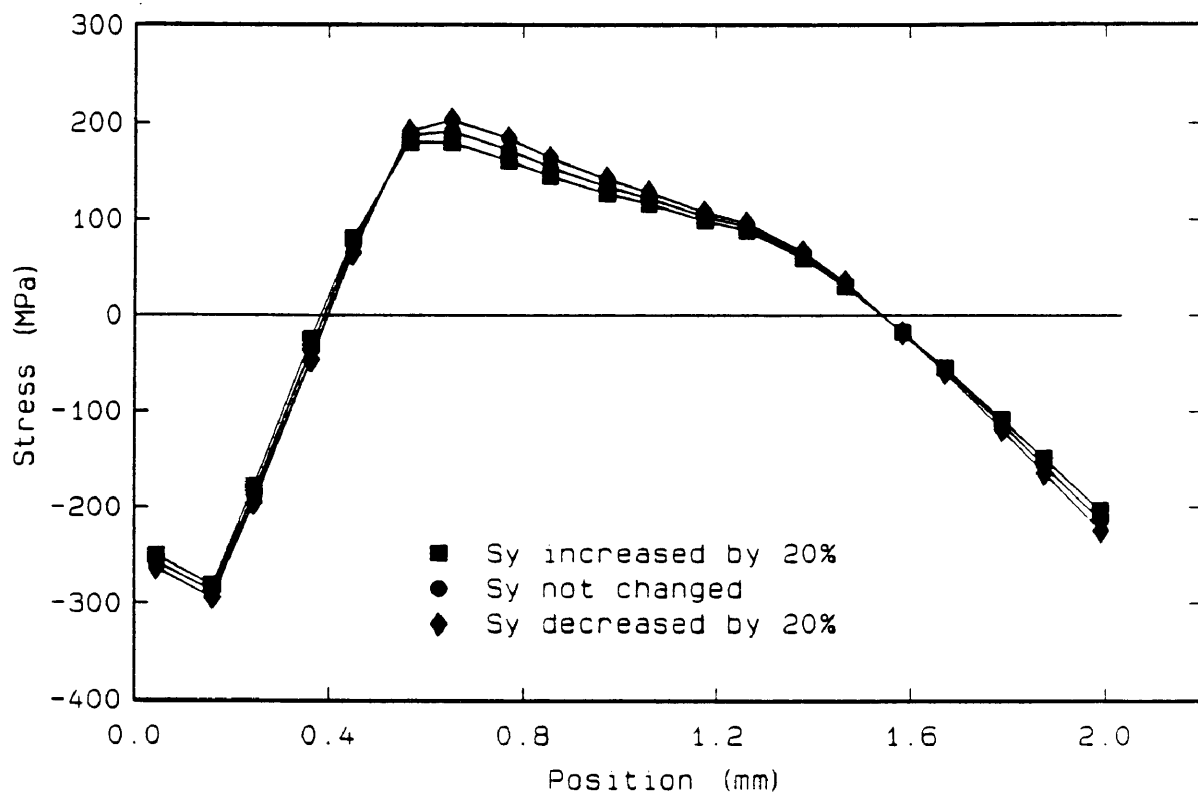


Figure 5.6 Residual stress distributions at 25°C for 2.03 millimeter SAE 4023 Almen strip models with a 20% increase and 20% decrease of the yield strength, S_y .

Table 5.5
Yield Strength Sensitivity Analysis - Arc Deflection

| Sensitivity Analysis | Arc Deflection | Percent Change in Deflection |
|---|----------------|------------------------------|
| Increase the yield strength, S_y , by 20% | 1.64 mm | -8.4% |
| no adjustment of the yield strength, S_y | 1.79 mm | - |
| Decrease the yield strength, S_y , by 20% | 1.95 mm | +8.9% |

Table 5.6 lists the maximum calculated compressive residual stress at 25°C and percent change in maximum compressive residual stress.

Table 5.6
Yield Strength Sensitivity Analysis - Residual Stress

| Sensitivity Analysis | Maximum Calculated Compressive Residual Stress | Percent Change in Residual Stress |
|---|--|-----------------------------------|
| Increase the yield strength, S_y , by 20% | -281 MPa | -2.1% |
| no adjustment of the yield strength, S_y | -287 MPa | - |
| Decrease the yield strength, S_y , by 20% | -294 MPa | +2.4% |

From these results it is concluded that the yield strength, S_y , has a moderate effect on the deflection results but not a significant effect on the residual stress results for the 2.03 millimeter SAE 4023 Almen strip model.

6.0 DISCUSSION

A discussion of the experimental and numerical results presented in section 4.0 is given in the following sections.

6.1 Calculated Deflection History Explanation

The following explanation describes the physical response of the Almen strip model during the quench analysis. Figure 6.1 depicts the finite element model used in this study. Figure 6.2 shows the deflection history for the 2.03 millimeter SAE 4023 Almen strip and four indicated temperatures, A, B, C, and D. Figure 6.3 schematically illustrates the relative strain distributions through the model thickness at temperatures A, B, C, and D. This description ignores the different cooling rates associated with quenching in oil and air cooling.

At the beginning of the quench analysis (temperature A in Figures 6.2 and 6.3), the model contracts symmetrically and elastically about its centerline due to induced thermal strain from a symmetric temperature profile. A symmetric residual stress profile also develops due to differential cooling between the model surface and centerline. The model transitions to plastic behavior after a 5°C to 15°C temperature decrease due the residual stress state exceeding the hot yield strength of the material (the elastic-plastic

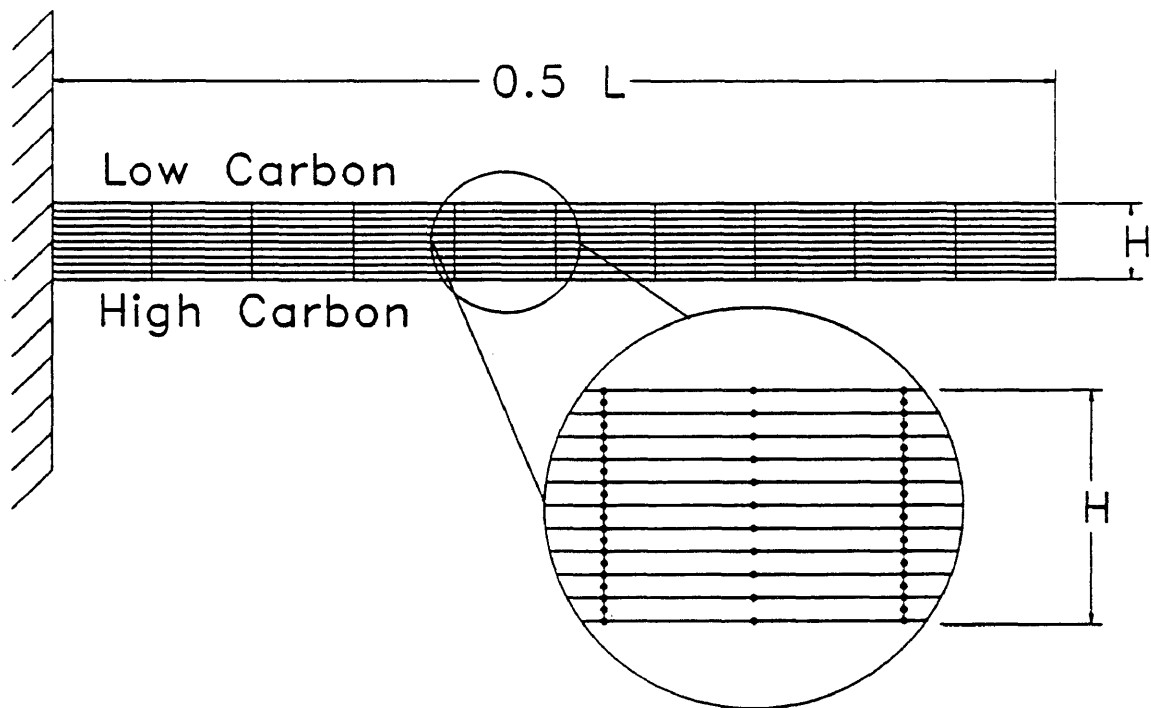


Figure 6.1 Finite element model used in this study consisting of 10 rows by 10 columns of eight noded isoparametric elements.

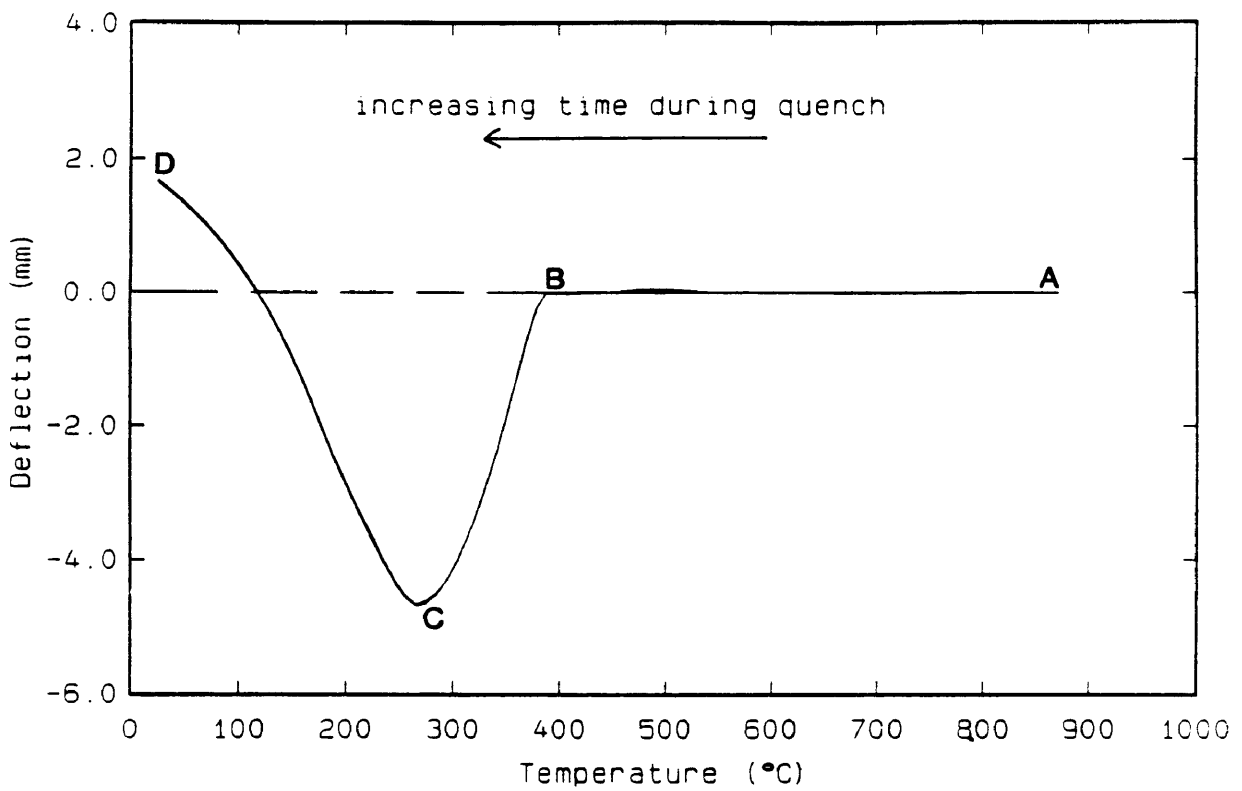


Figure 6.2 Deflection history for 2.03 millimeter SAE 4023 Almen strip model. The analysis begins at 871°C and continues to 25°C.

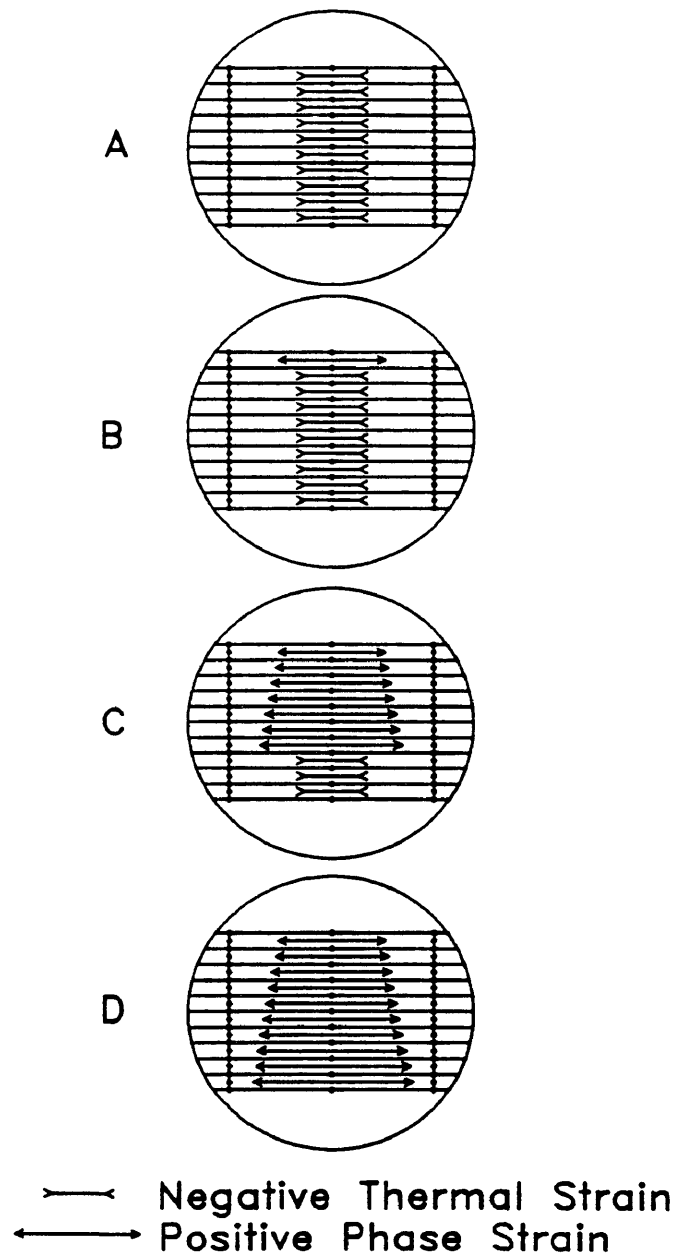


Figure 6.3 Schematic illustrating the relative strain distributions through the thickness of a typical Almen strip model at four temperatures indicated in Figure 6.2. The lower surface is the carburized surface.

transition is also symmetric, beginning at the surface and moving toward the model centerline). The model continues to contract axially until the temperature reaches the M_s temperature of the low carbon surface, indicated as temperature B in Figures 6.2 and 6.3.

At temperature B, the low carbon austenite at the upper surface of the Almen strip begins to transform to martensite (associated with this is a positive induced phase transformation strain). By superimposing a extensional phase strain on the contracted thermal strain, the low carbon surface of the Almen strip model transitions from plastic to elastic behavior. This relief of residual stress on the low carbon surface (and associated plastic-to-elastic transition) redistributes the existing symmetric stress profile to an unsymmetrical stress profile (about the model centerline). The martensitic expansion also forces the Almen strip model to deflect in a negative direction (low carbon surface convex). The martensitic phase transformation continues and moves across the model thickness from the low carbon surface, toward the high carbon surface. The amount of strain associated with the martensitic transformation also increases as the carbon level increases (shown in Figure 2.2).

At temperature C in Figures 6.2 and 6.3, the martensitic transformation has moved from the low carbon surface to some point below the centerline of the Almen strip model. A maximum negative deflection is reached where the expansion strains associated with phase transformation of the higher carbon martensite below the centerline balance the phase transformation strains of the lower carbon martensite above the centerline.

As the temperature decreases and the higher carbon austenite begins to transform, the model begins to deflect in a positive direction. The phase transformation (and associated plastic-to-elastic transition) continues until the high carbon M_s temperature is reached. The analysis continues elastically until the final ambient temperature, indicated as temperature D in Figures 6.2 and 6.3. The result is a net positive deflection of the Almen strip model (high carbon surface convex).

6.2 Microhardness, Carbon, and M_s Profiles

The conversion of microhardness data to a calculated carbon profile discussed in section 4.1 was the most accurate method available for determining the carbon distributions for the geometries studied. Possible sources of error exist, however. The conversion of microhardness measurements to HRC may be one such source. The calculated

carbon profiles presented in section 4.1 show the correct trends. They are of reasonable magnitude, but are most likely underestimated. Chrysler (8) has experimentally determined that the final surface carbon content for the SAE 4023 and SAE 4620 alloys should be about 0.86 weight percent carbon for the carburizing process numerically and experimentally considered in this study.

The calculated M_s profiles presented in section 4.1 also show the correct trends and are of reasonable magnitude. The sensitivity study considering the M_s temperature discussed in section 5.1 indicated that relatively small variations of the M_s temperature produce large variations in deflection and residual stresses. This is due to the path dependency of the elastic-plastic stress analysis. The time (or temperature) when the steel begins to transform to martensite has a significant effect on the final deflection and stress results.

6.3 Phase Transformation Analysis

The relationships incorporated in CSMCARB to determine the start temperature, rate of transformation and magnitude of dilatational phase strain is the most accurate data available. The phase transformation strain input data discussed in section 2.6, accurately represents the physical response of the SAE 4023 and SAE 4620 alloys. These data

were measured experimentally by Hildenwall (2) for a variety of alloys. Koistinen and Marburger's (20) relationship for the rate of the martensitic transformation is also the most accurate method available.

6.4 Mechanical Property Data

The relationships for the elastic modulus, yield strength, and strain hardening behavior incorporated in CSMCARB are the most accurate high temperature mechanical data available. Larson (29), however, believes that these data are inaccurate for the SAE 4023 and SAE 4620 alloys and that further studies can significantly improve the accuracy of the data presented in Hildenwall (2) to fit a greater variety of steel alloys.

6.5 Arc Deflection Results

The calculated arc deflections presented in Figure 4.23 and Table 4.2 are substantially different from the experimentally measured results. The intermediate calculated deflection results show the proper trends, however. The 1.30 millimeter Almen model yielded a negative deflection and the 3.18 millimeter model yielded the smallest positive deflection.

The 1.30 millimeter Almen strip model did not yield the largest positive deflection, as experimentally observed. Possible sources of error include the experimentally determined carbon profile (which subsequently yields an inaccurate M_s temperature which, in turn, alters the phase transformation behavior), the rate of transformation and magnitude of transformation strain, and the strain hardening behavior (which produces too great of an intermediate negative deflection) and transition plasticity (3,7,30). Transition plasticity is numerically simulated by decreasing the material's yield strength during the phase transformation. This yield strength decrease would significantly alter the stress generation and amount of plastic flow and, therefore, significantly affect the final deflection.

The final calculated arc deflection results for the 2.03, 2.44 and 3.18 millimeter Almen models also show the correct deflection trend. The larger the model thickness, the smaller the positive arc deflection.

The sensitivity study presented in section 5.0 showed that errors in selected input data used in this study can have a significant effect on the final calculated arc deflection results. The sensitivity study performed on the martensitic start temperature, for example, showed that a 20% variation in the calculated M_s temperature using

Andrew's linear equation can have a 38% variation associated with the final calculated arc deflection. This is due to the geometry selected for this study. The Almen strip geometry amplifies the distortion predicted by the elastic-plastic analysis. Hence, the geometry provides an excellent means for testing the adequacy of the constitutive model. The discrepancy in deflection results can also be attributed to one of (or combinations of) the numerical simplifying assumptions and input data.

6.6 Calculated Residual Stress Profiles

The calculated residual stress profiles shown in Figures 4.25-4.29 yielded reasonable results.

The residual stress profile for the 1.30 millimeter Almen model is shown in Figure 4.25. The calculated stress distribution yielded a tensile surface stress and centerline compressive stress. This distribution is opposite to what is physically expected. The large intermediate negative displacement and final negative displacement, discussed in section 6.5, is also unreasonable. Since the deflection results for the 1.30 millimeter Almen strip model were not physically reasonable, it is concluded that the predicted residual stress distribution will also be unreasonable.

The residual stress profiles for the other four thicknesses of Almen models that produced positive final

deflections are shown in Figures 4.26-4.29. These residual stress profiles are of reasonable magnitude and trend. The highest compressive residual stress is near the high carbon surface, as expected.

The calculated residual stress results for the 2.44 millimeter and 3.18 millimeter models did not, however, agree with the x-ray diffraction measurements performed by the Eaton Corporation. Eaton's measurements included a Moore-Evens relaxation correction. The final calculated positive deflection for the 2.44 millimeter Almen model was underestimated. Therefore the calculated residual stress profile should be overestimated when compared to the experimental measurements. The final calculated deflection for the 3.18 millimeter Almen model, however, was within 8% of the experimental result.

There are numerous possibilities to explain the discrepancy between the calculated and measured stress results. The constitutive data are probably not accurate for the alloys considered in this study. Specifically, the input data associated with the phase transformation are probably not accurate for the alloys and heat treatment process considered in this study. These data include the M_s temperature profile (determined from the carbon profile), the rate of transformation and the magnitude of transformation strain. Error associated with the strain

hardening behavior can also significantly affect the amount of plastic flow and, therefore, effect the calculated stress distribution. Neglecting transition plasticity can also significantly affect the calculated stress results. The relative amounts of martensite and retained austenite are considered using volumetric fractions only. Significant differences in stress can exist between the martensitic and austenitic microstructures.

7.0 CONCLUDING REMARKS

As an initial attempt to simulate numerically the distortion and residual stress development in carburized and quenched steel geometries, this study provided a great deal of interesting information. Following are various conclusions based on the results presented in sections 4.0 and 5.0 of this study.

7.1 Application of the Finite Element Method to Thermal-Elastic-Plastic Analyses

Based on the verification and quench analysis results presented, the numerical approach considered is not a viable method to determine the distortion and residual stress generated during quenching. The constitutive equation incorporated in the finite element program, CSMCARB, is sufficiently rigorous to simulate a variety of one-dimensional and two-dimensional verification problems proving that the derivation and implementation of the elastic-plastic constitutive equation in CSMCARB is correct. The material data, however, are not sufficiently accurate to yield reasonable results for the Almen strip analysis and, therefore, the effort and expense of FEM analyses is not justified.

7.2 Carbon Profile Determination

The method of determining the carbon profiles through the thickness of the Almen strip models was the most accurate available. Further investigation in this area could improve the accuracy of the analysis, however.

7.3 Simplifying Assumptions and Input Data

The simplifying assumptions and input data obtained from the literature discussed in sections 2.3, 2.4, 2.5, 2.6 and 2.7.2 were necessary to provide a reasonable scope to this study.

The simplifications for model material and thermomechanical coupling paths discussed in sections 2.3 and 2.4 provide a possible source of error. Further investigation is needed in these areas.

The only significant thermal property that requires further investigation for the geometries discussed in this study is the convection coefficient. The time-temperature history for the Almen strip models is controlled by the rate of convective heat loss.

The most questionable input data used in this study are the mechanical property data discussed in section 2.7.2. Accurate high temperature mechanical property data are not readily available in the literature. Future investigations in this area could provide significantly better numerical

modeling results.

Experimental studies should be initiated to provide better thermal, phase transformation, and mechanical input data for incorporation into numerical programs, such as CSMCARB. Once proper correlation is achieved between experimental and numerical results, the numerical methods can be expanded to include more complex geometries.

8.0 SUGGESTIONS FOR FUTURE WORK

Based on the results of this study, the following suggestions are presented to aid future investigators considering a study in analysis of carburized and quenched steel geometries.

8.1 Numerical Considerations

To simulate numerically the distortion and residual stress development of more complicated geometries including analyses of gear tooth involute shapes, CSMCARB must be modified to permit axisymmetric analyses. This will also add the ability to compare results of CSMCARB to the results obtained from numerical and experimental studies found in the literature.

Kinematic hardening and anisotropy due to prior forming operations (i.e. rolling, forging, etc.) should also be investigated.

8.2 Thermomechanical Coupling

This study considered three of the six coupling paths discussed in section 2.1. The paths not considered for this study should be investigated to determine whether the simplifying assumptions considered in this study were justified.

8.3 Carbon Profile and Phase Transformation Analysis

A more accurate numerical determination of the carbon profile is recommended. Suggestions include considering the diffusivity of carbon in austenite as a function of alloy additions (29) and incorporating a gas atmosphere analysis (31,32,33) into the thermomechanical analysis.

Experimental dilatometric testing should be performed for the alloy of interest and various carbon levels to determine directly the thermal and phase transformation strains on cooling.

This study considered the diffusionless martensitic transformation only. For geometries that experience slower cooling rates, CSMCARB should be modified to permit transformations to all product phases (i.e. ferrite, pearlite, bainite, martensite and cementite).

8.4 High Temperature Mechanical Properties

Further investigation is needed to determine reliable high temperature mechanical properties for incorporation into CSMCARB. Specifically, high temperature tensile or compressive testing should be performed to determine better relationships for elastic modulus, yield strength and strain hardening behavior for a variety of carburizing grade alloys as a function of temperature, carbon content and phase.

9.0 REFERENCES

1. Burnett, J. "Evaluation of Elastic-Plastic Stresses in Quenched Carburized Cylinders by Finite Element Methods." Ph.D. Diss., University of Akron, Akron, OH., 1977.
2. Hildenwall, B. "Prediction of the Residual Stresses Created During Quenching - Especially the Quench Response in Carburized Steels." Linköping Studies in Science and Technology, Ph.D. Diss. 39, Linköping, Sweden, 1979.
3. Sjöström, S. "The Calculation of Quench Stresses in Steel." Linköping Studies in Science and Technology, Ph.D. Diss. 84, Linköping Sweden, 1982.
4. Dougherty, J. "Thermal-Elastic-Visco-Plastic Finite Element Analysis of Heat Treatment Processes for Carburized Components." Masters Thesis, University of Akron, Akron, OH., 1987.
5. Beck, G. and Ericsson, T. "Prediction of Residual Stresses due to Heat Treatment." Residual Stresses in Science and Technology Informationsgesellschaft-Verlag, 1 (1987): 27-40.
6. Mayr, P. "Dimensional Alterations due to Heat Treatment." Residual Stresses in Science and Technology, Informationsgesellschaft-Verlag, 1 (1987): 57-78.
7. Fletcher, A. Thermal Stress and Strain Generation in Heat Treatment. Elsevier Science Publishing Co., New York, NY, 1989.
8. Meeting between Chrysler representatives J. Hoffmann, M. Schiemann, R. Scheiman and A. Freda and ASPPRC representatives G. Krauss, C. Van Tyne, M. Henriksen, K. Erven and D. Larson, March 1989.
9. Krauss, G. Principles of Heat Treatment of Steel. American Society of Metals, Metals Park, OH, 1980.
10. Ebert, L. "The Role of Residual Stresses in the Mechanical Performance of Case Carburized Steels." Metallurgical Transactions A, 9A (1978): 1537-1551.

11. Koistinen, D. "The Distribution of Residual Stresses in Carburized Cases and Their Origin." Transactions of the ASM, 50 (1958): 227-241.
12. Timoshenko, S. and Goodier, J. Theory of Elasticity. McGraw-Hill, New York, NY, 1951.
13. Weiner, J. and Huddleston, J. "Transient and Residual Stresses in Heat-Treated Cylinders." Journal of Applied Mechanics Trans. ASME, 26 (1959-Series E): 31-39.
14. Boley, B. and Weiner, J. Theory of Thermal Stress. John Wiley, New York, NY, 1967.
15. Fujio, H., Aida, T, and Akizono, J. "Distortions and Residual Stresses of Gears Caused by Hardening (4th Report, Case Hardening of Gears)." Bulletin of the Japanese Society of Mechanical Engineers, 22 (1979): 1009-1016.
16. Fujio, H., Aida, T, Aratake, T, and Hosoi, E. "Distortions and Residual Stresses of Gears Caused by Hardening - (5th Report, Gear with Limited Face Width)." Bulletin of the Japanese Society of Mechanical Engineers, 24 (1981): 591-598.
17. Habraken, A. "Coupled Thermo-Mechanical Analysis with Microstructural Computation of Steel Pieces." Proceeding of Numiform 89 (1989): 165-170.
18. Price, R. and Fletcher, A. "Determination of Surface Heat-Transfer Coefficients during Quenching of Steel Plates." Metals Technology, Vol. II (1980): 203-211.
19. Andrews, K. "Empirical Formulae for the Calculation of Some Transformation Temperatures." Journal of the Iron and Steel Institute, 203 (1965): 721-727.
20. Koistinen, D. and Marburger, R. "A General Equation Prescribing the Extent of the Austenite-Martensite Transformation in Pure Iron-Carbon Alloys and Plain Carbon Steels." ACTA Metallurgia, 7 (1959): 59-60.
21. Bathe, K. Finite Element Procedures in Engineering Analysis. Prentice-Hall, Inc., Englewood Cliffs, NJ, 1982.

22. Zienkiewicz, O., Valliappan, S. and King, I. "Elasto-Plastic Solutions of Engineering Problems 'Initial Stress' Finite Element Approach." International Journal for Numerical Methods in Engineering, 1 (1965): 75-100.
23. Nayak, G. and Zienkiewicz, O. "Elasto-Plastic Analysis, a Generalization for Various Constitutive Relations Including Strain Softening." International Journal for Numerical Methods in Engineering, 5 (1972): 113-135.
24. Owen, D. and Hinton, E. Finite Elements in Plasticity. Pineridge Press Limited, Swansea, U.K., 1980.
25. Chung, T. Continuum Mechanics, Prentice-Hall, Englewood Cliffs, NJ, 1988.
26. Reddy, J. An Introduction to the Finite Element Method, McGraw-Hill, New York, NY, 1984.
27. Grange, R., Hribal, C. and Porter, L. "Hardness of Tempered Martensite in Carbon and Low-Alloy Steels." Metallurgical Transactions A, 8A (1977): 1775-1785.
28. Metal Improvement Company Shot Peening Applications, 7th ed., Metal Improvement Company, Inc., Paramus, NJ.
29. Meeting between R. Larson, Senior Divisional Metallurgist, Eaton Corporation and ASPPRC representatives C. Van Tyne and D. Larson, October 1990.
30. Denis, S. and Simon, A. "Discussion on the Role of Transformation Plasticity in the Calculation of Quench Stresses in Steels." Residual Stresses in Science and Technology, Informationsgesellschaft-Verlag, 2 (1987): 565-572.
31. Reti, T., Reger, M. and Gergely, M. "A Practical Method for the Computer Prediction of Technological Parameters of Two-Stage Gas Carburizing." Heat Treatment and Surface Engineering, Proceedings of the 6th International Congress on Heat Treatment of Materials, ASM International, Materials Park, OH (1988): 95-98.
32. Stickels, C. "Gas Carburizing in Batch Furnaces: A Computer Model." Heat Treatment and Surface Engineering, Proceedings of the 6th International Congress on Heat Treatment of Materials, ASM

- International, Materials Park, OH (1988): 99-102.
33. McCurdy, D. "Software Simulation of Atmosphere Carburizing and Hardening." Carburizing: Processing and Performance, Proceedings of an International Conference, ASM International, Materials Park, OH (1989): 71-81.
34. Dieter, G. Mechanical Metallurgy. 3rd Edition. McGraw Hill, New York, NY, 1986.

APPENDIX A Derivation of an Implicit Integration Scheme to Determine the Transient Temperature Distribution During Quenching

The θ -method was derived specifically for this work to numerically determine the transient temperature distribution during quenching. This derivation assumes flux (first derivative with respect to time) varies linearly from time t to time $t+\theta\Delta t$, where $\theta \geq 1.0$. For unconditional stability, it has been shown for similar derivations that $\theta \geq 1.37$, and thus a value of $\theta=1.40$ is commonly used (21).

The differential equation representing the transient temperature distribution during quenching is given by:

$$\frac{\partial T}{\partial t} - \frac{\partial}{\partial x} \left(\alpha \frac{\partial T}{\partial x} \right) = 0 \quad (\text{A.1})$$

where

T = temperature
 $\alpha = k / (\rho c_p) =$ thermal diffusivity
 K = conductivity
 $\rho =$ density
 $c_p =$ specific heat
 $t^p =$ time
 x = position

The finite element formulation for the equations of equilibrium governing the linear dynamic response of a system of finite elements is explained in Bathe (21). This derivation will explain the integration scheme only.

For this derivation, a generic second order transient partial differential equation is considered, given by:

$$\frac{\partial \mathbf{A}}{\partial t} - \frac{\partial}{\partial \mathbf{x}} \left(\mathbf{D} \frac{\partial \mathbf{A}}{\partial \mathbf{x}} \right) = 0 \quad (\text{A.2})$$

where

A = primary variable valid over the domain (0,L)
 D = diffusivity
 t = time
 x = position

The equilibrium equation is given by:

$$[\mathbf{C}]\{\dot{\mathbf{A}}\} + [\mathbf{K}]\{\mathbf{A}\} = \{\mathbf{R}\} \quad (\text{A.3})$$

where

[C] is the damping matrix
 [K] is the stiffness matrix
 {R} is the flux vector

The unknown variables, {A} and { $\dot{\mathbf{A}}$ }, in equation (A.3) cannot be found simultaneously. An integration scheme is necessary to find a relationship for { $\dot{\mathbf{A}}$ } as a function of {A}. This is accomplished using the θ -method, described below.

Let τ denote the increase in time, where $\theta \leq \tau \leq \theta \Delta t$; then for the time interval t to $t + \theta \Delta t$, it is assumed that:

$$\{\dot{\mathbf{A}}^{t+\tau}\} = \{\dot{\mathbf{A}}^\tau\} + \frac{\tau}{\theta \Delta t} \{\dot{\mathbf{A}}^{t+\theta \Delta t} - \dot{\mathbf{A}}^t\} \quad (\text{A.4})$$

Integrating (A.4), one obtains:

$$\{\mathbf{A}^{t+\tau}\} = \{\mathbf{A}^t\} + \tau \{\dot{\mathbf{A}}^t\} + \frac{\tau^2}{2\theta \Delta t} \{\dot{\mathbf{A}}^{t+\theta \Delta t} - \dot{\mathbf{A}}^t\} \quad (\text{A.5})$$

Evaluating (A.5) at time $t + \theta \Delta t$ (i.e. $\tau = \theta \Delta t$) yields:

$$\{\mathbf{A}^{t+\theta \Delta t}\} = \{\mathbf{A}^t\} + \theta \Delta t \{\dot{\mathbf{A}}^t\} + \frac{\theta \Delta t}{2} \{\dot{\mathbf{A}}^{t+\theta \Delta t} - \dot{\mathbf{A}}^t\} \quad (\text{A.6})$$

Expanding and rearranging (A.6) yields:

$$\begin{aligned} \{\mathbf{A}^{t+\theta \Delta t}\} - \{\mathbf{A}^t\} - \theta \Delta t \{\dot{\mathbf{A}}^t\} + \frac{\theta \Delta t}{2} \{\dot{\mathbf{A}}^t\} \\ = \frac{\theta \Delta t}{2} \{\dot{\mathbf{A}}^{t+\theta \Delta t}\} \end{aligned} \quad (\text{A.7})$$

Solving (A.7) for $\dot{\mathbf{A}}^{t+\theta \Delta t}$ in yields:

$$\{\dot{\mathbf{A}}^{t+\theta \Delta t}\} = \frac{2}{\theta \Delta t} \{\mathbf{A}^{t+\theta \Delta t}\} - \frac{2}{\theta \Delta t} \{\mathbf{A}^t\} - 2\{\dot{\mathbf{A}}^t\} + \{\dot{\mathbf{A}}^t\} \quad (\text{A.8})$$

Equation (A.8) can be simplified to:

$$\{\dot{\mathbf{A}}^{t+\theta\Delta t}\} = \frac{2}{\theta\Delta t} \{\mathbf{A}^{t+\theta\Delta t} - \mathbf{A}^t\} - \{\dot{\mathbf{A}}^t\} \quad (\text{A.9})$$

To obtain the solution for \mathbf{A} and $\dot{\mathbf{A}}$ at time $t+\Delta t$, the equilibrium equation (A.3), is evaluated at time $t+\theta\Delta t$.

This is given by:

$$[\mathbf{C}]\{\dot{\mathbf{A}}^{t+\theta\Delta t}\} + [\mathbf{K}]\{\mathbf{A}^{t+\theta\Delta t}\} = \{\mathbf{R}^{t+\theta\Delta t}\} \quad (\text{A.10})$$

By substituting the relationship for $\dot{\mathbf{A}}^{t+\theta\Delta t}$ in (A.9) into (A.10), the new equilibrium equation is given by:

$$\begin{aligned} & [\mathbf{C}]\left\{\frac{2}{\theta\Delta t}\{\mathbf{A}^{t+\theta\Delta t} - \mathbf{A}^t\} - \{\dot{\mathbf{A}}^t\}\right\} \\ & + [\mathbf{K}]\{\mathbf{A}^{t+\theta\Delta t}\} = \{\mathbf{R}^{t+\theta\Delta t}\} \end{aligned} \quad (\text{A.11})$$

Rearranging (A.11) yields:

$$\begin{aligned} & \frac{2}{\theta\Delta t} [\mathbf{C}]\{\mathbf{A}^{t+\theta\Delta t}\} + [\mathbf{K}]\{\mathbf{A}^{t+\theta\Delta t}\} \\ & = \{\mathbf{R}^{t+\theta\Delta t}\} + \frac{2}{\theta\Delta t} [\mathbf{C}]\{\mathbf{A}^t\} + [\mathbf{C}]\{\dot{\mathbf{A}}^t\} \end{aligned} \quad (\text{A.12})$$

Rewriting (A.12) yields the following equation:

$$\begin{aligned} & \left\{\frac{2}{\theta\Delta t} [\mathbf{C}] + [\mathbf{K}]\right\} \{\mathbf{A}^{t+\theta\Delta t}\} \\ & = \{\mathbf{R}^{t+\theta\Delta t}\} + \frac{2}{\theta\Delta t} [\mathbf{C}]\{\mathbf{A}^t\} + [\mathbf{C}]\{\dot{\mathbf{A}}^t\} \end{aligned} \quad (\text{A.13})$$

An effective stiffness matrix and effective flux vector can be defined by:

$$[\hat{\mathbf{K}}] = \left(\frac{2}{\theta \Delta t} [\mathbf{C}] + [\mathbf{K}] \right) \quad (\text{A.14})$$

$$\{\hat{\mathbf{R}}^{t+\theta \Delta t}\} = \{\mathbf{R}^{t+\theta \Delta t}\} + \frac{2}{\theta \Delta t} [\mathbf{C}] \{\mathbf{A}^t\} + [\mathbf{C}] \{\dot{\mathbf{A}}^t\}$$

By substituting the effective matrices given in (A.14) into (A.13), a simplified relationship results, given by:

$$[\hat{\mathbf{K}}] \{\mathbf{A}^{t+\theta \Delta t}\} = \{\hat{\mathbf{R}}\} \quad (\text{A.15})$$

$\mathbf{A}^{t+\theta \Delta t}$ is found by inverting the effective stiffness matrix in (A.15). $\dot{\mathbf{A}}^{t+\theta \Delta t}$ can then be found by using equation (A.9). Finally, $\mathbf{A}^{t+\Delta t}$ and $\dot{\mathbf{A}}^{t+\Delta t}$ are found using the following equations:

$$\{\mathbf{A}^{t+\Delta t}\} = \{\mathbf{A}^t\} + \Delta t \{\dot{\mathbf{A}}^t\} + \frac{\Delta t}{2\theta} \{\dot{\mathbf{A}}^{t+\theta \Delta t} - \dot{\mathbf{A}}^t\} \quad (\text{A.16})$$

$$\{\dot{\mathbf{A}}^{t+\Delta t}\} = \{\dot{\mathbf{A}}^t\} + \frac{1}{\theta} \{\dot{\mathbf{A}}^{t+\theta \Delta t} - \dot{\mathbf{A}}^t\} \quad (\text{A.17})$$

APPENDIX B Thermal, Phase and Mechanical Properties
Incorporated in CSMCARB.

Following is the thermal, phase transformation and mechanical input data relationships incorporated in CSMCARB.

1. Relative Phases and Volumetric Weighing

The relative volumetric amounts of austenite and martensite are calculated using the same notation as Hildenwall and Sjöström (2,3). The sum of the individual volumetric fractions of austenite and product phases is one. This relationship is given as:

$$1 = \sum_{i=1}^6 v_i$$

where

v_i is the volumetric fraction of the i th phase

i=1 : austenite
i=2 : ferrite
i=3 : pearlite
v=4 : bainite
v=5 : martensite
v=6 : cementite

For this study, the martensitic transformation is the only phase transformation considered. Therefore, v_2 , v_3 , v_4 , and v_6 are zero.

2. Thermal Conductivity

The thermal conductivity as a function of temperature and phase for the SAE 4023 and SAE 4620 alloys is assumed to follow the relationship given in Hildenwall (2). This relationship is given by:

$$K = \sum_{i=1}^6 v_i (K_{0,i} + K_{1,i}T + K_{2,i}T^2 + K_{3,i}T^3) \left(\frac{W}{m^{\circ}C} \right)$$

where T is the temperature in degrees C and K_0 , K_1 , K_2 and K_3 for each phase is given in Table B.1.

Table B.1
Coefficients for Thermal Conductivity

| phase | K_0 | K_1 (x 10^3) | K_2 (x 10^6) | K_3 (x 10^9) |
|-------|-------|----------------------|----------------------|----------------------|
| 1 | 14.60 | 13.56 | 0 | 0 |
| 2 | 59.00 | -22.22 | 0 | 0 |
| 3 | 38.40 | 22.40 | -78.86 | 36.38 |
| 4 | 33.55 | 48.55 | -179.6 | 116.5 |
| 5 | 25.10 | 2.778 | 0 | 0 |
| 6 | 0 | 0 | 0 | 0 |

Figure B.1 illustrates the thermal conductivity, K, as a function of temperature for a 0.23 weight percent SAE 4023 alloy steel transforming from austenite to martensite ($M_s = 415^{\circ}C$) beginning at $871^{\circ}C$ and continuing to $25^{\circ}C$.

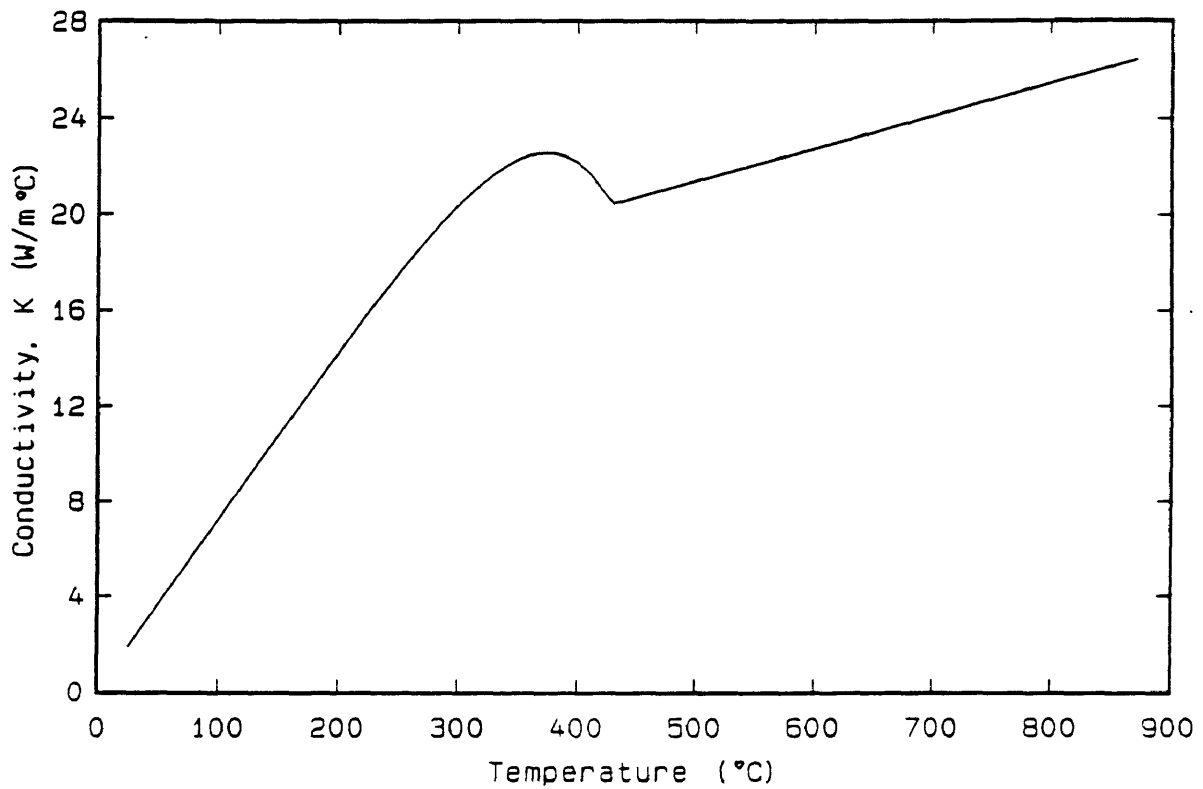


Figure B.1 Thermal conductivity, K , as a function of temperature for a 0.23 weight percent SAE 4023 alloy steel transforming from austenite to martensite ($M_s = 415^\circ\text{C}$) beginning at 871°C and continuing to 25°C .

3. Specific Heat

Specific heat as a function of temperature and phase for the SAE 4023 and SAE 4620 alloys is assumed to follow the relationship presented in Hildenwall (2). This relationship is given by:

$$C_p = \sum_{i=1}^6 v_i (C_{p_{0,i}} + C_{p_{1,i}}T + C_{p_{2,i}}T^2 + C_{p_{3,i}}T^3) \left(\frac{J}{Kg^{\circ}C} \right)$$

where T is the temperature in degrees C and C_{p_0} , C_{p_1} , C_{p_2} and C_{p_3} for each phase is given in Table B.2.

Table B.2
Coefficients for Specific Heat

| phase | C_{p_0} | C_{p_1} | C_{p_2} (x 10^3) | C_{p_3} (x 10^6) |
|-------|-----------|-----------|--------------------------|--------------------------|
| 1 | 375 | 0.333 | 0 | 0 |
| 2 | 445 | 0.8073 | -1.993 | 2.572 |
| 3 | 445 | 0.8073 | -1.993 | 2.572 |
| 4 | 443 | 0.8073 | -1.993 | 2.572 |
| 5 | 448 | 0.8073 | -1.993 | 2.572 |
| 6 | 0 | 0 | 0 | 0 |

Figure B.2 illustrates the specific heat, C_p , as a function of temperature for a 0.23 weight percent SAE 4023 alloy steel transforming from austenite to martensite ($M_s = 415^{\circ}C$) beginning at $871^{\circ}C$ and continuing to $25^{\circ}C$.

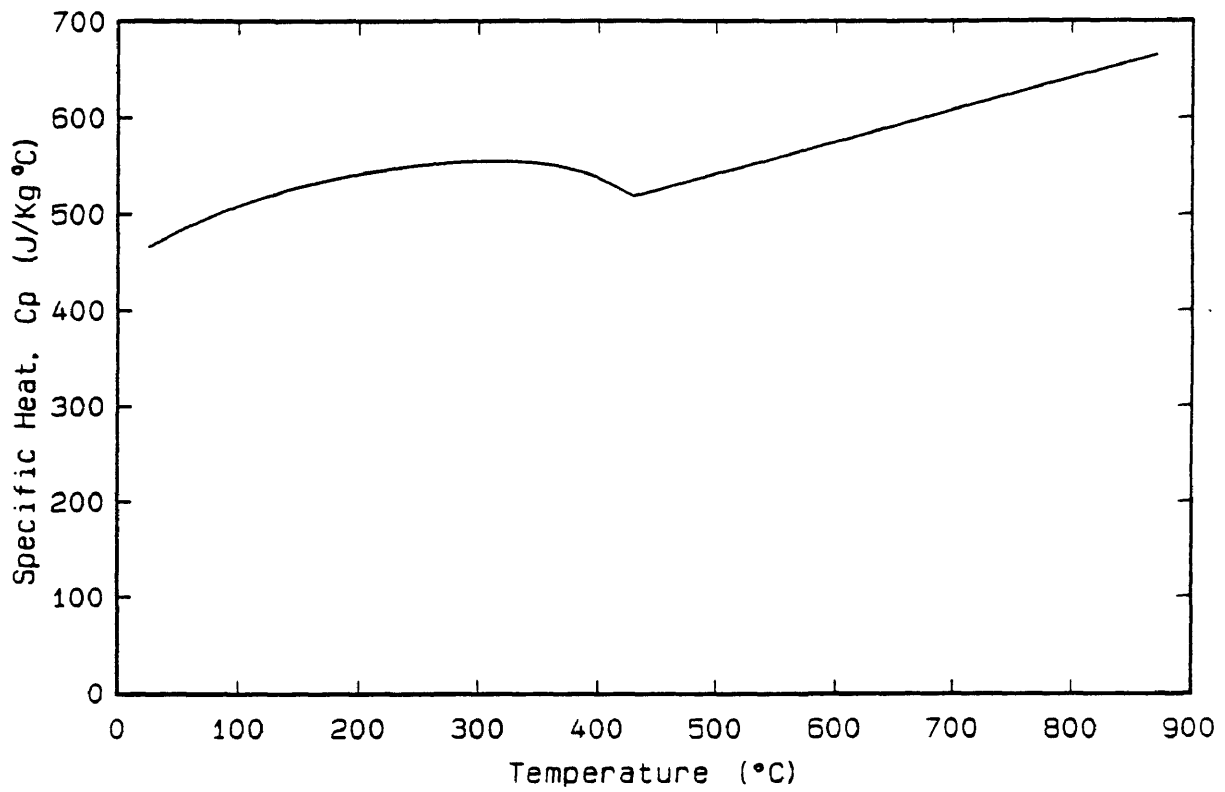


Figure B.2 Specific heat, C_p , as a function of temperature for a 0.23 weight percent SAE 4023 alloy steel transforming from austenite to martensite ($M_s = 415^\circ\text{C}$) beginning at 871°C and continuing to 25°C .

4. Density

The steel density as a function of temperature, carbon content, and phase for the SAE 4023 and SAE 4620 alloys is assumed to follow the relationship presented in Hildenwall (2). This relationship is given by:

$$\rho = \sum_{i=1}^6 v_i \left(\frac{\rho_{0,i} + \rho_{1,i}C + \rho_{2,i}C^2}{(1 + 3T\alpha)} \right) \left(\frac{\text{Kg}}{\text{m}^3} \right)$$

where T is the temperature in degrees C, α is the coefficient of thermal expansion (section 6.) and C is the carbon concentration in weight percent and ρ_0 , ρ_1 , and ρ_2 for each phase is given in Table B.3.

Table B.3
Coefficients for Density

| phase | ρ_0 | ρ_1 | ρ_2 |
|-------|----------|----------|----------|
| 1 | 8056 | 0 | 0 |
| 2 | 7860 | 0 | 0 |
| 3 | 7860 | 46 | -0.27 |
| 4 | 7860 | 39.9 | -0.113 |
| 5 | 7860 | -64.4 | 0.528 |
| 6 | 7860 | 0 | 0 |

Figure B.3 shows steel density, ρ , as a function of temperature for a 0.23 weight percent SAE 4023 alloy steel transforming from austenite to martensite ($M_s = 415^\circ\text{C}$) beginning at 871°C and continuing to 25°C .

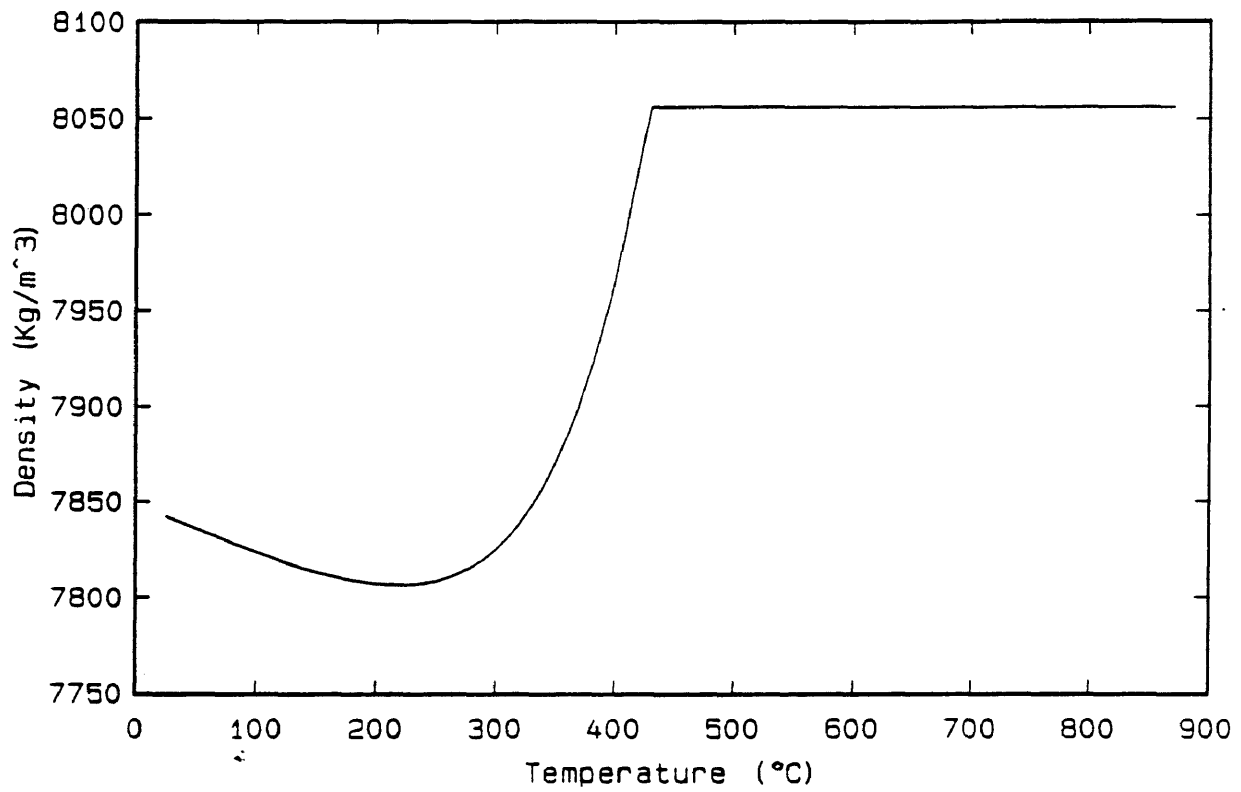


Figure B.3 Density, ρ , as a function of temperature for a 0.23 weight percent SAE 4023 alloy steel transforming from austenite to martensite ($M_s = 415^\circ\text{C}$) beginning at 871°C and continuing to 25°C .

5. Convective Heat Loss Coefficient

The convective heat loss coefficient for SAE 4023 and SAE 4620 alloy steel immersed in oil over the temperature range $176^{\circ}\text{C} < T < 871^{\circ}\text{C}$ is assumed to follow the relationship presented in Price and Fletcher (18). Figure B.4 shows the convective heat loss coefficient, h_c , as a function of temperature. Table B.4 lists specific values for the convective heat loss coefficient, h_c , as a function of temperature. Linear interpolation was used for temperatures between the tabulated values.

Table B.4
Convection Coefficient Data

| Temperature ($^{\circ}\text{C}$) | h_c $\text{W}/\text{m}^2\text{K}$ |
|---------------------------------------|--|
| 100 | 320 |
| 300 | 520 |
| 430 | 2000 |
| 480 | 2000 |
| 540 | 520 |
| 800 | 820 |
| 1000 | 820 |

The convective heat loss coefficient for steel in air for the temperature range $25^{\circ}\text{C} < T < 176^{\circ}\text{C}$ was assumed to be a constant of $300 \text{ W}/\text{m}^2\text{K}$. This coefficient must be altered to a more accurate value when transformation to intermediate phases is considered.

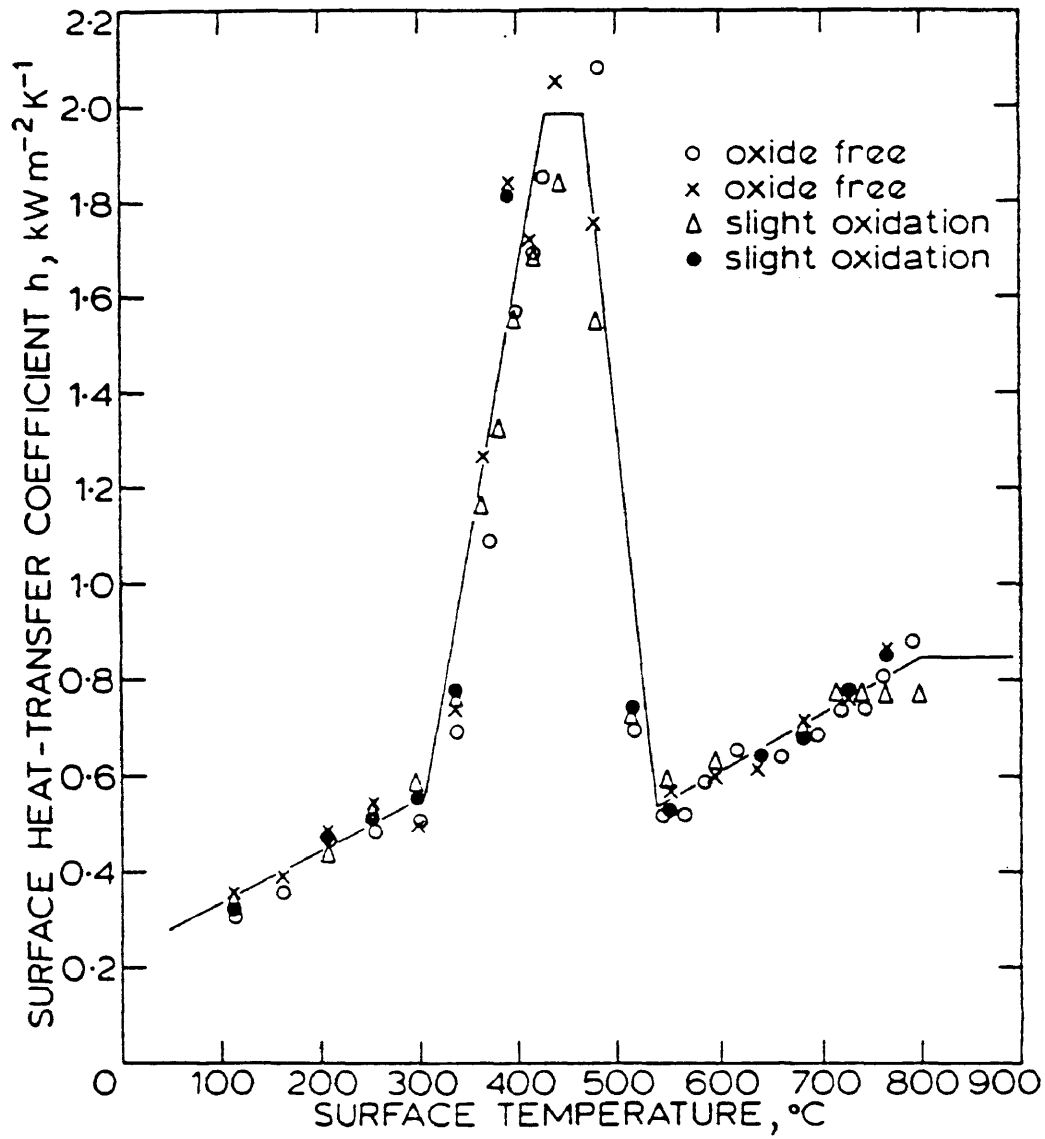


Figure B.4 The convective heat loss coefficient, h_c , as a function of temperature for steel immersed in oil (18).

6. Coefficient of Thermal Expansion

The coefficient of thermal expansion for the SAE 4023 and SAE 4620 alloy steels is assumed to follow the relationship presented in Hildenwall (2). This relationship is given by:

$$\alpha = (\alpha_1 + \alpha_2 C) + (\alpha_3 + \alpha_4 C) T + \alpha_5 T^2 \quad (^\circ\text{C}^{-1})$$

where T is the temperature in degrees C, C is the carbon concentration in weight percent and α_1 , α_2 , α_3 , α_4 , and α_5 for the various phases is given in Table B.5.

Table B.5
Coefficients for the Coefficient of Thermal Expansion

| phase | α_1 (x 10^6) | α_2 (x 10^6) | α_3 (x 10^9) | α_4 (x 10^9) | α_5 (x 10^{12}) |
|-------|---------------------------|---------------------------|---------------------------|---------------------------|------------------------------|
| 1 | 22.38 | 0 | 0 | 0 | 0 |
| 2 | 13.0 | -4.3 | 5.8 | 2.8 | -2.05 |
| 3 | 13.0 | -4.3 | 5.8 | 2.8 | -2.05 |
| 4 | 13.0 | -4.3 | 5.8 | 2.8 | -2.05 |
| 5 | 13.0 | -4.3 | 5.8 | 2.8 | -2.05 |
| 6 | 13.0 | -4.3 | 5.8 | 2.8 | -2.05 |

Figure B.5 shows the coefficient of thermal expansion, α , as a function of temperature and carbon content for ferrite, pearlite, bainite, martensite and cementite.

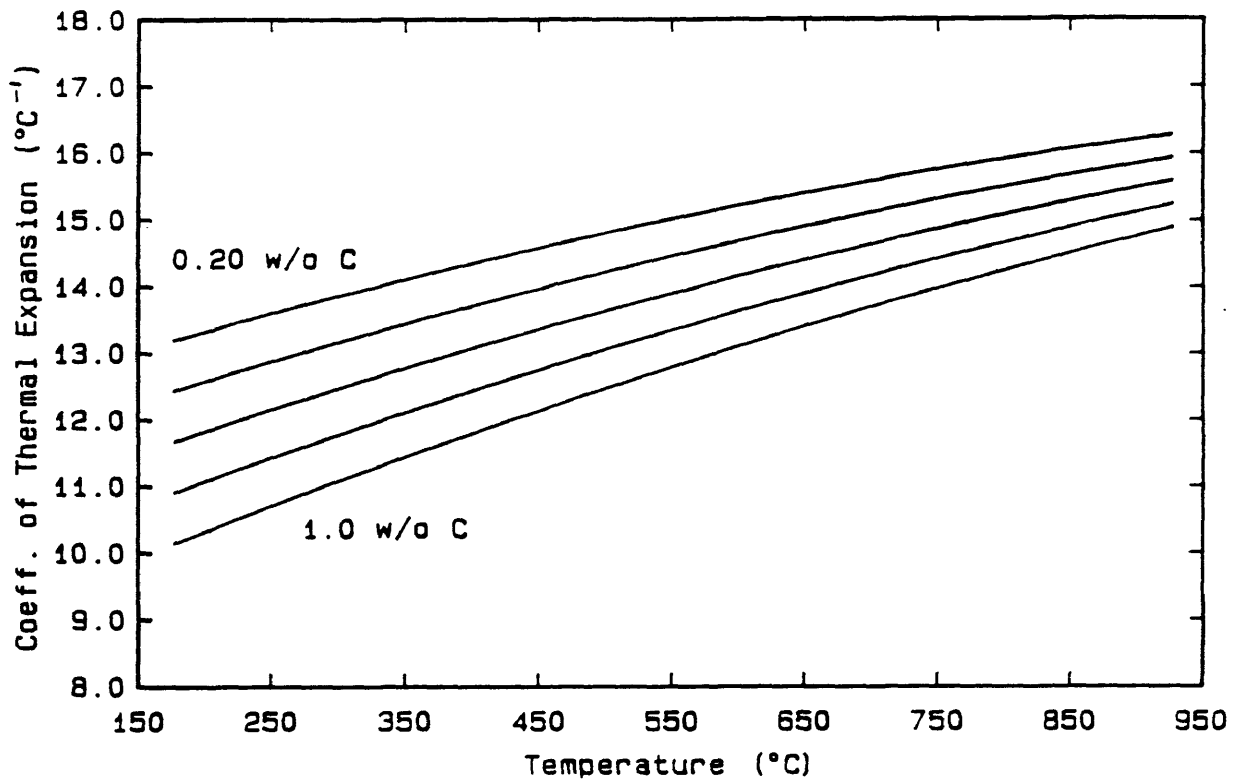


Figure B.5 The coefficient of thermal expansion, α , as a function of temperature and carbon content for ferrite, pearlite, bainite, martensite and cementite.

7. Andrew's Linear Equation

Andrew's linear equation (19) is used in this study to determine the martensite start temperature, M_s , for the SAE 4023 and SAE 4620 alloys during the quench. This relationship is given by:

$$M_s = 539 - 423C - 30.4Mn \\ - 12.1Cr - 17.7Ni - 7.5Mo \quad (^\circ C)$$

where C is the carbon concentration in weight percent and Mn, Cr, Ni, and Mo are the concentrations of the other appropriate alloying additions in weight percent. Figure B.6 shows the inverse relationship using Andrew's linear equation between the M_s temperature and carbon concentration.

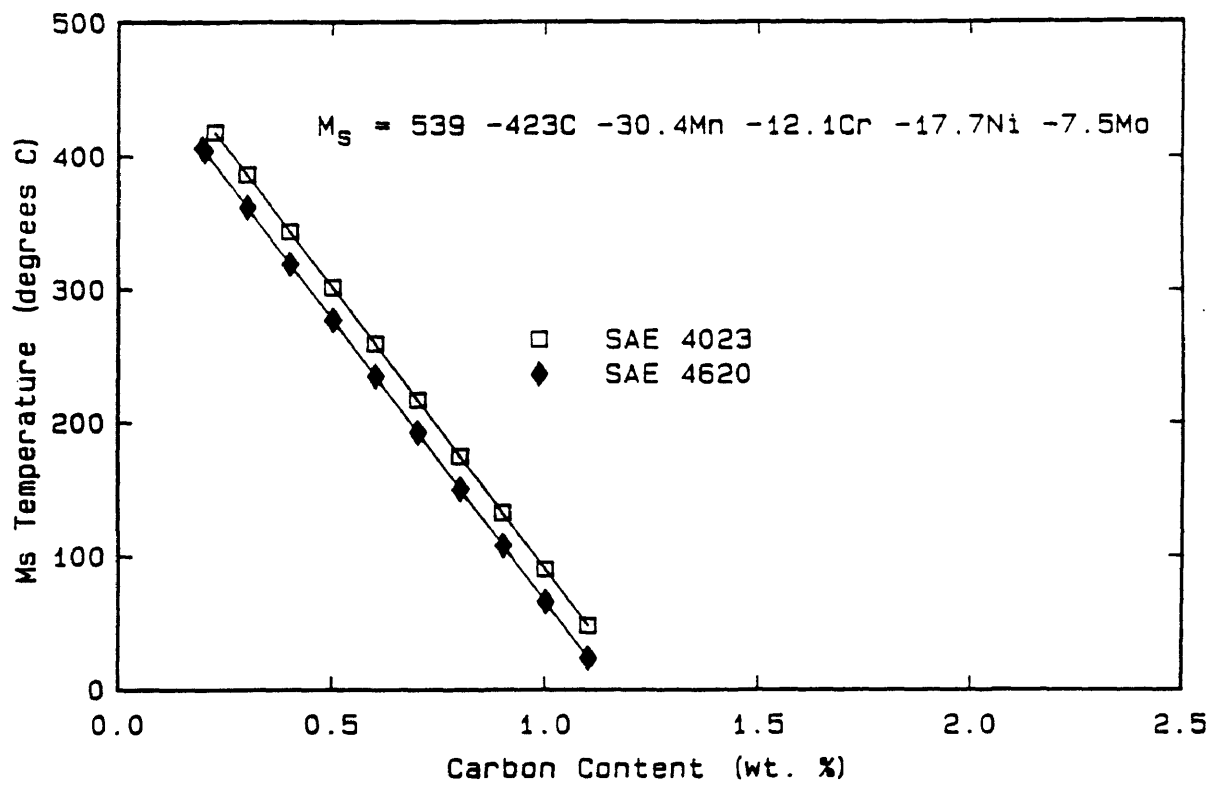


Figure B.6 The martensite start temperature, M_s , as a function of carbon concentration for the SAE 4023 and SAE 4620 alloy steels using Andrew's linear equation.

8. Koistinen and Marburger's Relationship for the Formation of Martensite

Koistinen and Marburger's relationship (20) is incorporated in CSMCARB to determine the relative volumetric fractions of austenite and martensite as a function of temperature. This relationship is given by:

$$v_5 = 1 - e^{-0.011(M_s - T)} \quad M_s < T$$

$$v_1 = 1 - v_2 - v_3 - v_4 - v_5 - v_6$$

where T is the temperature in degrees C and v_i represents the volumetric fraction of the *i*th phase, as described in section 1. Figure B.7 shows the volume fraction of martensite formed as a function of temperature for steels of 0.20, 0.50 and 0.80 weight percent carbon.

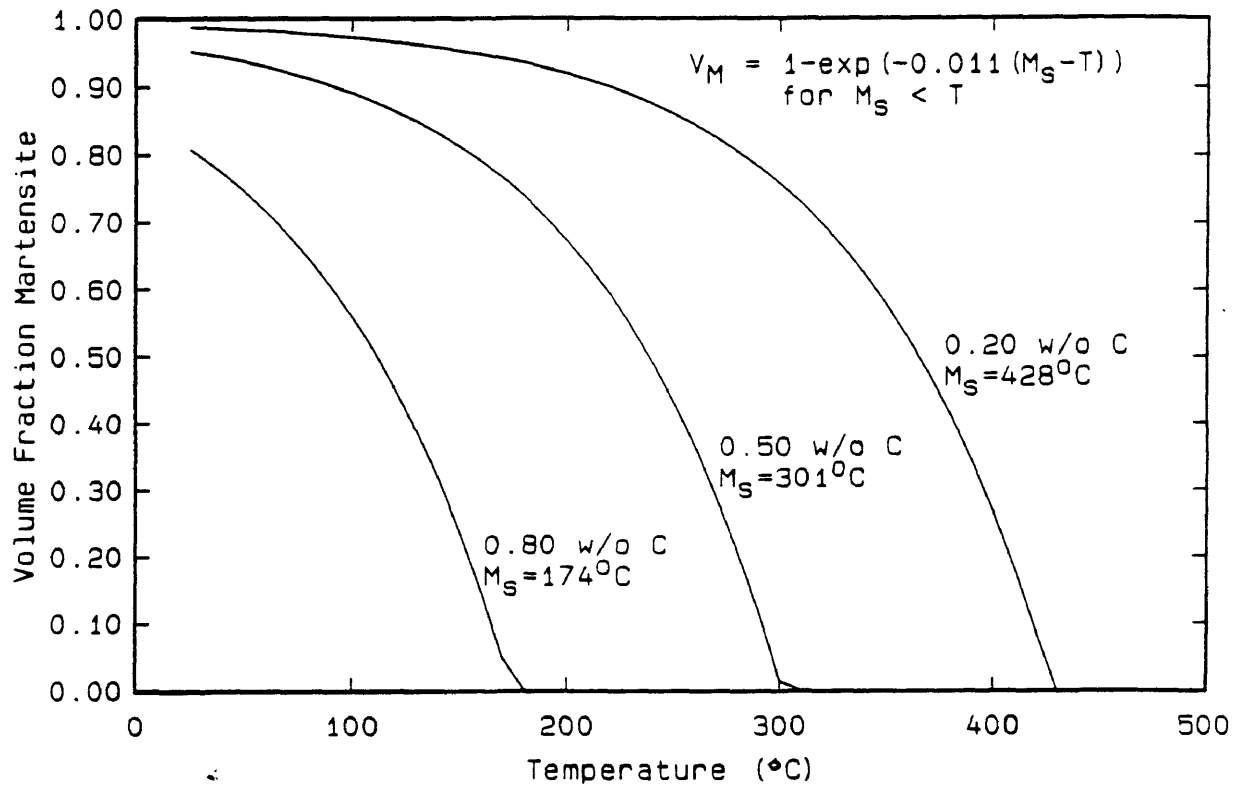


Figure B.7 The volume fraction of martensite formed as a function of temperature for steels of 0.20, 0.50 and 0.80 weight percent carbon.

9. Phase Transformation Strain

The linear dilatometric strains associated with the martensitic transformation of the SAE 4023 and SAE 4620 alloy steels are assumed to follow the experimental data presented in Hildenwall (2). These experimental values for various carbon concentrations are given in Table B.6.

Table B.6
Linear Dilatometric Strain Associated
with Transformation to the Indicated Phases

| phase | 0.18 w/o C | 0.39 w/o C | 0.58 w/o C | 0.74 w/o C |
|-------|------------|------------|------------|------------|
| 1 | 0 | 0 | 0 | 0 |
| 2 | 0.00802 | 0.00741 | 0.00706 | 0.00689 |
| 3 | 0.00802 | 0.00741 | 0.00706 | 0.00689 |
| 4 | 0.00971 | 0.00812 | 0.00706 | 0.00755 |
| 5 | 0.00823 | 0.00860 | 0.01057 | 0.00979 |
| 6 | 0 | 0 | 0 | 0 |

CSMCARB interpolated between carbon concentrations using a second order equation curve-fit to the data presented in Table B.6. Figure B.8 shows the transformation strain as a function of carbon concentration for the ferritic, pearlitic, bainitic and martensitic phase transformations. Figure B.9 shows the calculated linear dilatometric strain as a function of temperature for 0.20 and 0.80 weight percent carbon SAE 4620 alloy steels cooled from 871°C to 25°C.

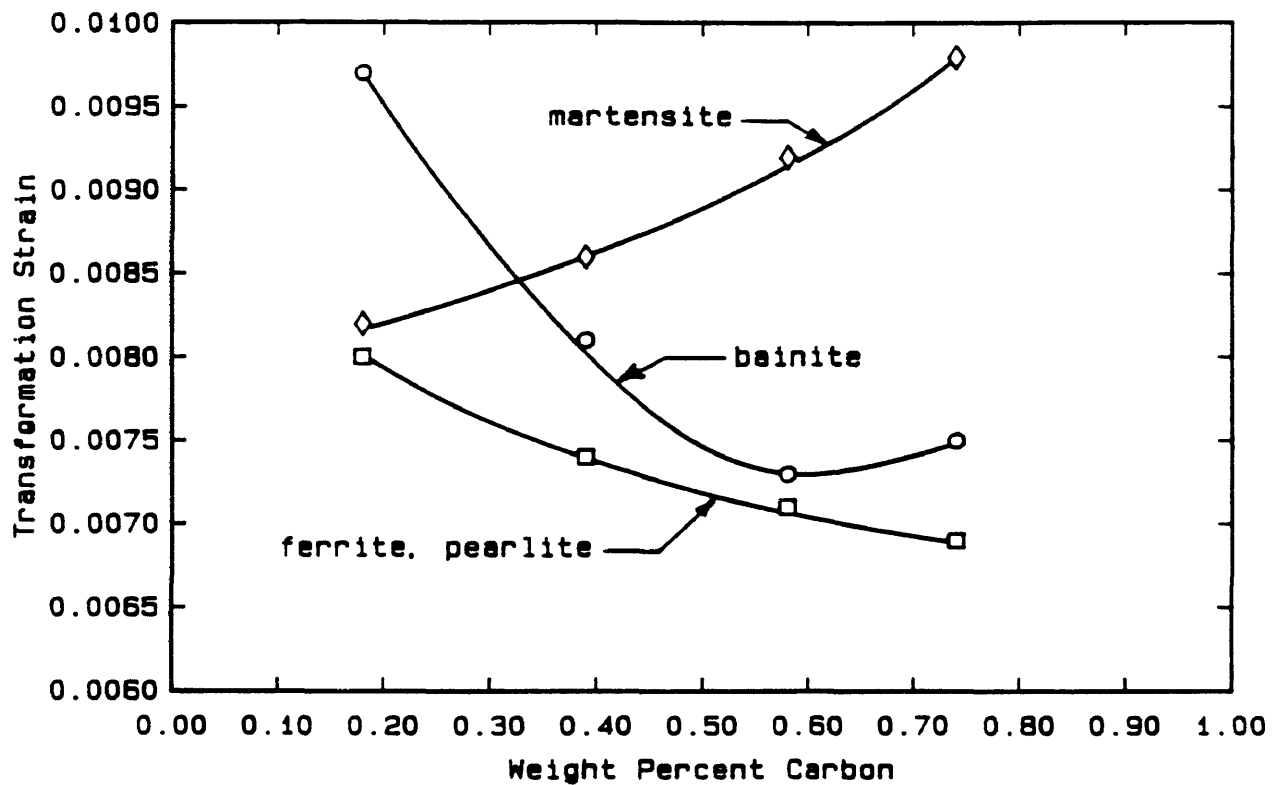


Figure B.8 Transformation strain as a function of carbon concentration for the ferritic, pearlitic, bainitic and martensitic phase transformations (2).

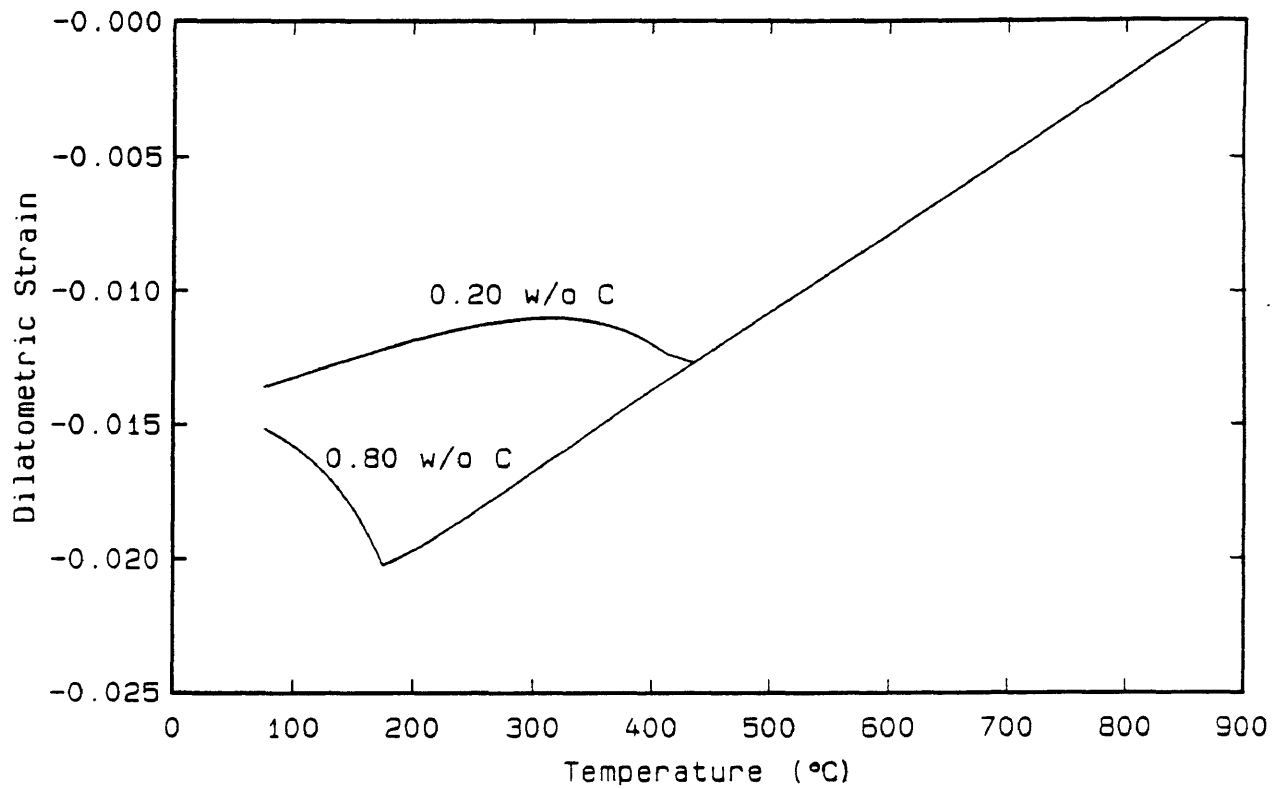


Figure B.9 Calculated dilatometric strain as a function of temperature for 0.20 and 0.80 weight percent carbon SAE 4620 alloy steels cooled from 871°C to 25°C.

10. Elastic Modulus

The elastic modulus as a function of temperature and phase for the SAE 4023 and SAE 4620 alloys is assumed to follow the relationship determined by Burnett (1) and given in Hildenwall (2). This relationship is given by:

$$E = \sum_{i=1}^6 v_i (E_{0,i} + E_{1,i}T + E_{2,i}T^2 + E_{3,i}T^3) \quad (\text{MPa})$$

where T is the temperature in degrees C and E_0 , E_1 , E_2 and E_3 for each phase is given in Table B.7.

Table B.7
Coefficients for Elastic Modulus

| phase | E_0 | E_1 | E_2 (x 10^3) | E_3 (x 10^6) |
|-------|--------|--------|----------------------|----------------------|
| 1 | 198500 | -44.62 | -90.90 | -2.059 |
| 2 | 214500 | -30.97 | -92.08 | -2.797 |
| 3 | 214500 | -30.97 | -92.08 | -2.797 |
| 4 | 214500 | -30.97 | -92.08 | -2.797 |
| 5 | 214500 | -30.97 | -92.08 | -2.797 |
| 6 | 214500 | -30.97 | -92.08 | -2.797 |

Figure B.10 illustrates the elastic modulus, E, as a function of temperature for a 0.23 weight percent SAE 4023 alloy steel transforming from austenite to martensite ($M_s = 415^\circ\text{C}$) beginning at 871°C and continuing to 25°C .

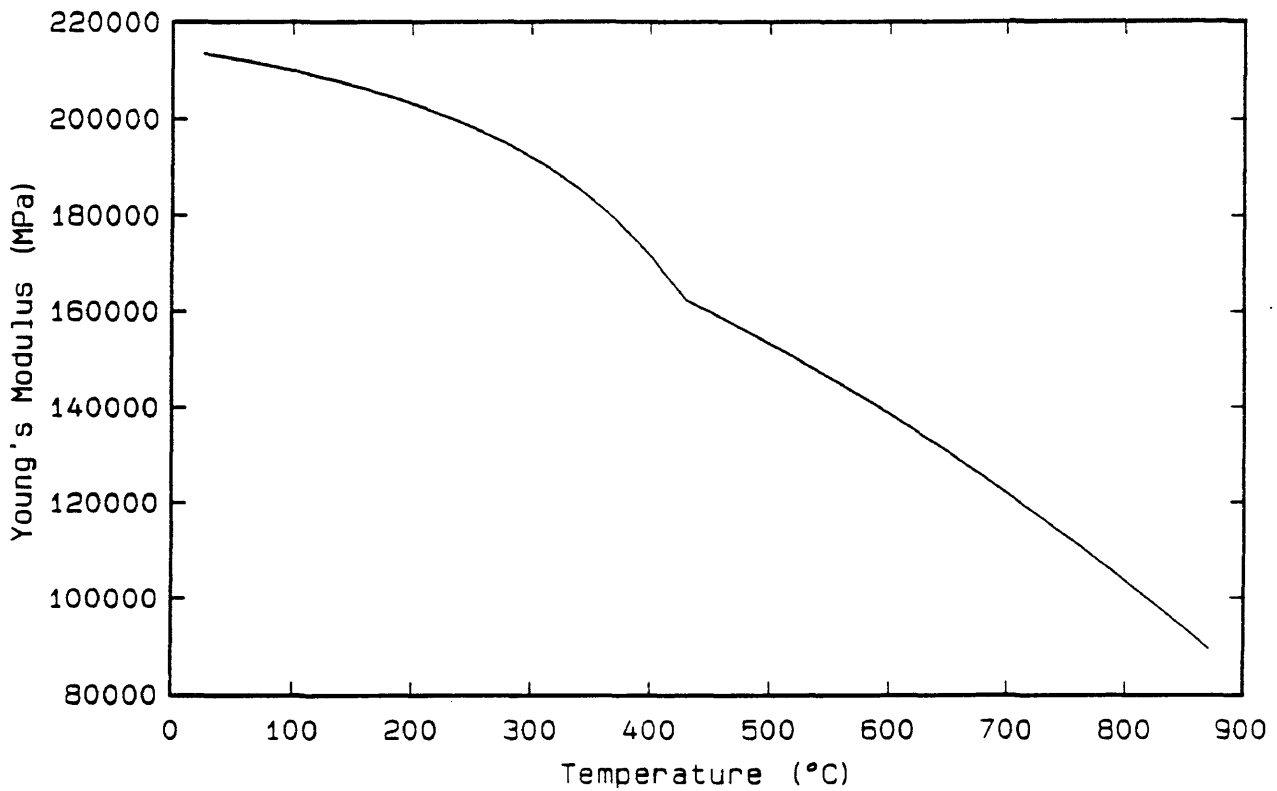


Figure B.10 Elastic modulus, E , as a function of temperature for a 0.23 weight percent SAE 4023 alloy steel transforming from austenite to martensite ($M_s = 415^\circ\text{C}$) beginning at 871°C and continuing to 25°C .

10. Yield Strength

The yield strength as a function of temperature, carbon content, and phase for the SAE 4023 and SAE 4620 alloys is assumed to follow the relationship given in Hildenwall (2). This relationship is given by:

$$S_y = \sum_{i=1}^6 v_i (S_{y_{0,i}} + S_{y_{1,i}}T + S_{y_{2,i}}T^2 + S_{y_{3,i}}T^3) \quad (\text{MPa})$$

where T is the temperature in degrees C and S_{y_0} , S_{y_1} , S_{y_2} and S_{y_3} for each phase is given in Table B.8.

Table B.8
Coefficients for Yield Strength

| phase | carbon content | S_{y_0} | S_{y_1} | S_{y_2} (x 10^6) | S_{y_3} (x 10^9) |
|-------|----------------|-----------|-----------|--------------------------|--------------------------|
| 1 | - | 43.9 | 0.29 | -589.0 | 276.4 |
| 2 | - | 395 | -0.43 | 0 | 0 |
| 3 | - | 461 | -0.23 | 0 | 0 |
| 4 | 0.0 | 480 | -0.5 | 0 | 0 |
| | 0.4 | 890 | -0.5 | 0 | 0 |
| | 0.8 | 1300 | -0.5 | 0 | 0 |
| | 1.2 | 1300 | -0.5 | 0 | 0 |
| 5 | 0.0 | 300 | -0.5 | 0 | 0 |
| | 0.4 | 400 | -0.5 | 0 | 0 |
| | 0.8 | 400 | -0.5 | 0 | 0 |
| | 1.2 | 400 | -0.5 | 0 | 0 |
| 6 | - | 500 | 0 | 0 | 0 |

Linear interpolation was used between the tabulated carbon concentrations. Figure B.11 shows the yield strength, S_y , as a function of temperature for a 0.23 w/o SAE 4023 steel transforming from austenite to martensite ($M_s = 415^\circ\text{C}$).

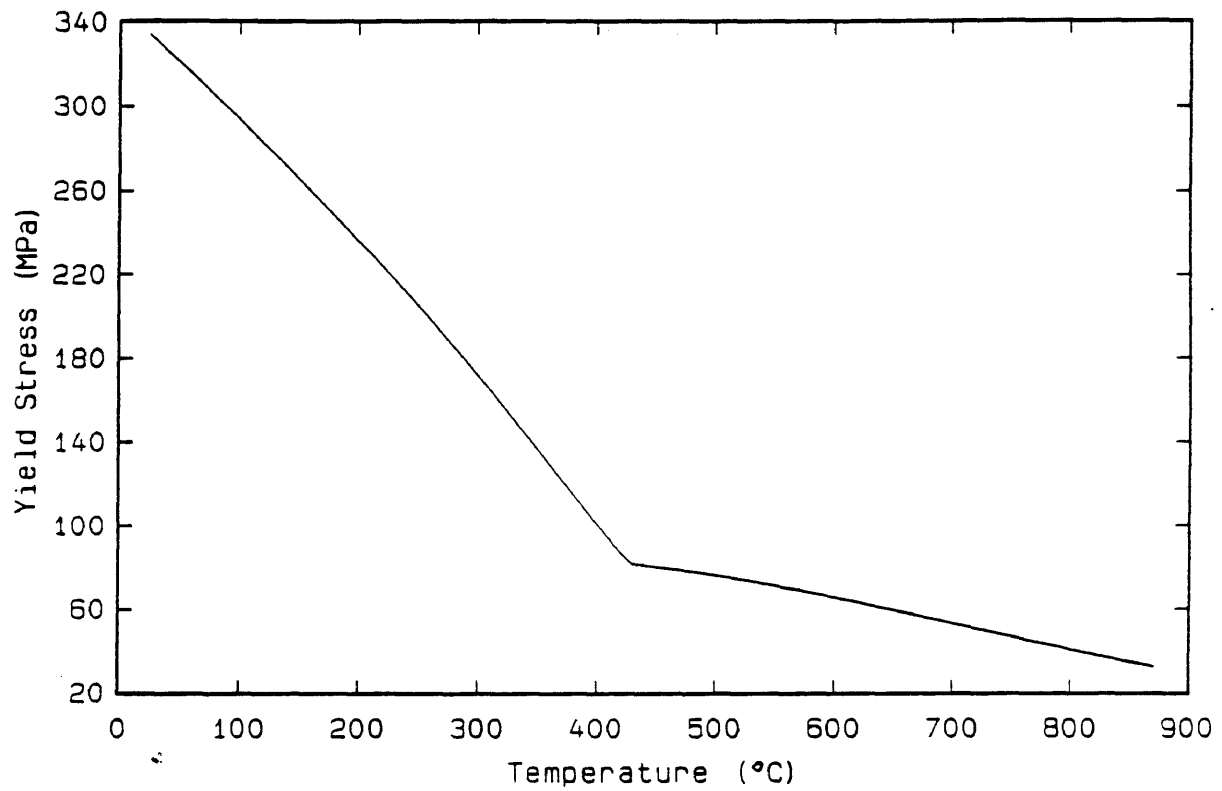


Figure B.11 Yield strength, S_y , as a function of temperature for a 0.23 weight percent SAE 4023 alloy steel transforming from austenite to martensite ($M_s = 415^\circ\text{C}$) beginning at 871°C and continuing to 25°C .

10. The Stress at Four Percent Strain, the Strain Hardening Coefficient and the Tangent Modulus

The strain hardening behavior as a function of temperature, carbon content and phase for the SAE 4023 and SAE 4620 alloys is assumed to follow the relationship given in Hildenwall (2). The relationship for stress at four percent strain is given by:

$$S4 = \sum_{i=1}^6 v_i (S4_{0,i} + S4_{1,i}T + S4_{2,i}T^2 + S4_{3,i}T^3) \quad (\text{MPa})$$

where T is the temperature in degrees C and $S4_0$, $S4_1$, $S4_2$ and $S4_3$ for each phase is given in Table B.9.

Table B.9
Coefficients for Stress at Four Percent Strain

| phase | carbon content | $S4_0$ | $S4_1$ | $S4_2$ ($\times 10^6$) | $S4_3$ ($\times 10^9$) |
|-------|----------------|--------|--------|-----------------------------|-----------------------------|
| 1 | - | 166 | 0.25 | -614 | 240 |
| 2 | - | 395 | -0.032 | 0 | 0 |
| 3 | - | 488 | 4.32 | -11440 | 7200 |
| 4 | 0.0 | 500 | -0.5 | 0 | 0 |
| | 0.4 | 1250 | -0.5 | 0 | 0 |
| | 0.8 | 2050 | -0.5 | 0 | 0 |
| | 1.2 | 2050 | -0.5 | 0 | 0 |
| 5 | 0.0 | 3100 | -0.1 | 0 | 0 |
| | 0.4 | 6980 | -0.1 | 0 | 0 |
| | 0.8 | 7080 | -0.1 | 0 | 0 |
| | 1.2 | 7080 | -0.1 | 0 | 0 |
| 6 | - | 1000 | 0 | 0 | 0 |

Linear interpolation was used between the tabulated carbon concentrations. The elastic modulus, E , yield strength, S_y , and stress at four percent strain, S_4 , are then used to solve for the strain hardening coefficient, H . This relationship is given as:

$$H = \frac{E (S_4 - S_y)}{0.04E - S_4} \quad (\text{MPa})$$

The tangent modulus, E^T , is then determined using the following relationship:

$$E^T = \frac{H E}{(H + E)} \quad (\text{MPa})$$

Figure B.12 shows the stress-strain behavior for a 0.23 w/o SAE 4023 steel transforming from austenite to martensite ($M_s = 415^\circ\text{C}$) at the various indicated temperatures.

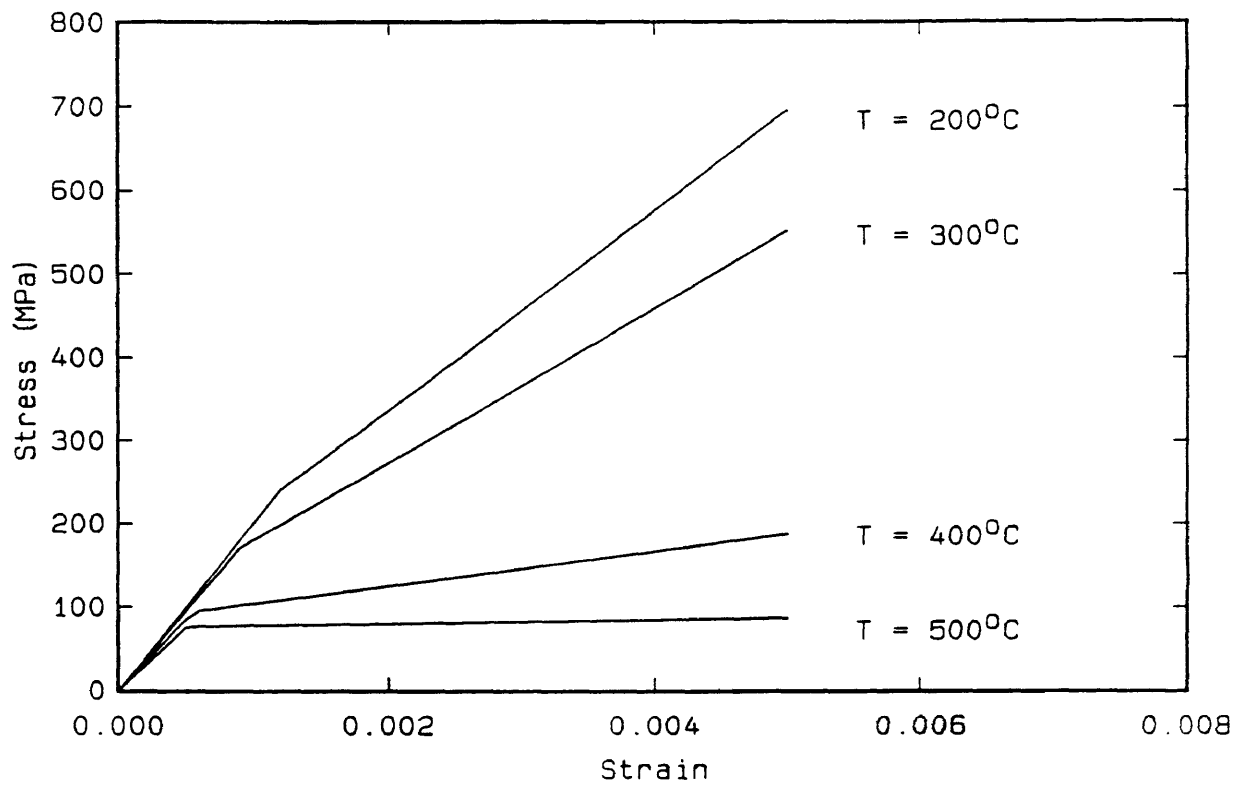


Figure B.12 The stress strain behavior for a 0.23 weight percent SAE 4023 alloy steel transforming from austenite to martensite ($M_s = 415^\circ\text{C}$) at the various indicated temperatures.

APPENDIX C Derivation of An Elastic-Plastic Constitutive Equation with Temperature Effect¹

1. Yield Criterion

The von Mises' yield criterion, assuming isotropic hardening, is incorporated in this analysis. Figure C.1 (21) illustrates geometrically the yield criterion, assuming isotropic hardening and a simple constant tangent modulus, E_T . The yield cylinder shown is oriented such that its axis is at equal angles to the $(\sigma_1, \sigma_2, \sigma_3)$ coordinate system. The cylinder axis therefore represents the hydrostatic component of the stress state. A stress state within the cylinder represents elastic behavior and yielding begins when the stress state reaches the surface of the cylinder. Isotropic hardening allows the radius of the cylinder to vary with effective plastic strain and temperature but does not allow the cylinder axis to vary. Further explanation can be found in (21,24,25,34).

¹ The derivation and implimentation of the elastic-plastic constitutive equation used in this study was a joint effort of Dr. M. Henriksen and D.B. Larson.

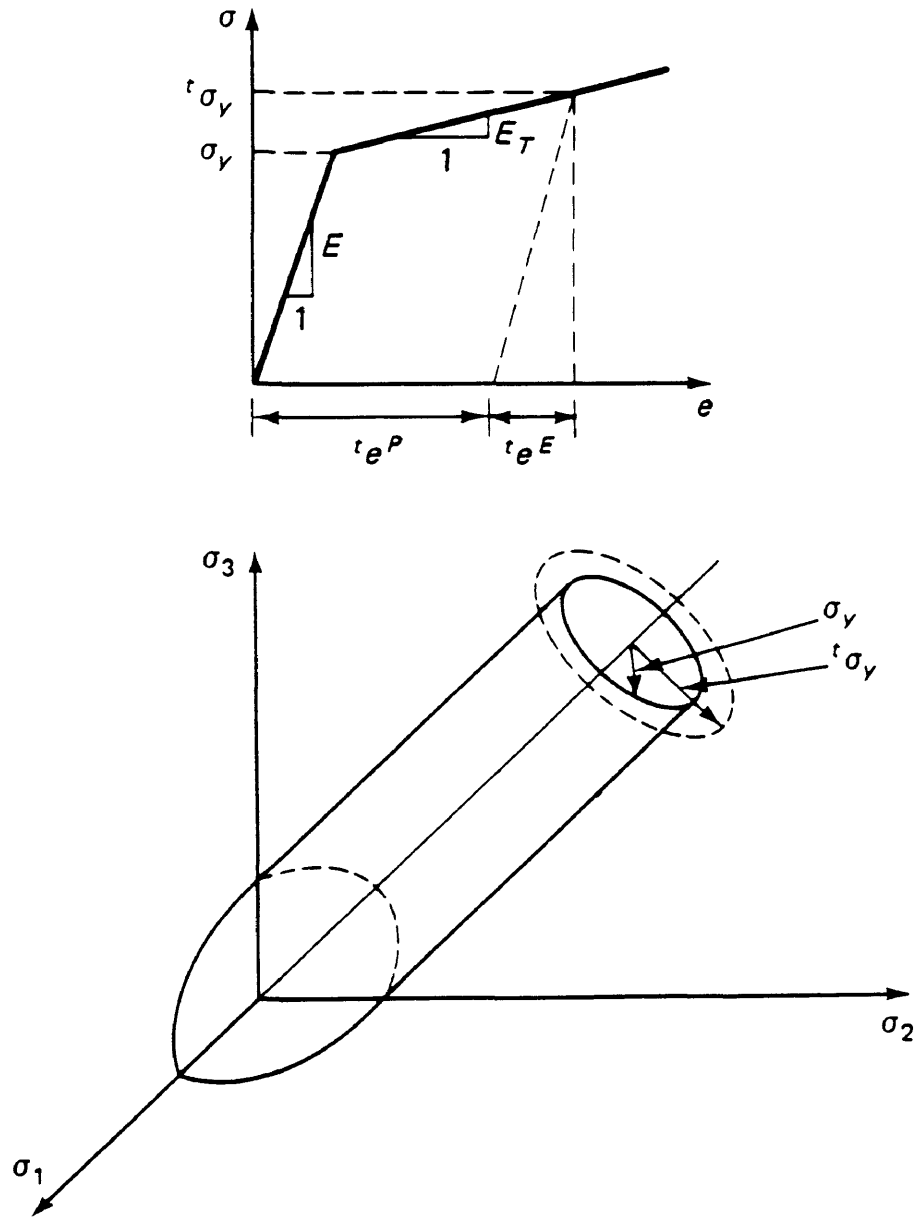


Figure C.1 The von Mises' yield criterion, assuming isotropic hardening, represented geometrically by the yield cylinder (21).

The yield surface can be defined numerically using a function, F , given as:

$$F = \frac{1}{2}\langle \mathbf{s} \rangle \{ \mathbf{s} \} - \frac{1}{3} S_y^2(\bar{\epsilon}, T) = J_2 - \frac{1}{3} S_y^2(\bar{\epsilon}, T) \quad (C.1)$$

where

F = function that describes the yield surface
 $\frac{1}{2}\langle \mathbf{s} \rangle \{ \mathbf{s} \} = J_2$ = second deviatoric stress invariant
 S_y = yield stress
 $\bar{\epsilon}$ = effective plastic strain
 T = temperature

The second deviatoric stress invariant for two-dimensional plane strain conditions is defined as:

$$\begin{aligned} \frac{1}{2}\langle \mathbf{s} \rangle \{ \mathbf{s} \} = J_2 = \frac{1}{6} [& (\tau_{xx} - \tau_{yy})^2 + (\tau_{yy} - \tau_{zz})^2 \\ & + (\tau_{zz} - \tau_{xx})^2] + \tau_{xy}^2 \end{aligned} \quad (C.2)$$

The effective plastic strain, $\bar{\epsilon}$, is defined as:

$$\bar{\epsilon} = \sqrt{\frac{2}{3} \{ (\epsilon_1^{PL})^2 + (\epsilon_2^{PL})^2 + (\epsilon_3^{PL})^2 \}} \quad (C.3)$$

where the strains in (C.3) are the principle strains.

2. Flow Rule

The Prandtl-Reuss flow rule incorporates a constant of proportionality, λ , that relates the deviatoric stress components to the incremental plastic strain components.

This is given as:

$$\{\Delta \epsilon^{PL}\} = \lambda \left\{ \frac{\partial F}{\partial \tau} \right\} = \lambda \{s\} \quad (C.4)$$

where

$\{\Delta \epsilon^{PL}\}$ = incremental plastic strain components
 λ = constant of proportionality (to be determined)
 F = yield function
 τ = stress
 $\{s\}$ = deviatoric stress components

3. Consistency Rule

During plastic deformation, the yield function, F , is zero. Therefore the total derivative of the yield function must also be zero. The consistency rule, given as the total derivative of the yield function, F , is given by:

$$\Delta F = 0 = \langle s \rangle \{\Delta \tau\} - \frac{2}{3} S_y (H \Delta \tilde{\epsilon} + \beta \Delta T) \quad (C.5)$$

where H and β are defined as:

$$H = \frac{\partial S_y}{\partial \tilde{\epsilon}} \quad \beta = \frac{\partial S_y}{\partial T} \quad (C.6)$$

4. Strain Decomposition

The incremental kinematic strain, $\{\Delta\epsilon^K\}$, can be written as the sum of the elastic, plastic, thermal and phase transformation incremental strains, as follows:

$$\{\Delta\epsilon^K\} = \{\Delta\epsilon^{EL}\} + \{\Delta\epsilon^{PL}\} + \{\Delta\epsilon^\theta\} + \{\Delta\epsilon^\phi\} \quad (C.7)$$

The incremental thermal strains, $\{\Delta\epsilon^\theta\}$, from time t to time $t+\Delta t$ are given by the coefficient of thermal expansion, α , and the incremental change in temperature. This relationship is given by:

$$\{\Delta\epsilon^\theta\} = \begin{Bmatrix} \Delta\epsilon_{xx}^\theta \\ \Delta\epsilon_{yy}^\theta \\ \Delta\epsilon_{xy}^\theta \\ \Delta\epsilon_{zz}^\theta \end{Bmatrix} = \begin{Bmatrix} \alpha^{t+\Delta t}\mathbf{T}^{t+\Delta t} - \alpha^t\mathbf{T}^t \\ \alpha^{t+\Delta t}\mathbf{T}^{t+\Delta t} - \alpha^t\mathbf{T}^t \\ 0 \\ \alpha^{t+\Delta t}\mathbf{T}^{t+\Delta t} - \alpha^t\mathbf{T}^t \end{Bmatrix} \quad (C.8)$$

The incremental phase transformation strains, $\{\Delta\epsilon^\phi\}$, from time t to time $t+\Delta t$ are determined using experimental data given in Appendix B. This relationship is given by:

$$\{\Delta\epsilon^\phi\} = \begin{Bmatrix} \Delta\epsilon_{xx}^\phi \\ \Delta\epsilon_{yy}^\phi \\ \Delta\epsilon_{xy}^\phi \\ \Delta\epsilon_{zz}^\phi \end{Bmatrix} = \begin{Bmatrix} e^{\phi^{t+\Delta t}} - e^{\phi^t} \\ e^{\phi^{t+\Delta t}} - e^{\phi^t} \\ 0 \\ e^{\phi^{t+\Delta t}} - e^{\phi^t} \end{Bmatrix} \quad (C.9)$$

5. Elastic Constitutive Relationship

The elastic constitutive relationship for a system where the elastic modulus, $E(T)$, is a function of temperature, T , is given by:

$$\{\Delta\tau^{t+\Delta t}\} = [D]\{\Delta e^{EL}\} + [\dot{D}]\{e^{EL^t} + \Delta e^{EL}\} \quad (C.10)$$

$$[\dot{D}] = \frac{\partial E}{\partial T} [D] \Delta T$$

where $\{e^{EL^t}\}$ is the historical elastic strain (i.e. the total elastic strain at time t).

The elastic plane strain constitutive matrix, $[D]$, is defined as:

$$[D] = \frac{E(1-\nu)}{(1+\nu)(1-2\nu)} \begin{bmatrix} 1 & \frac{\nu}{(1-\nu)} & 0 \\ \frac{\nu}{(1-\nu)} & 1 & 0 \\ 0 & 0 & \frac{(1-2\nu)}{2(1-\nu)} \end{bmatrix} \quad (C.11)$$

where

$$E = f(T)$$

6. Derivation of the Elastic Constitutive Equation

For an elastic system (i.e. $\Delta\varepsilon^{PL}$ and ε^{PL} are zero) undergoing a temperature change, ΔT , from time t to time $t+\Delta t$, the new incremental stress, $\{\Delta\tau\}$, is given by:

$$\begin{aligned} \{\Delta\tau\} &= [D]\{\Delta e^{\kappa} - \Delta e^{\theta} - \Delta e^{\phi}\} \\ &+ [\dot{D}]\{\Delta e^{\kappa} - \Delta e^{\theta} - \Delta e^{\phi}\} \\ &+ [\dot{D}]\{e^{\kappa^t} - e^{\theta^t} - e^{\phi^t}\} \end{aligned} \quad (C.12)$$

By defining a new constitutive matrix, $[D^*]$, and historical elastic strain, $\{e^{EL^t}\}$, as follows:

$$\begin{aligned} [D^*] &= [D] + [\dot{D}] \\ \{e^{EL^t}\} &= \{e^{\kappa^t} - e^{\theta^t} - e^{\phi^t}\} \end{aligned} \quad (C.13)$$

The elastic constitutive equation in (C.12) can be rewritten as:

$$\{\Delta\tau\} = [D^*]\{\Delta e^{\kappa} - \Delta e^{\theta} - \Delta e^{\phi}\} + [\dot{D}]\{e^{EL^t}\} \quad (C.14)$$

7. Deviation of the Elastic-Plastic Constitutive Equation

For an elastic-plastic system undergoing a temperature change, ΔT , from time t to time $t+\Delta t$, the new incremental stress, $\{\Delta\tau\}$, is given by:

$$\begin{aligned} \{\Delta\tau\} &= [D^*]\{\Delta e^K - \Delta e^{PL} - \Delta e^\theta - \Delta e^\phi\} \\ &+ [\dot{D}]\{e^{EL^t}\} \end{aligned} \quad (C.15)$$

During plastic flow, the yield function, F , is zero. The consistency rule, (C.5), and (C.15) can be written as:

$$\begin{aligned} \langle s \rangle \{\Delta\tau\} &= \frac{2}{3} S_y (H \Delta \tilde{\epsilon} + \beta \Delta T) \\ &= \langle s \rangle [D^*] \{\Delta e^K - \Delta e^{PL} - \Delta e^\theta - \Delta e^\phi\} \\ &+ \langle s \rangle [\dot{D}] \{e^{EL^t}\} \end{aligned} \quad (C.16)$$

The plastic work in the system, incorporating the flow rule in (C.4), can be written as:

$$\langle \tau \rangle \{\Delta e^{PL}\} = \lambda \langle \tau \rangle \{s\} = S_y \Delta \tilde{\epsilon} \quad (C.17)$$

From (C.17), the constant of proportionality, λ , and the incremental plastic strain, $\{\Delta e^{PL}\}$, can be found as:

$$\begin{aligned} \lambda &= \frac{S_y \Delta \tilde{\epsilon}}{\langle s \rangle \langle \tau \rangle} \\ \{\Delta e^{PL}\} &= \lambda \{s\} = \frac{S_y \Delta \tilde{\epsilon}}{\langle s \rangle \langle \tau \rangle} \{s\} \end{aligned} \quad (C.18)$$

Equations (C.16) and (C.18) can be combined to yield the following relationship:

$$\begin{aligned} \frac{2}{3} \mathbf{S}_y \mathbf{H} \Delta \tilde{\mathbf{e}} + \frac{\langle \mathbf{s} \rangle [\mathbf{D}^*] \{ \mathbf{s} \}}{\langle \mathbf{s} \rangle \{ \boldsymbol{\tau} \}} \mathbf{S}_y \Delta \tilde{\mathbf{e}} &= \Gamma \mathbf{S}_y \Delta \tilde{\mathbf{e}} \\ &= \langle \mathbf{s} \rangle [\mathbf{D}^*] \{ \Delta \mathbf{e}^{\kappa} - \Delta \mathbf{e}^{\theta} - \Delta \mathbf{e}^{\phi} \} \\ &\quad - \frac{2}{3} \mathbf{S}_y \boldsymbol{\beta} \Delta \mathbf{T} + \langle \mathbf{s} \rangle [\mathbf{D}] \{ \mathbf{e}^{\text{EL}^t} \} \end{aligned} \quad (\text{C.19})$$

where Γ is defined as:

$$\Gamma = \left[\frac{2}{3} \mathbf{H} + \frac{\langle \mathbf{s} \rangle [\mathbf{D}^*] \{ \mathbf{s} \}}{\langle \mathbf{s} \rangle \{ \boldsymbol{\tau} \}} \right] \quad (\text{C.20})$$

Equation (C.19) can now be written as follows:

$$\begin{aligned} \mathbf{S}_y \Delta \tilde{\mathbf{e}} &= \frac{1}{\Gamma} (\langle \mathbf{s} \rangle [\mathbf{D}^*] \{ \Delta \mathbf{e}^{\kappa} - \Delta \mathbf{e}^{\theta} - \Delta \mathbf{e}^{\phi} \} \\ &\quad - \frac{2}{3} \mathbf{S}_y \boldsymbol{\beta} \Delta \mathbf{T} + \langle \mathbf{s} \rangle [\mathbf{D}] \{ \mathbf{e}^{\text{EL}^t} \}) \end{aligned} \quad (\text{C.21})$$

The effective incremental plastic strain can then be found using the following equation:

$$\begin{aligned} \Delta \tilde{\mathbf{e}} &= \frac{1}{\Gamma \mathbf{S}_y} (\langle \mathbf{s} \rangle [\mathbf{D}^*] \{ \Delta \mathbf{e}^{\kappa} - \Delta \mathbf{e}^{\theta} - \Delta \mathbf{e}^{\phi} \} \\ &\quad - \frac{2}{3} \mathbf{S}_y \boldsymbol{\beta} \Delta \mathbf{T} + \langle \mathbf{s} \rangle [\mathbf{D}] \{ \mathbf{e}^{\text{EL}^t} \}) \end{aligned} \quad (\text{C.22})$$

The incremental plastic strain, $\{\Delta\epsilon^{PL}\}$, is then found by first solving for λ , as described in (C.18). By substituting the resulting incremental plastic strain, $\{\Delta\epsilon^{PL}\}$, into (C.15) the following relationship for incremental stress, $\{\Delta\tau\}$, is obtained:

$$\begin{aligned}
 \{\Delta\tau\} &= [D^*]\{\Delta e^k - \Delta e^\theta - \Delta e^\phi\} \\
 &- \frac{[D^*]\{s\}\langle s \rangle [D^*]}{\Gamma\langle s \rangle\langle \tau \rangle} \{\Delta e^k - \Delta e^\theta - \Delta e^\phi\} \\
 &+ \frac{\frac{2}{3} [D^*]\{s\}s_y \beta}{\Gamma\langle s \rangle\langle \tau \rangle} \Delta T \\
 &+ [\acute{D}]\{e^{EL^t}\} - \frac{[D^*]\{s\}\langle s \rangle [\acute{D}]}{\Gamma\langle s \rangle\langle \tau \rangle} \{e^{EL^t}\}
 \end{aligned} \tag{C.23}$$

By defining the following three new terms:

$$\begin{aligned}
 [\bar{D}] &= [D^*] - \frac{[D^*]\{s\}\langle s \rangle[D^*]}{\Gamma\langle s \rangle\{\tau\}} \\
 \{G\} &= \frac{\frac{2}{3}[D^*]\{s\}s_y\beta}{\Gamma\langle s \rangle\{\tau\}} \\
 [\tilde{D}] &= [D] - \frac{[D^*]\{s\}\langle s \rangle[D]}{\Gamma\langle s \rangle\{\tau\}}
 \end{aligned}
 \tag{C.24}$$

the elastic-plastic constitutive equation in (C.23) can be expressed as:

$$\begin{aligned}
 \{\Delta\tau\} &= [\bar{D}]\{\Delta e^x - \Delta e^\theta - \Delta e^\phi\} \\
 &+ \{G\}\Delta T + [\tilde{D}]\{e^{EL^c}\}
 \end{aligned}
 \tag{C.25}$$

The equation expressed in (C.25) is unlike that of previous investigators (1,2,3). It allows for varying elastic modulus with temperature, proper elastic-plastic and plastic-elastic transitional behavior with changing temperature, and plastic creep due to a decrease in yield strength which is useful when considering transformation plasticity (7,30).

APPENDIX D Verification Problems using CSMCARB

Numerous verification problems were developed to determine the viability of the constitutive equation used in this analysis. Verifications were performed using one-dimensional plane stress axial and cantilever load models consisting of four 8-noded isoparametric elements and a two-dimensional plane strain thick wall pressure vessel model consisting of twelve 8-noded isoparametric elements. Figure D.1 illustrates the axial load model used. The cantilever model is identical to that illustrated in Figure D.1 except loading is distributed over the right end nodes in the negative Y direction. Figure D.2 illustrates the thick wall pressure vessel model (24). Following are descriptions of selected verification problems performed.

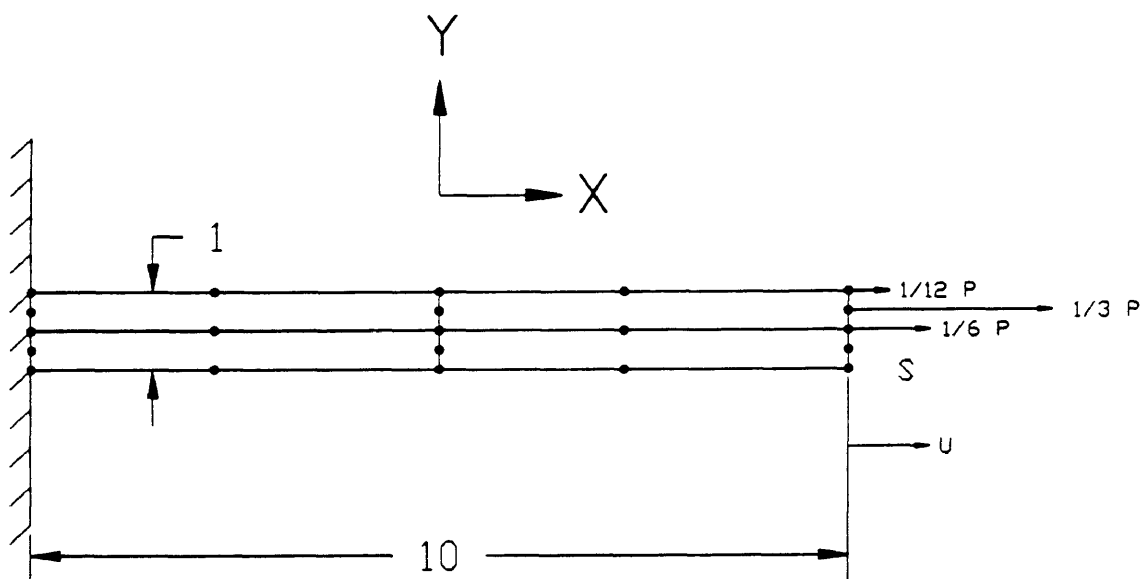


Figure D.1 Schematic illustrating the axial load model used to verify the constitutive equation in CSMCARB.

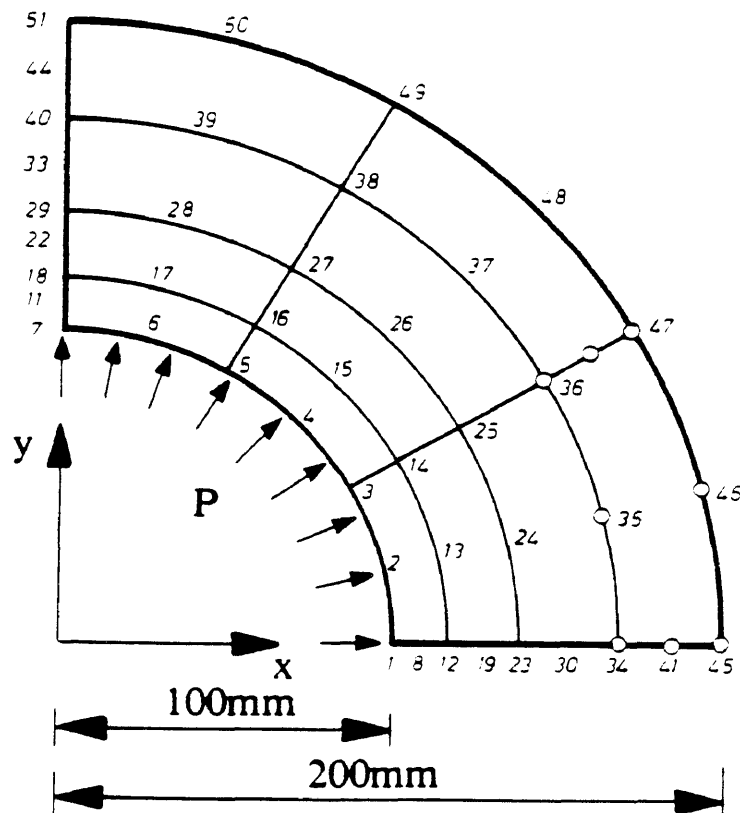


Figure D.2 Schematic illustrating the thick wall pressure vessel model used to verify the constitutive equation in CSMCARB (24).

VERIFICATION PROBLEM #1

Description:

One-dimensional plane stress elastic analysis with external tensile load. The temperature is held constant at zero.

$$\begin{aligned}
 E &= 10 \times 10^6 \\
 E_T &= n/a \\
 S_y &= 10 \times 10^3 \text{ (constant)} \\
 \nu &= 0.30 \\
 \alpha &= 0
 \end{aligned}$$

Results:

| P | T | τ_{xx} | $\epsilon_{xx} \times 10^3$ |
|------|---|-------------|-----------------------------|
| 2000 | 0 | 2000 | 0.2 |
| 4000 | 0 | 4000 | 0.4 |
| 6000 | 0 | 6000 | 0.6 |
| 8000 | 0 | 8000 | 0.8 |

Discussion:

The calculated results using CSMCARB agree with the closed-form solutions for axial stress and strain to 12 significant digits. A stress-strain diagram and the applied loads for verification problem #1 is illustrated in Figure D.3.

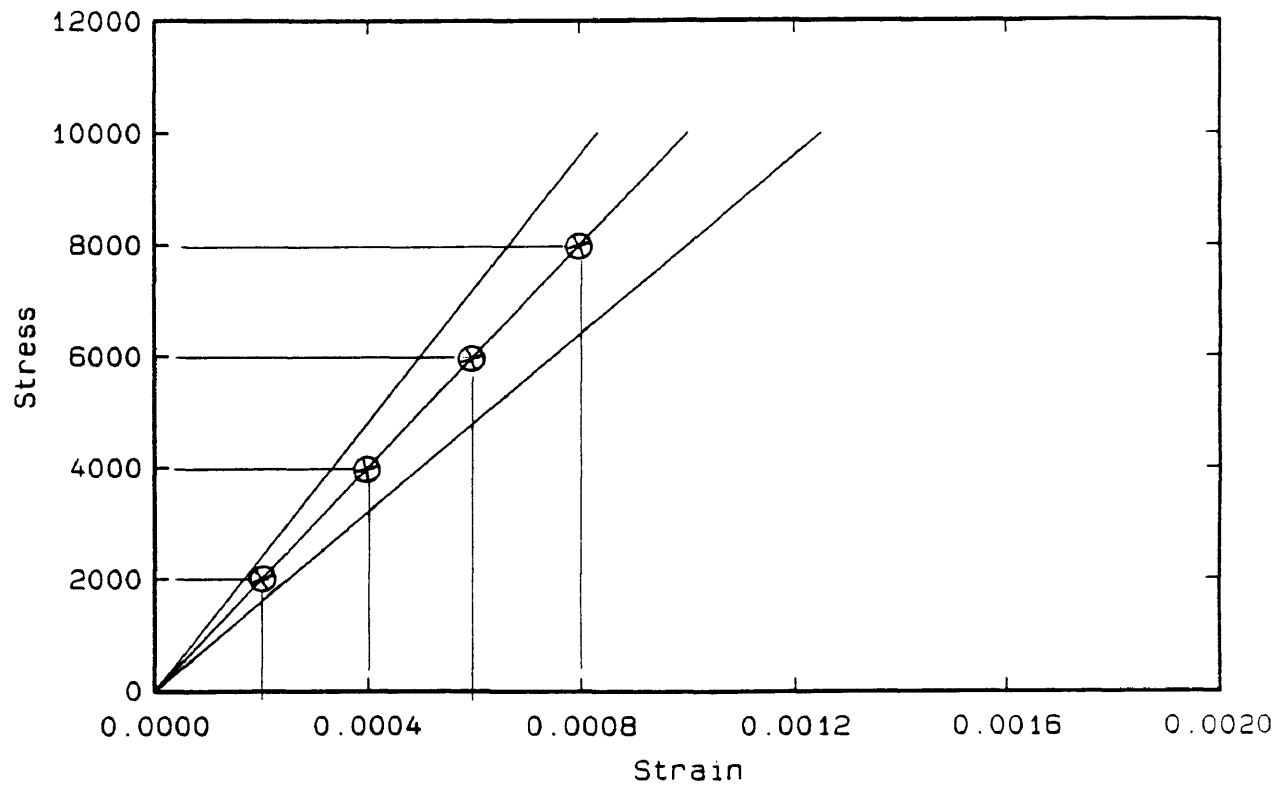


Figure D.3 Stress-strain diagram and the applied loads for verification problem #1.

VERIFICATION PROBLEM #2

Description:

One-dimensional plane stress elastic analysis with varying elastic modulus and temperature. An external load is incrementally applied, then held constant while the temperature is varied.

$$E = (10 \times 10^6)(1 - 0.2T)$$

$$E_T = n/a$$

$$S_y = 10 \times 10^3 \text{ (constant)}$$

$$\nu = 0.30$$

$$\alpha = 1 \times 10^{-3}$$

Results:

| P | T | τ_{xx} | $\epsilon_{xx} \times 10^3$ |
|------|----|-------------|-----------------------------|
| 2000 | 0 | 2000 | 0.2 |
| 4000 | 0 | 4000 | 0.4 |
| 6000 | 0 | 6000 | 0.6 |
| 8000 | 0 | 8000 | 0.8 |
| 8000 | 1 | 8000 | 2.0 |
| 8000 | 1 | 8000 | 0.8 |
| 8000 | -1 | 8000 | -0.333 |
| 8000 | 0 | 8000 | 0.8 |

Discussion:

The combination of varying elastic modulus and thermal strain due to the temperature change produced the correct change in the elastic strain. The calculated results using CSMCARB agree with the closed-form solutions to 12 significant digits. A stress-strain diagram and the applied loads for verification problem #2 is illustrated in Figure D.4.

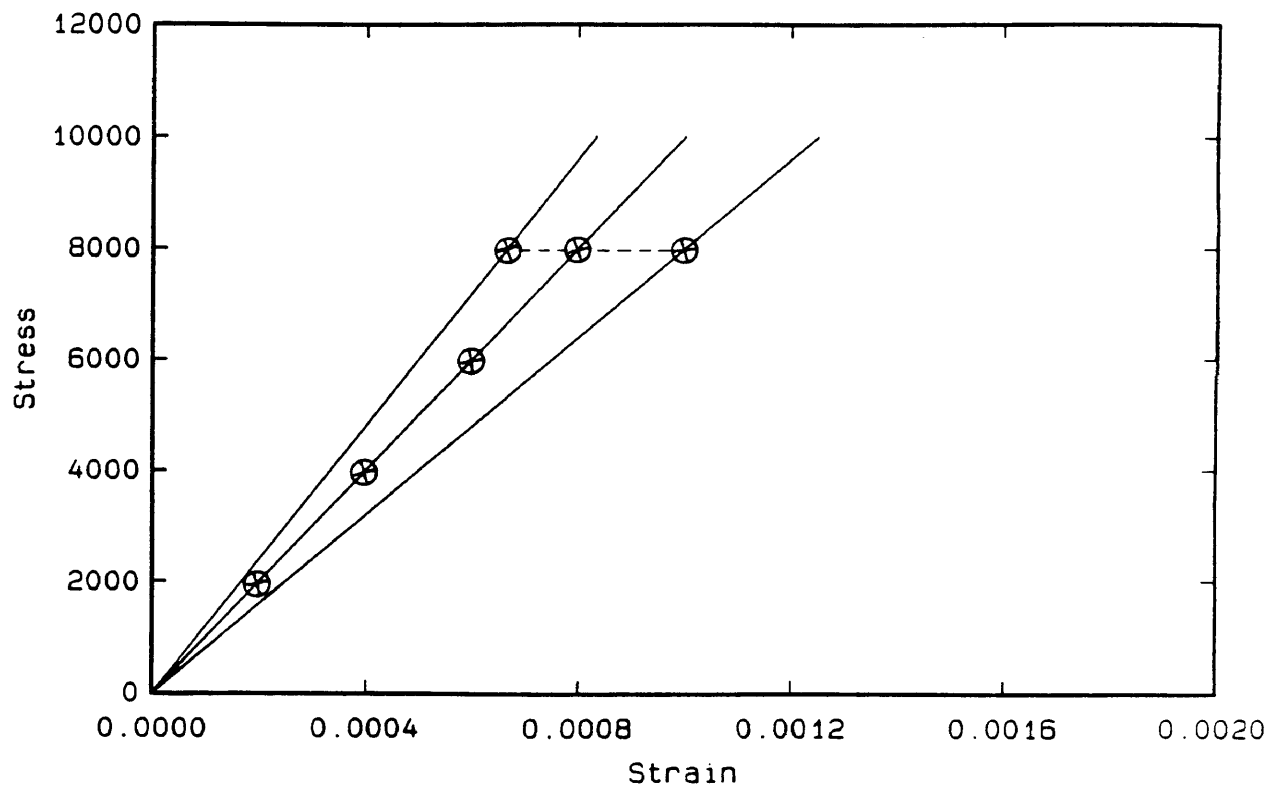


Figure D.4 Stress-strain diagram and the applied loads for verification problem #2.

VERIFICATION PROBLEM #3

Description:

One-dimensional plane stress elastic-plastic analysis with axial load. The temperature is held constant at zero. External load is applied near the yield point.

$$\begin{aligned}
 E &= 10 \times 10^6 \\
 E_T &= 1 \times 10^6 \\
 S_Y &= 10 \times 10^3 \text{ (constant)} \\
 \nu &= 0.30 \\
 \alpha &= 0
 \end{aligned}$$

Results:

| P | T | τ_{xx} | $\epsilon_{xx} \times 10^3$ |
|-----------|---|-------------|-----------------------------|
| 8000 | 0 | 8000 | 0.8 |
| 10000.001 | 0 | 10000.001 | 1.001 |
| 11000 | 0 | 11000 | 2.0 |
| 14000 | 0 | 14000 | 5.0 |

Discussion:

Load exactly yield produces a point of numerical instability. Therefore a load slightly higher than the yield strength is applied. The calculated solutions using CSMCARB agree with the closed-form solutions for axial stress and strain to 4 significant digits. A stress-strain diagram and the applied loads for verification problem #3 is illustrated in Figure D.5.

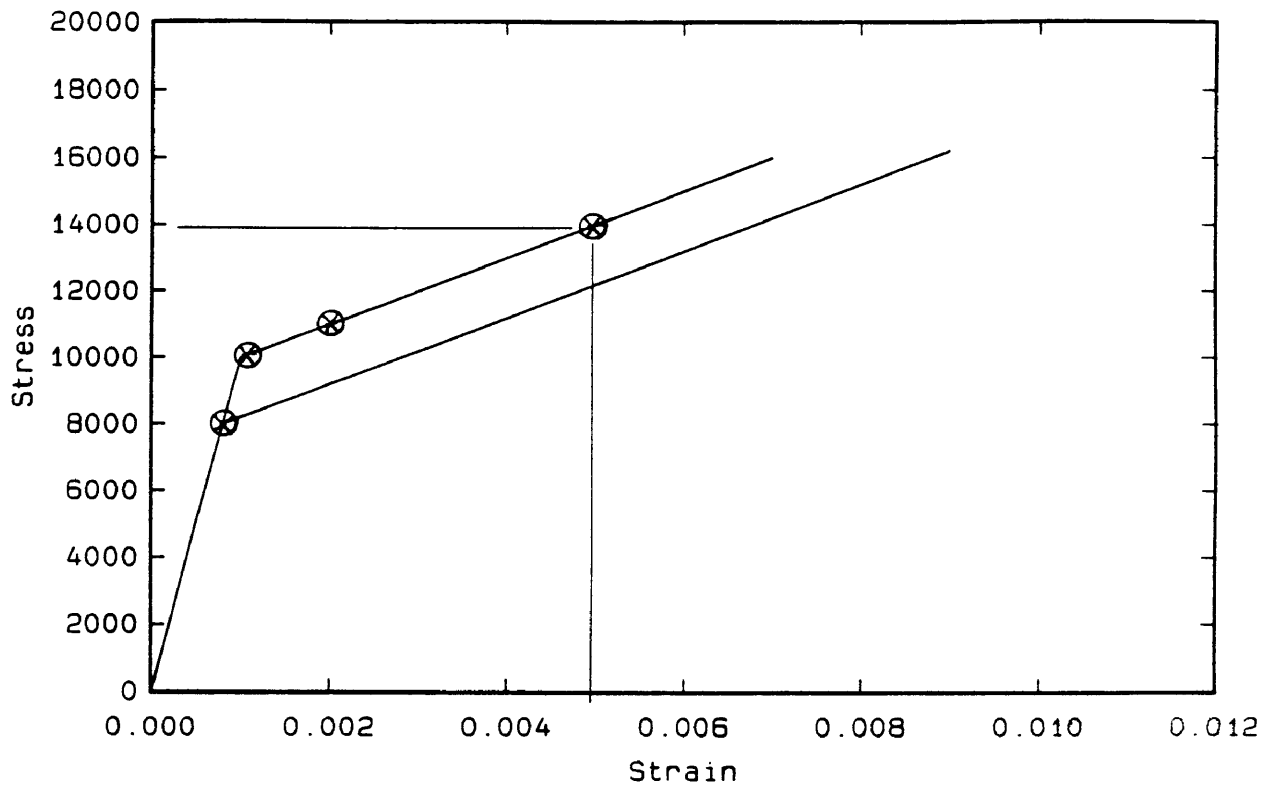


Figure D.5 Stress-strain diagram and the applied loads for verification problem #3.

VERIFICATION PROBLEM #4

Description:

One-dimensional plane stress elastic-plastic analysis with axial load. The temperature is held constant at zero. Loading is applied such that the stress state jumps over the yield strength.

$$\begin{aligned}
 E &= 10 \times 10^6 \\
 E_T &= 1 \times 10^6 \\
 S_y &= 10 \times 10^3 \text{ (constant)} \\
 \nu &= 0.30 \\
 \alpha &= 0
 \end{aligned}$$

Results:

| P | T | τ_{xx} | $\epsilon_{xx} \times 10^3$ |
|-------|---|-------------|-----------------------------|
| 8000 | 0 | 8000 | 0.8 |
| 11000 | 0 | 11000 | 2.0 |
| 14000 | 0 | 14000 | 5.0 |

Discussion:

The correct elastic-to-plastic transitional behavior is observed. The calculated results using CSMCARB agree with the closed-form solutions for axial stress and strain to 4 significant digits. A stress-strain diagram and the applied loads for verification problem #4 is illustrated in Figure D.6.

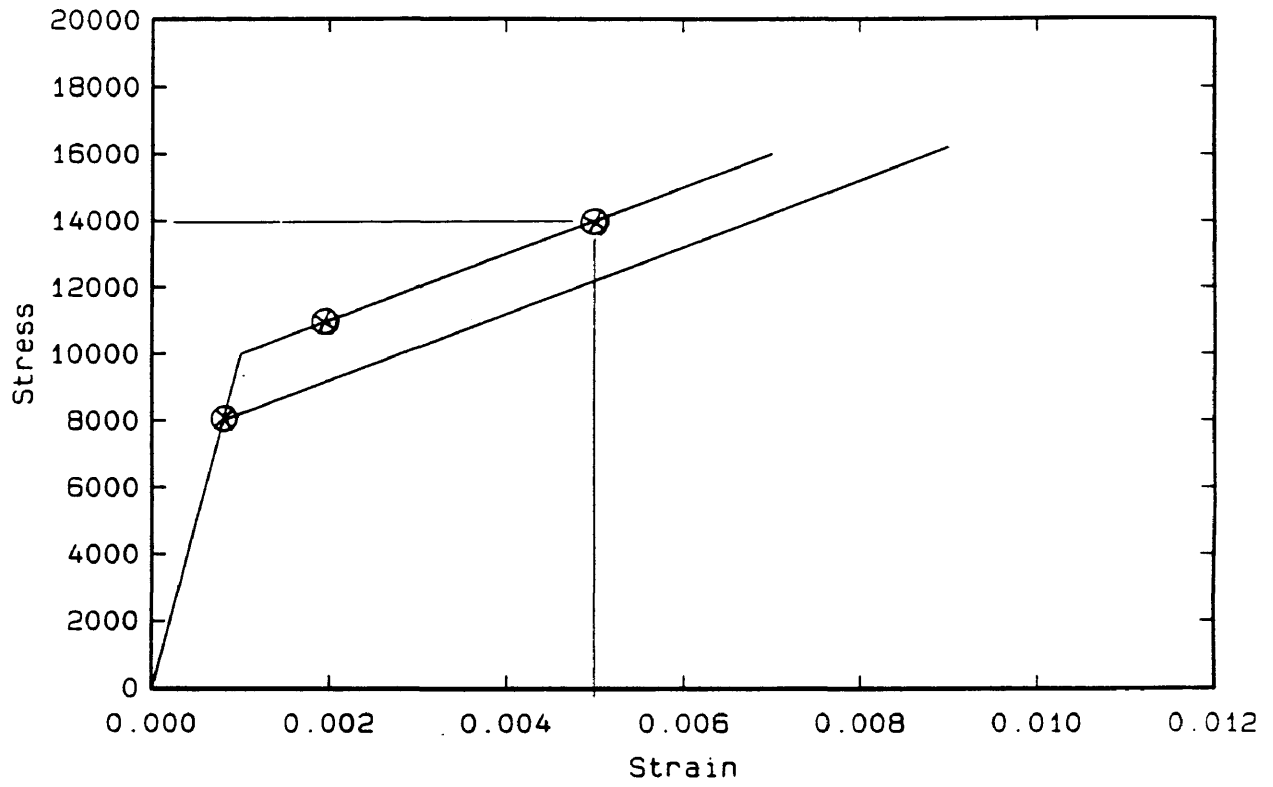


Figure D.6 Stress-strain diagram and the applied loads for verification problem #4.

VERIFICATION PROBLEM #5

Description:

One-dimensional plane stress elastic-plastic analysis with axial load. The temperature is held constant at zero. Applied loads are the same as problem #4. The load is removed to check permanent plastic strain.

$$\begin{aligned}
 E &= 10 \times 10^6 \\
 E_T &= 1 \times 10^6 \\
 S_y &= 10 \times 10^3 \text{ (constant)} \\
 \nu &= 0.30 \\
 \alpha &= 0
 \end{aligned}$$

Results:

| P | T | τ_{xx} | $\epsilon_{xx} \times 10^3$ |
|-------|---|-------------|-----------------------------|
| 8000 | 0 | 8000 | 0.8 |
| 11000 | 0 | 11000 | 2.0 |
| 14000 | 0 | 14000 | 5.0 |
| 0 | 0 | 0 | 3.6 |

Discussion:

CSMCARB correctly calculated the permanent plastic strain at loads of 14000 and 0. The calculated results using CSMCARB agree with the closed-form solutions for axial stress and strain to 4 significant digits. A stress-strain diagram and the applied loads for verification problem #5 is illustrated in Figure D.7.

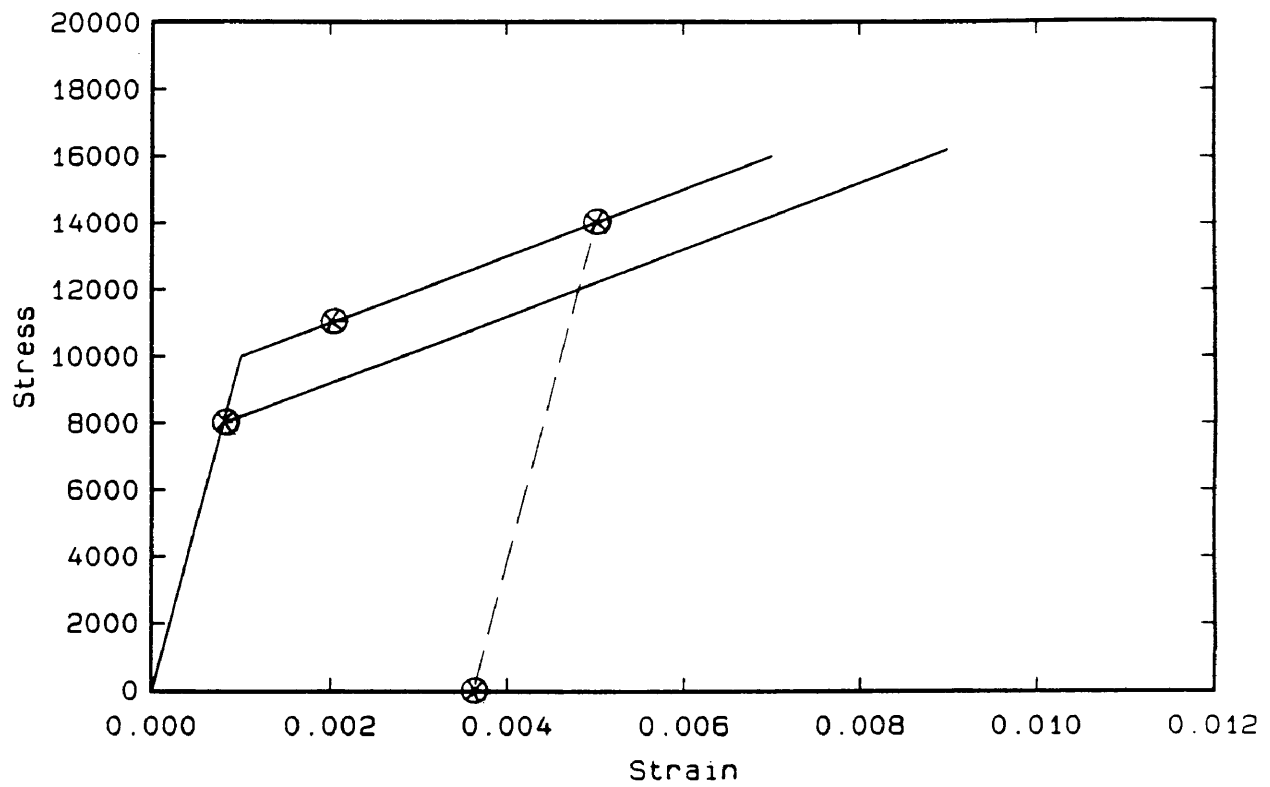


Figure D.7 Stress-strain diagram and the applied loads for verification problem #5.

VERIFICATION PROBLEM #6

Description:

One-dimensional plane stress elastic-plastic analysis with axial load. The temperature is increased (decrease S_y) and the model is allowed to plastically "creep", then unload. The thermal expansion due to temperature increase is ignored.

$$\begin{aligned}
 E &= 10 \times 10^6 \\
 E_T &= 1 \times 10^6 \\
 S_T &= (10 \times 10^3)(1 - 0.2T) \\
 \nu_y &= 0.30 \\
 \alpha &= 0
 \end{aligned}$$

Results:

| P | T | τ_{xx} | $\epsilon_{xx} \times 10^3$ |
|-------|---|-------------|-----------------------------|
| 8000 | 0 | 8000 | 0.8 |
| 11000 | 0 | 11000 | 2.0 |
| 14000 | 0 | 14000 | 5.0 |
| 14000 | 1 | 14000 | 6.8 |
| 0 | 1 | 0 | 5.4 |

Discussion:

Changing S_y by 20% in one step produces numerical instability. Intermediate load steps are therefore needed for numerical stability during "creep" (i.e. $T=0.1$, $T=0.2$, etc.). The calculated results using CSMCARB agree with the closed-form solutions for axial stress and strain to 4 significant digits. A stress-strain diagram and the applied loads for verification problem #6 is illustrated in Figure D.8.

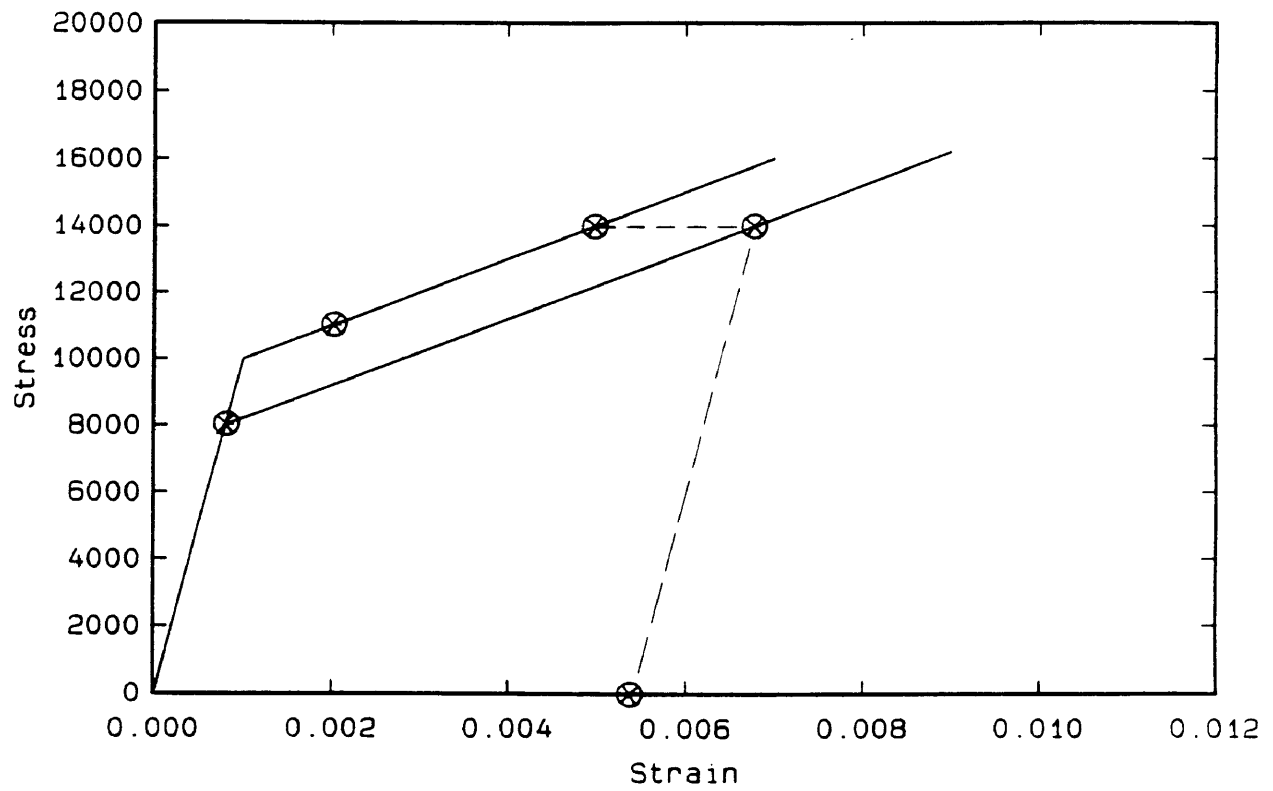


Figure D.8 Stress-strain diagram and the applied loads for verification problem #6.

VERIFICATION PROBLEM #7

Description:

One-dimensional plane stress elastic-plastic analysis with axial load. The temperature is decreased (increase S_y) while holding the load constant and the model is allowed to transition to an elastic state. The load is then increased and the model is allowed to re-transition to plastic behavior. The contraction due to the temperature decrease is included.

$$\begin{aligned}
 E &= 10 \times 10^6 \\
 E_T &= 1 \times 10^6 \\
 S_T &= (10 \times 10^3)(1 - 0.2T) \\
 \nu &= 0.30 \\
 \alpha &= 2 \times 10^{-3}
 \end{aligned}$$

Results:

| P | T | τ_{xx} | $\epsilon_{xx} \times 10^3$ |
|-------|---|-------------|-----------------------------|
| 6000 | 1 | 6000 | 0.6 |
| 11000 | 1 | 11000 | 3.8 |
| 11000 | 0 | 11000 | 1.8 |
| 14000 | 0 | 14000 | 3.0 |

Discussion:

CSMCARB properly transitions from plastic to elastic behavior with decrease in temperature. Proper plastic strain is maintained with change in temperature. The combination of external and thermal loading is correct. The calculated results using CSMCARB agree with the closed-form solutions for axial stress and strain to 4 significant digits. A stress-strain diagram and the applied loads for verification problem #7 is illustrated in Figure D.9.

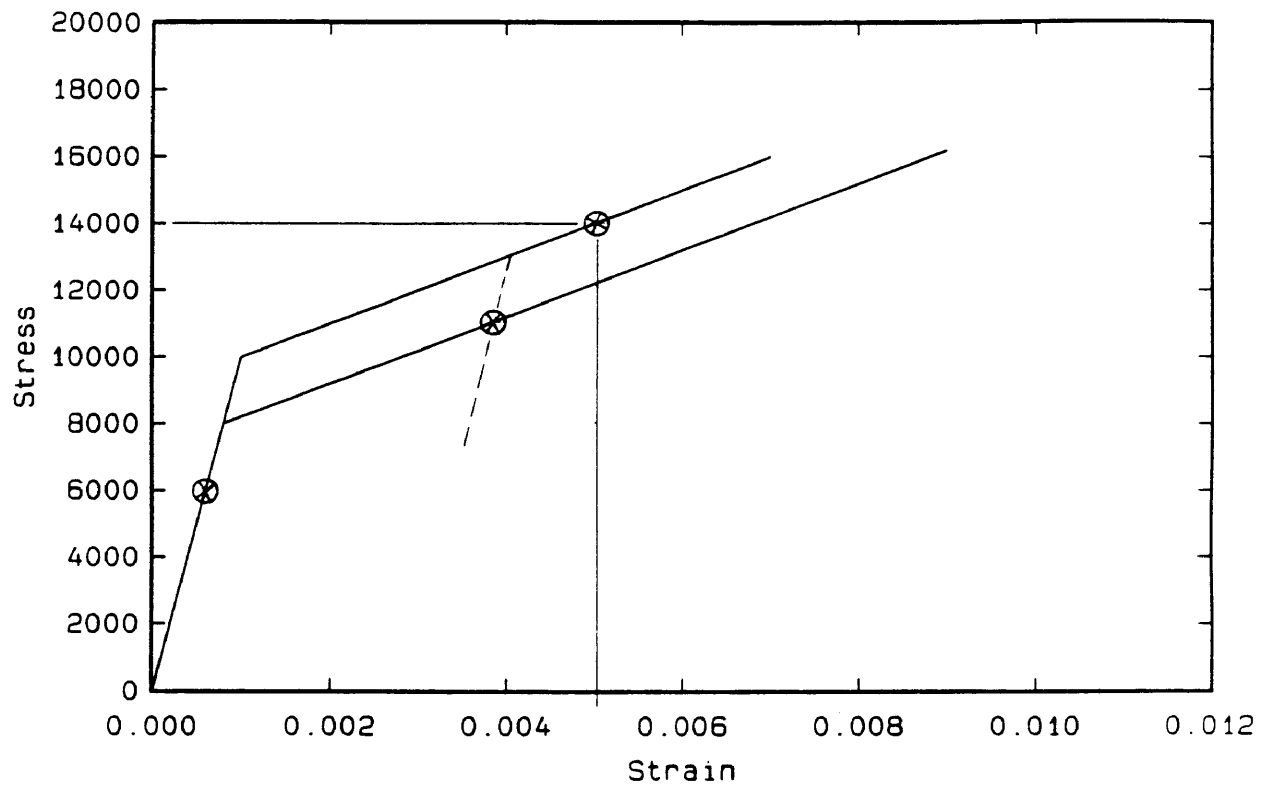


Figure D.9 Stress-strain diagram and the applied loads for verification problem #7.

VERIFICATION PROBLEM #8

Description:

One-dimensional plane stress elastic-plastic analysis with axial load. The temperature is increased (decrease S_y) and the model is allowed to plastically "creep". The expansion due to the temperature increase is included.

$$\begin{aligned}
 E &= 10 \times 10^6 \\
 E_T &= 1 \times 10^6 \\
 S_y &= (10 \times 10^3)(1 - 0.2T) \\
 \nu &= 0.30 \\
 \alpha &= 2 \times 10^{-3}
 \end{aligned}$$

Results:

| P | T | τ_{xx} | $\epsilon_{xx} \times 10^3$ |
|-------|---|-------------|-----------------------------|
| 8000 | 0 | 8000 | 0.8 |
| 11000 | 0 | 11000 | 2.0 |
| 11000 | 1 | 11000 | 5.8 |
| 14000 | 1 | 14000 | 8.8 |

Discussion:

Changing S_y by 20% in one step produces numerical instability. Intermediate load steps are needed for numerical stability during "creep" (i.e. $T=0.1$, $T=0.2$, etc.). Free thermal expansion due to temperature increase produces additional strain but does not alter the stress state. The calculated results using CSMCARB agree with the closed-form solutions for axial stress and strain to 4 significant digits. A stress-strain diagram and the applied loads for verification problem #8 is illustrated in Figure D.10.

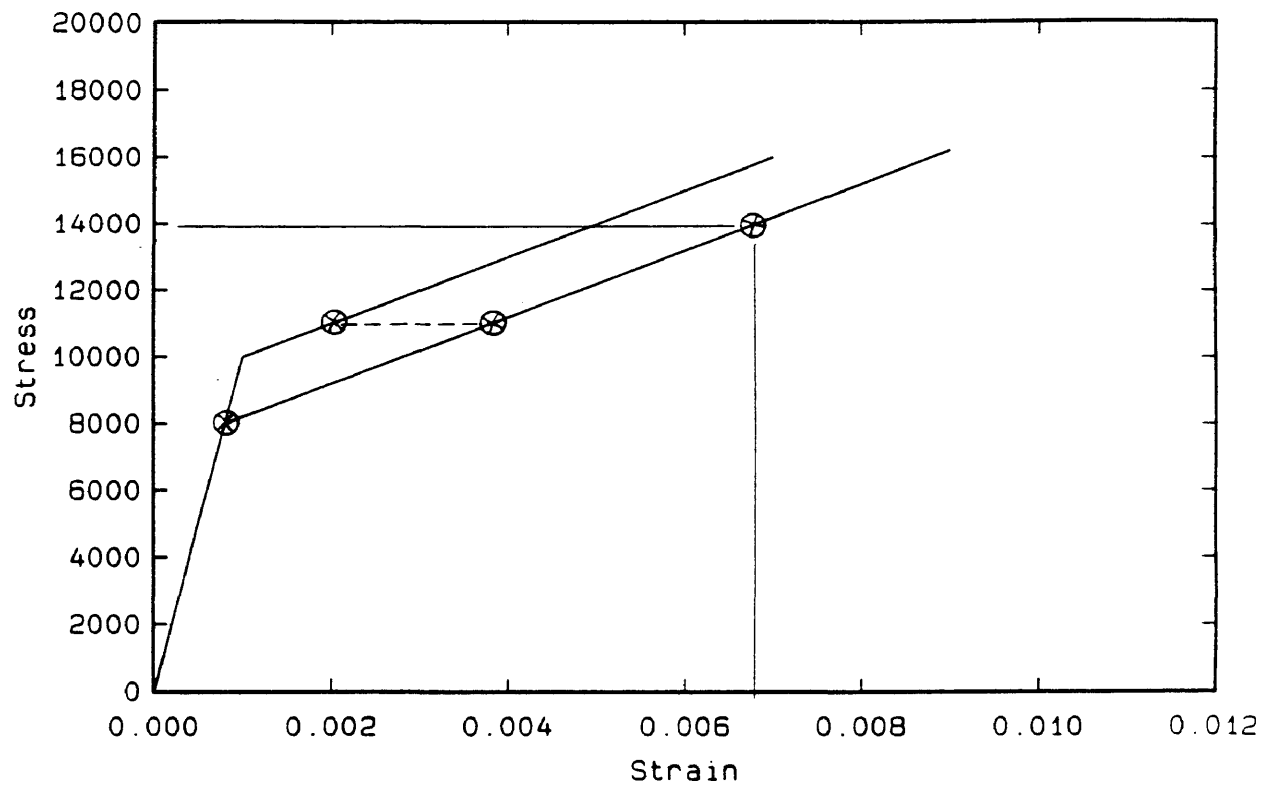


Figure D.10 Stress-strain diagram and the applied loads for verification problem #8.

VERIFICATION PROBLEM #9

Description:

One-dimensional plane stress elastic-plastic analysis with cantilever loading. The temperature is held constant at zero. The load is increased until the cantilever beam model begins to yield.

$$E = 10 \times 10^6$$

$$E_T = 1 \times 10^6$$

$$S_y = 10 \times 10^3$$

$$\nu = 0.30$$

Results:

| P | End Displacement (closed-form) | End Displacement (CSMCARB) |
|------|-----------------------------------|-------------------------------|
| -50 | -0.02 | -0.0201 |
| -100 | -0.04 | -0.0403 |
| -150 | -0.06 | -0.0605 |
| -200 | -0.08 | -0.0807 |
| -250 | -0.10 | -0.1181 (yielded) |

Discussion:

The end displacement results using CSMCARB agree with the closed-form solution for cantilever displacement to within 1% (within the elastic range).

VERIFICATION PROBLEM #10

Description:

Two-dimensional plane strain elastic-plastic analysis using the thick wall pressure vessel model in Figure D.2 (24). The internal pressure is incrementally increased to a maximum of 1.8 MPa.

$E = 2.1 \text{ GPa}$
 $E_T = 0 \text{ (perfectly plastic)}$
 $S_Y = 2.4 \text{ MPa}$
 $\nu = 0.30$

Displacement Results:

| Pressure, p (MPa) | Radial Displacement of Inner Face (24) (mm) | Radial Displacement of Inner Face (CSMCARB) (mm) |
|----------------------|---|--|
| 0.8 | 0.07 | 0.073 |
| 1.0 | 0.09 | 0.091 |
| 1.2 | 0.11 | 0.112 |
| 1.4 | 0.14 | 0.140 |
| 1.6 | 0.18 | 0.183 |
| 1.8 | 0.26 | 0.263 |

Discussion:

The displacement results given in the above table agree with the closed-form and calculated displacement results given in (24).

VERIFICATION PROBLEM #10, continued

Stress Results:

The stress results in the following table are for elements 2,5,8 and 11 through the cylinder thickness at a pressure of 1.4 MPa.

| Element Number | Gauss Point | σ_{θ} (24) (MPa) | σ_{θ} (CSMCARB) (MPa) |
|----------------|-------------|---------------------------------|--------------------------------------|
| 2 | 5 | 1.4994 | 1.49 |
| 2 | 6 | 1.7838 | 1.77 |
| 5 | 17 | 1.8011 | 1.81 |
| 5 | 18 | 1.5890 | 1.60 |
| 8 | 29 | 1.4381 | 1.44 |
| 8 | 30 | 1.2478 | 1.26 |
| 11 | 41 | 1.1464 | 1.15 |
| 11 | 42 | 1.0360 | 1.04 |

Discussion:

The hoop stress distribution calculated using CSMCARB agrees with the distribution presented in (24).

APPENDIX E Calculation of the Almen Strip Radius of Curvature

The radius of curvature for the modified Almen strip is calculated using Figure E.1 and trigonometry. The two variables of cord length, C , and arc deflection, A , fix the geometry of the specimen. Distance L is found using the relationship:

$$L = \sqrt{A^2 + \left(\frac{C}{2}\right)^2} \quad (\text{E.1})$$

The angle, α , is found using the relationship:

$$\alpha = \arctan \frac{A}{\left(\frac{C}{2}\right)} \quad (\text{E.2})$$

The angle, β , is then found using the relationship:

$$\beta = 90^\circ - \alpha \quad (\text{E.3})$$

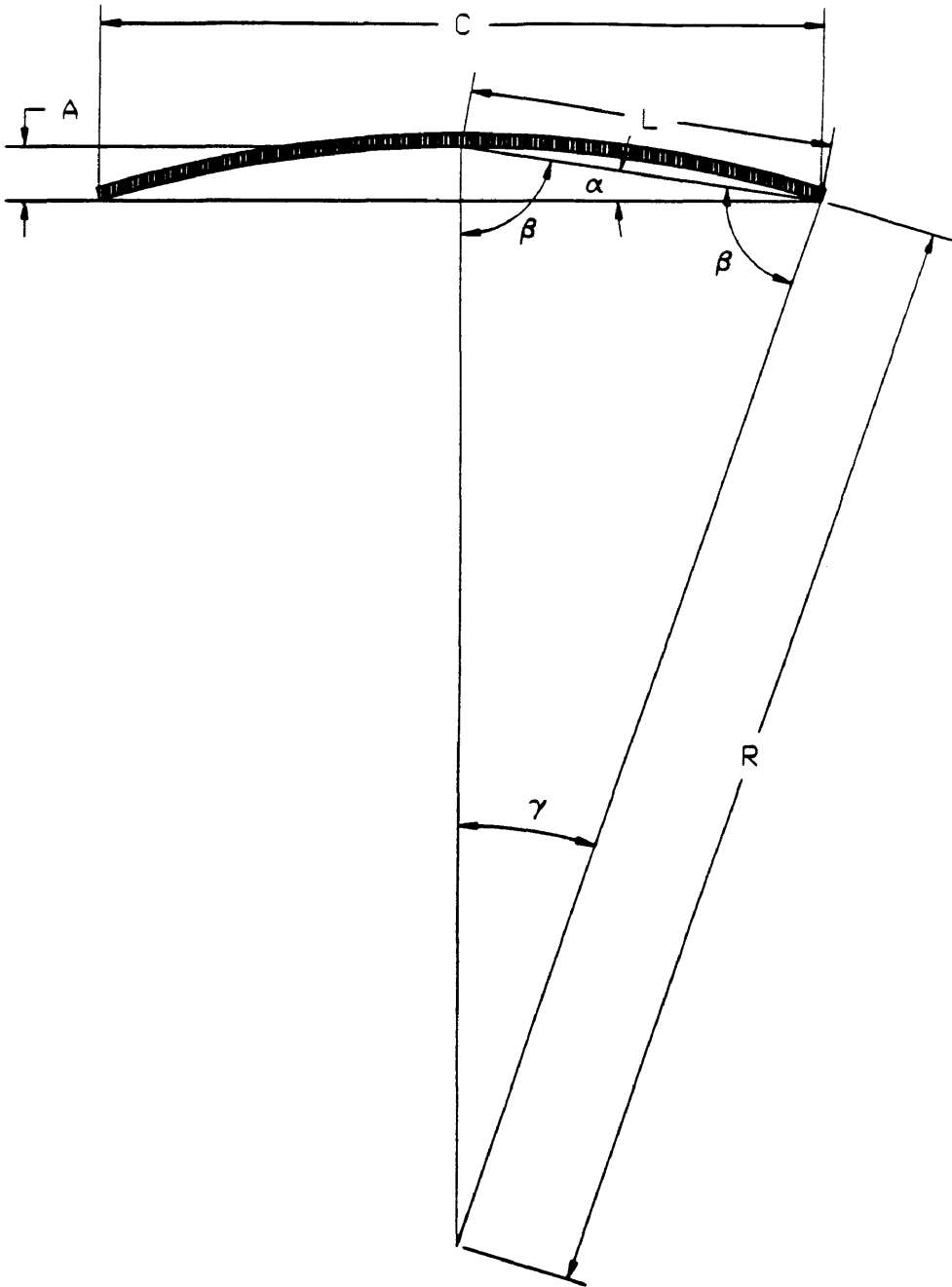


Figure E.1 Schematic representing the radius of curvature for the Almen strip.

The angle, γ , is found using the relationship:

$$\gamma = 180^\circ - 2\beta \quad (\text{E.4})$$

By the law of sines, the radius of curvature can then be found using the relationship:

$$R = \frac{(\sin\beta)}{(\sin\gamma)} L \quad (\text{E.5})$$